

**SIMULATION OF PERSONAL PROTECTIVE
EQUIPMENT EXPOSURE TO RADIOACTIVE
PARTICULATES**

**SIMULATION DE L'EXPOSITION D'ÉQUIPEMENT DE
PROTECTION PERSONNELLE À DES MACRO-
PARTICULES RADIOACTIVES**

A Thesis Submitted to the Division of Graduate Studies
of the Royal Military College of Canada
by

Michael J. Roeterink, BEng, rmc

In Partial Fulfillment of the Requirements for the Degree of
Master of Applied Science

October 2014

© This thesis may be used within the Department of National Defence but
copyright for open publication remains the property of the author.

Acknowledgements

This thesis was made possible as a result of the assistance of many people. Firstly, I would like to thank my parents for their constant support and confidence. Secondly, I would like to extend my sincerest gratitude to my supervisors, Dr. E.C. Corcoran and Dr. E.G. Dickson. Without their encouragement, leadership, and guidance this project would not have been possible. I would also like to acknowledge the financial support of the Natural Science and Engineering Research Council of Canada. Finally, I would be amiss if I did not thank the staff of the Department of Chemistry and Chemical Engineering, RMCC for their continued interest and assistance. I would like to specifically mention both the RMCC CBRN Protection Group and RMCC Analytical Sciences Group for their direction and expertise with regards to the planning and execution of numerous experiments, as well as Dr. D.G. Kelly, Dr. P. Bodurtha, and M.T. Andrews for their invaluable contributions to the technical aspects of this thesis.

Abstract

Airborne radioactive particulates constitute a significant hazard facing military members, emergency personnel, and the immediate public in any nuclear-related incident. Personal protective equipment (PPE) can be used to reduce wearer exposure to emitted radiation; however, existing PPE suits do not effectively attenuate all types of radiation and, thus, cannot offer complete protection in response to radiological hazard scenarios. In light of the Fukushima-Daiichi incident, it is evident that rigorous investigation and research needs to be undertaken in order to resolve this issue and to garner a better understanding of the level of protection provided by current PPE concepts.

The objective of this thesis is to develop a realistic dosimetric model of the human forearm, protected by a PPE sleeve, which can be used to determine the dose imparted to the tissue in the event of radiological particulate exposure. A two-fold approach is employed whereby: (1) a particle transport model is used to determine the concentration of radioactive particulates in five regions surrounding the forearm (both within and outside the PPE sleeve); and (2) these concentration data are then incorporated into a dosimetric model that uses the Monte Carlo N-Particle (MCNP) transport code to determine the dose imparted to the tissue. Nine modelling cases, representative of a combination of the three most likely radionuclide species (Co-60, Sr-90, and Cs-137) facing emergency personnel during a radiological dispersion event and three different PPE sleeve concepts (air impermeable fabric with closure leak, perfectly sealed air permeable fabric, and no shielding), were selected for analysis.

The preliminary model developed in this thesis was successfully able to determine the dose imparted to a human forearm as a result of exposure to radioactive particulates released in a dispersion event. The results indicate that the ability of the fabric to limit the transport of radioactive particulates has a greater impact on reducing the imparted dose than its ability to attenuate the incident radiation. A number of improvements to the model are proposed and discussed, such that it may be extended to consider more accurately particulate infiltration processes and whole-body dose and be used as a tool for Canadian Armed Forces (CAF) commanders during radiological emergencies.

Résumé

Les macro-particules radioactives aéroportées représentent un danger important pour les militaires, le personnel des urgences et le public immédiat lors d'incidents de nature nucléaire. L'équipement de protection personnelle (ÉPP) peut être utilisé afin de réduire l'exposition du porteur aux rayonnements émis; cependant, les vêtements d'ÉPP existants ne peuvent pas atténuer de manière efficace tous les types de rayonnement et, par conséquent, ils ne peuvent pas offrir une protection complète dans tous les scénarios de danger nucléaire. À la lumière de l'incident de Fukushima-Daiichi, il est évident qu'une enquête et une recherche rigoureuses doivent être entreprises pour résoudre cette question et pour acquérir une meilleure compréhension du niveau de protection fourni par les concepts actuels en matière d'ÉPP.

L'objectif de cette thèse est de développer un modèle réaliste de la dosimétrie de l'avant-bras humain protégé par une manche d'ÉPP et qui peut être utilisé pour déterminer la dose appliquée au tissu lors d'une exposition aux macro-particules radioactives. Une double approche est employée ici: (1) on utilise un modèle de transport de particules pour déterminer la concentration des macro-particules radioactives dans cinq régions de l'avant-bras (au-dedans et au-dehors de la manche de l'ÉPP) et, (2) on incorpore les données de concentration dans un modèle de dosimétrie qui utilise de code de transport par Monte Carlo "*Monte Carlo N-Particle (MCNP)*" pour déterminer la dose reçue par le tissu. On a choisi pour l'analyse neuf cas de modélisation représentatifs d'une combinaison des trois radioisotopes les plus probables (Co-60, Sr-90, et Cs-137) auxquels ont à faire face les membres du personnel d'urgence au cours d'un événement de dispersion radiologique, ainsi que trois concepts différents de manche d'ÉPP (tissu imperméable à l'air avec une fuite dans une fermeture, tissu perméable à l'air parfaitement scellé, et aucun blindage).

Le modèle préliminaire développé dans cette thèse était capable de déterminer avec succès la dose reçue par l'avant-bras humain lors d'un événement de dispersion de macro-particules radioactives. Les résultats indiquent que la capacité du tissu de limiter le transport des macro-particules radioactives a un impact sur la réduction de la dose appliquée bien supérieur à sa capacité d'atténuer le rayonnement incident. Un certain nombre d'améliorations sont proposées et discutées pour le modèle, comme celle d'une extension possible incluant un traitement plus précis des processus d'infiltration des macro-particules et de la dose sur tout le corps, ainsi que l'utilisation de ce modèle comme outil pour les commandants des Forces armées canadiennes lors d'urgences radiologiques.

Table of Contents

Acknowledgements.....	i
Abstract.....	ii
Résumé.....	iii
List of Tables	vii
List of Figures.....	x
List of Symbols, Abbreviations, and Acronyms	xiv
1. INTRODUCTION	1
1.1. Impetus.....	1
1.2. Objectives of Research	1
2. LITERATURE REVIEW	3
2.1. The Nature of Radiation.....	3
2.1.1. Types of radiation	3
2.1.2. Interaction of radiation with matter	6
2.1.3. Biological effects of radiation exposure	8
2.1.4. Quantifying dose.....	9
2.1.5. Acceptable exposure limits	11
2.2. Personal Protective Equipment	12
2.2.1. Types of PPE suits	12
2.2.1.1. Air permeable PPE suit.....	12
2.2.1.2. Air impermeable PPE suit.....	13
2.3. Aerosols	14
2.3.1. Properties of aerosols.....	14
2.3.2. Aerosol mechanics.....	15
2.3.3. Uniform particulate motion	16
2.3.4. Deposition of airborne particulates.....	17
2.3.5. Collection of airborne particulates by PPE fabrics	18
2.4. Particulate Transport Theory	21
2.4.1. Fick’s first law of diffusion	22
2.4.2. Fick’s second law of diffusion.....	22
2.4.3. Factors affecting diffusion	24
2.5. Radiation Hazard Scenarios	25

2.5.1.	Evaluating radiological events.....	26
2.5.2.	Major radiological events since World War II.....	26
2.5.3.	Classification of radiological hazard scenarios.....	28
3.	PROJECT METHODOLOGY.....	31
3.1.	Particulate Transport Model	32
3.2.	Dosimetric Model	34
4.	SCOPE OF PROJECT	36
4.1.	Forearm-based Model.....	36
4.2.	Exposure Conditions.....	37
4.3.	Modelling Cases	39
5.	EXPERIMENTATION.....	40
5.1.	Particulate Transport Benchmarking Experimentation.....	40
5.1.1.	COMSOL Multiphysics software	41
5.1.2.	Experimental objective	42
5.1.3.	Experimental methodology.....	42
5.1.4.	COMSOL modelling.....	45
5.1.5.	Experimental results and discussion	47
5.1.6.	COMSOL model benchmarking	50
5.1.7.	Summary of particulate transport experimentation and COMSOL modelling	54
5.2.	Transmittance Benchmarking Experimentation.....	55
5.2.1.	Monte Carlo N-Particle Transport Code, Version 5	56
5.2.2.	Experimental objectives.....	57
5.2.3.	Experimental methodology.....	57
5.2.3.1.	Fabric characterization.....	57
5.2.3.2.	Transmittance of gamma photons.....	58
5.2.4.	MCNP5 modelling.....	58
5.2.5.	Experimental results and discussion	59
5.2.5.1.	Fabric characterization.....	59
5.2.5.2.	Transmittance of gamma photons.....	60
5.2.5.3.	MCNP5 model benchmarking	61
5.2.6.	Summary of transmittance experimentation and MCNP5 modelling	64

6.	MODELLING.....	65
6.1.	Universal Modelling Dimensions	65
6.2.	Particulate Transport Model	67
6.2.1.	First principles model	68
6.2.2.	Penetration model	72
6.2.3.	No shielding cases	75
6.3.	Dosimetric model.....	75
7.	RESULTS AND DISCUSSION	82
7.1.	Particulate Transport Model	82
7.1.1.	First principles model	82
7.1.2.	Penetration model	87
7.1.3.	No shielding cases	90
7.2.	Dosimetric Model	93
7.2.1.	Co-60 and Cs-137 modelling cases.....	94
7.2.2.	Sr-90 modelling cases.....	99
7.3.	Analysis of the Nine Modelling Cases.....	100
7.3.1.	Regional dose rate.....	101
7.3.2.	Nine modelling cases	105
8.	RECOMMENDATIONS FOR FUTURE WORK	112
9.	CONCLUSION.....	114
10.	REFERENCES	116
11.	APPENDIX A.....	121
12.	APPENDIX B	127
13.	APPENDIX C	129
14.	APPENDIX D.....	131
15.	APPENDIX E	135
16.	APPENDIX F	136
17.	APPENDIX G.....	137
18.	APPENDIX H.....	138
19.	APPENDIX I	139
20.	APPENDIX J	140
21.	APPENDIX K.....	143
22.	APPENDIX L	147

List of Tables

<i>Table 1: Summary of radiation weighting factors (w_R) current as of the ICRP's 2005 Recommendations</i>	<i>10</i>
<i>Table 2: Summary of tissue weighting factors (w_T) current as of the ICRP's 2005 Recommendations</i>	<i>10</i>
<i>Table 3: Radiation exposure state categories and corresponding dose limits</i>	<i>11</i>
<i>Table 4: Best general estimate of deposition velocities on various surfaces as a function of particulate diameter</i>	<i>18</i>
<i>Table 5: Summary of the nine modelling cases selected for analysis</i>	<i>39</i>
<i>Table 6: Particulate size designations and corresponding size range</i>	<i>44</i>
<i>Table 7: Summary of initial conditions for the particulate transport experimentation</i>	<i>44</i>
<i>Table 8: Rate of decrease of the outer concentration for each of the three particulate sizes</i>	<i>50</i>
<i>Table 9: ICP-MS and INAA(*) results for the first and second generation CRC fabrics</i>	<i>60</i>
<i>Table 10: Forearm dimensions corresponding to an average male member of the CAF</i>	<i>66</i>
<i>Table 11: Summary of dimensions used in both the particulate transport and dosimetric models</i>	<i>67</i>
<i>Table 12: Summary of k_s, k_{is}, and k_c values used in the first principles model</i>	<i>70</i>
<i>Table 13: Comparison of the CBRN fabric and Paul Boyé fabric.....</i>	<i>74</i>
<i>Table 14: Density and elemental composition of each material used in the dosimetric model.....</i>	<i>77</i>
<i>Table 15: Decay schemes for Co-60, Sr-90, and Cs-137 as used in the dosimetric model.....</i>	<i>80</i>

<i>Table 16: Outer concentration values used in the first principles model for each radionuclide</i>	<i>83</i>
<i>Table 17: Regional concentration values generated by the first principles model for the case in which the air impermeable fabric was exposed to Co-60 particulates</i>	<i>84</i>
<i>Table 18: Magnitudes of each of the five regions for the PPE sleeve composed of the air impermeable fabric</i>	<i>84</i>
<i>Table 19: Regional activity values for the modelling case in which the air impermeable fabric was exposed to Co-60 particulates</i>	<i>85</i>
<i>Table 20: Regional activity values for the modelling case in which the air impermeable fabric was exposed to Sr-90 particulates</i>	<i>85</i>
<i>Table 21: Regional activity values for the modelling case in which the air impermeable fabric was exposed to Cs-137 particulates</i>	<i>86</i>
<i>Table 22: Regional concentration values generated by the penetration model for the case in which the air permeable fabric was exposed to Co-60 particulates</i>	<i>88</i>
<i>Table 23: Magnitudes of each of the five regions for the PPE sleeve composed of the air permeable fabric</i>	<i>88</i>
<i>Table 24: Regional activity values for the modelling case in which the air permeable fabric was exposed to Co-60 particulates</i>	<i>89</i>
<i>Table 25: Regional activity values for the modelling case in which the air permeable fabric was exposed to Sr-90 particulates</i>	<i>89</i>
<i>Table 26: Regional activity values for the modelling case in which the air permeable fabric was exposed to Cs-137 particulates</i>	<i>89</i>
<i>Table 27: Regional concentration values generated using fundamental particulate transport theory for the case in which no PPE sleeve was used to protect the forearm from exposure to Co-60 particulates.....</i>	<i>91</i>
<i>Table 28: Magnitudes of each of the outer volume and forearm surface area given the absence of a PPE sleeve</i>	<i>91</i>

Table 29: Regional activity values for the modelling case in which PPE sleeve was used to protect the forearm from exposure to Co-60 particulates92

Table 30: Regional activity values for the modelling case in which no PPE sleeve was used to protect the forearm from exposure to Sr-90 particulates92

Table 31: Regional activity values for the modelling case in which no PPE sleeve was used to protect the forearm from exposure to Cs-137 particulates92

Table 32: Total dose imparted to the forearm tissue as a function of time for the modelling cases involving exposure to Co-60 particulates 107

Table 33: Total dose imparted to the forearm tissue as a function of time for the modelling cases involving exposure to Sr-90 particulates..... 107

Table 34: Total dose imparted to the forearm tissue as a function of time for the modelling cases involving exposure to Cs-137 particulates..... 107

List of Figures

<i>Figure 1: Radioactive decay and the locus of stability</i>	4
<i>Figure 2: CAF member modelling the Horizon 1 CWC</i>	13
<i>Figure 3: Traditional CRC suit</i>	14
<i>Figure 4: Collection of particulates via the impaction mechanism</i>	19
<i>Figure 5: Collection of particulates via the interception mechanism</i>	20
<i>Figure 6: Collection of particulates via the diffusion mechanism</i>	20
<i>Figure 7: Differential element used in the derivation of Fick’s second law of diffusion</i>	22
<i>Figure 8: Levels making up the INES</i>	26
<i>Figure 9: Mock radiation hazard scenario involving the deliberate dispersal of radiological material</i>	29
<i>Figure 10: Geographical health implications of radioactive particulates released during a nuclear reactor event</i>	30
<i>Figure 11: Schematic of project methodology</i>	31
<i>Figure 12: Location of radioactive particulates at t_0</i>	32
<i>Figure 13: Location of radioactive particulates at t_∞</i>	33
<i>Figure 14: Dosimetric model illustrating the location of the five regional concentration source terms</i>	35
<i>Figure 15: Mechanical ‘sleeved forearm’ apparatus used in the particulate transport benchmarking experimentation</i>	43
<i>Figure 16: Experimentally-obtained inner and outer concentration results for the Size A particulates</i>	47
<i>Figure 17: Experimentally-obtained average inner and outer concentration results for the Size A particulates</i>	48

<i>Figure 18: Experimentally-obtained average inner and outer concentration results for the Size B particulates</i>	<i>49</i>
<i>Figure 19: Experimentally-obtained average inner and outer concentration results for the Size C particulates.....</i>	<i>49</i>
<i>Figure 20: Comparison of the average experimental and COMSOL model inner concentration results for each particulate size</i>	<i>51</i>
<i>Figure 21: COMSOL model results of the velocity profile of the air flowing through the experimental apparatus</i>	<i>53</i>
<i>Figure 22: Comparison of the average experimental and adjusted COMSOL model inner concentration results for the Size B particulates.....</i>	<i>54</i>
<i>Figure 23: Photograph and SEM images (100× magnification, using 20.0 keV electrons at 1 mbar) of the second generation CRC fabric</i>	<i>59</i>
<i>Figure 24: Experimentally-obtained transmittance results for a single layer of the first and second generation CRC fabrics as a function of gamma photon energy</i>	<i>61</i>
<i>Figure 25: Comparison of experimental and MCNP5 transmittance results for a single layer of the second generation CRC fabric as a function of gamma photon energy</i>	<i>62</i>
<i>Figure 26: Refined MCNP5 model illustrating the distribution of gamma photons incident on the detector during the transmittance experimentation</i>	<i>63</i>
<i>Figure 27: Comparison of experimental and adjusted MCNP5 transmittance results for a single layer of the second generation CRC fabric as a function of gamma photon energy.....</i>	<i>64</i>
<i>Figure 28: Schematic describing particulate transport for an air impermeable fabric.....</i>	<i>69</i>
<i>Figure 29: Schematic of the dosimetric model geometry</i>	<i>77</i>
<i>Figure 30: End view of the dosimetric model geometry illustrating each of the five source locations: a) surface of the forearm, b) inner air gap, c) inner surface of the PPE sleeve, d) outer surface of the PPE sleeve, and e) outer environment</i>	<i>79</i>

<i>Figure 31: Overall dose (gamma and beta) imparted to forearm as a function of source location for each of the PPE sleeve compositions when exposed to Co-60 particulates</i>	<i>95</i>
<i>Figure 32: Gamma-contributed dose imparted to forearm as a function of source location for each of the PPE sleeve compositions when exposed to Co-60 particulates</i>	<i>97</i>
<i>Figure 33: Beta-contributed dose imparted to forearm as a function of source location for each of the PPE sleeve compositions when exposed to Co-60 particulates</i>	<i>98</i>
<i>Figure 34: Overall dose imparted to forearm as a function of source location for each of the PPE sleeve compositions when exposed to Sr-90 particulates</i>	<i>100</i>
<i>Figure 35: Regional dose rates for the modelling case in which the forearm was surrounded by a PPE sleeve composed of the second generation CRC fabric and exposed to Co-60 particulates</i>	<i>102</i>
<i>Figure 36: Regional dose rates for the modelling case in which the forearm was surrounded by a PPE sleeve composed of the CBRN fabric and exposed to Co-60 particulates</i>	<i>103</i>
<i>Figure 37: Regional dose rates for the modelling case in which the forearm was not surrounded by a PPE sleeve and was exposed to Co-60 particulates</i>	<i>104</i>
<i>Figure 38: Total dose rate plot and regression equation for the modelling case in which the forearm was surrounded by a PPE sleeve composed of the second generation CRC fabric and exposed to Co-60 particulates</i>	<i>106</i>
<i>Figure 39: Comparison of the total dose imparted to the forearm tissue as a function of time for the modelling cases involving exposure to Co-60 particulates and the ICRP maximum acceptable whole-body annual dose</i>	<i>109</i>
<i>Figure 40: Comparison of the total dose imparted to the forearm tissue as a function of time for the modelling cases involving exposure to Sr-90 particulates and the ICRP maximum acceptable whole-body annual dose</i>	<i>110</i>

Figure 41: Comparison of the total dose imparted to the forearm tissue as a function of time for the modelling cases involving exposure to Cs-137 particulates and the ICRP maximum acceptable whole-body annual dose 111

List of Symbols, Abbreviations, and Acronyms

A	Activity
APS	Aerodynamic particle sizer
ASG	Analytical Sciences Group
BDF	Backward differentiation formula
C_c	Cunningham slip correction factor
C_{down}	Downstream concentration
C_i	Inner volume concentration
$C_{innersuit}$	Inner suit surface concentration
C_o	Outer volume concentration
$C_{outersuit}$	Outer suit surface concentration
C_{skin}	Skin surface concentration
C_{up}	Upstream concentration
CAD	Computer aided design
CAF	Canadian Armed Forces
CBRN	Chemical, biological, radiological, and nuclear
CFD	Computational fluid dynamics
CRC	Combat radio-opaque commercial
CSA	Canadian Standards Association
CWC	Chemical warfare coverall
d	Aerodynamic diameter
d_f	Fibre diameter
d_p	Particulate diameter
D	Absorbed dose
D_f	Diffusion coefficient of fabric
DRDC	Defence Research and Development Canada
E	Effective dose
EDX	Energy-dispersive X-ray spectroscopy
F_{drag}	Aerodynamic drag force
FTIR	Fourier transform infrared
g	Acceleration due to gravity
HPGe	High purity germanium
I	Intensity
IAEA	International Atomic Energy Agency
ICP-MS	Inductively coupled plasma-mass spectrometry
ICRP	International Commission on Radiological Protection
INAA	Instrumental neutron activation analysis
INES	International nuclear and radiological event scale
J_A	Diffusive flux of species A
k	Boltzmann constant
LET	Linear energy transfer

LOCA	Loss of coolant accident
M	Mass number
MCNP	Monte Carlo N-Particle Transport Code
MPPS	Most penetrating particulate size
NATO	North Atlantic Treaty Organization
NEW	Nuclear energy worker
NFPA	National Fire Protection Association
NSERC	Natural Science and Engineering Research Council of Canada
P	Penetration efficiency
Δp	Pressure drop
PARDISO	Parallel sparse direct solver
PPE	Personal protective equipment
R_A	Rate of reaction of species A
Re	Reynolds number
RDD	Radiological dispersion device
RES	Radiation exposure state
RMCC	Royal Military College of Canada
RTG	Radioisotope thermoelectric generator
SEM	Scanning electron microscopy
t	Fabric thickness
T	Temperature
U_0	Free-stream velocity
v^*	Molar average velocity
v_{dep}	Deposition velocity
v_{TS}	Terminal settling velocity
V	Velocity
w_R	Radiation weighting factor
w_T	Tissue weighting factor
X	Parent radionuclide
Y	Daughter radionuclide
Z	Atomic number
Θ	Fibre packing density
η	Dynamic viscosity
ρ	Material density
ρ_g	Density of gas
λ	Mean free path
μ	Linear attenuation coefficient
$\frac{\mu}{\rho}$	Mass attenuation coefficient
ν	Neutrino
$\bar{\nu}$	Anti-neutrino

1. INTRODUCTION

1.1. Impetus

Throughout history, there have been numerous examples of nuclear-related accidents and incidents. While these events often differ in cause and severity, ranging from full-scale nuclear reactor meltdowns to the improper disposal of radioisotope sources, the majority of situations coincide with the release of airborne radioactive particulates and other such materials into the environment. This is significant as airborne radioactive particulates are one of the most serious hazards facing first responders and the immediate public during a nuclear-related incident and must be considered when determining human exposure levels. As such, every effort must be made to protect personnel from the harmful effects of these particulates and one of the most effective and widespread ways to do this is through the use of personal protective equipment (PPE). Currently, various types of commercially-available PPE suits are marketed with the ability to reduce wearer exposure to radiation hazards by either blocking radioactive particulates or attenuating the actual radiation itself; however, the extent to which these suits are effective at limiting wearer radiation exposure is not well understood. As it stands today, most commonly worn PPE suits do not effectively attenuate all types of radiation and, thus, cannot offer complete protection in the event of a radiological hazard scenario. In light of the recent Fukushima-Daiichi disaster, it is evident that rigorous investigation and research needs to be undertaken in order to resolve this issue and to garner a better understanding of the level of protection provided by existing PPE suits. Correspondingly, this project seeks to investigate how the presence or absence of a range of PPE suits impacts the dose imparted to the wearer in the event of radiological exposure.

1.2. Objectives of Research

The objective of this thesis is to create a realistic dosimetric model of the human forearm, protected by a PPE sleeve, which can be used as a tool to assess the dose imparted to the tissue in the event of radiological particulate exposure. A two-fold modelling approach is employed whereby: (1) a particulate transport model is used to determine the concentration of radioactive particulates in the regions surrounding the forearm (both within and outside the protective sleeve); and (2) these concentration data are then incorporated into a dosimetric model that uses the Monte Carlo N-Particle Transport Code, Version 5 (MCNP5) to determine the dose imparted to the tissue. A human forearm and sleeve are modelled in place of a whole-body phantom as this significantly simplifies the model geometry and is less computationally intensive. Also, the model is limited to examining exposure

levels for select radiological cases based on dispersion events of radioactive particulates that emit gamma photons and/or beta particles. Future models (outside the scope of this thesis) could consider whole body dose and may consider all types of radiation in-suit (*e.g.*, alpha, beta, gamma, proton, and neutron). This future research will be invaluable in the development of radiation exposure policies and allow for comparison with recommended exposure guidelines. Thus, the long-term goal of this research is to develop a model (based on entered incident parameters and PPE characteristics) that Canadian Armed Forces (CAF) commanders can reference in order to determine the dose their personnel would receive whilst responding to a radiological event.

2. LITERATURE REVIEW

As this thesis is based upon a two-fold modelling approach, it is necessary to include a review of both radiation protection principles and particulate transport theory. In this regard, the following chapter commences with a discussion on the nature of radiation and how various types of PPE suits can be used to mitigate its harmful effects. Aerosol behaviour and the fundamental theories describing the transport of airborne particulates are then presented. Finally, a review of radiological hazard scenarios is conducted to illustrate the serious health threat posed by airborne radioactive particulates during a radiological dispersion event.

2.1. The Nature of Radiation

2.1.1. Types of radiation

Radioactivity is a property that is inherent to an individual nuclear species and is not dependent on external factors such as temperature, pressure, or chemical state. In that regard, the probability that a nucleus decays is an intrinsic property of that particular nuclear species and is an entirely random process. All nuclides with an atomic number greater than eighty-three are radioactive and, as a result, undergo various modes of radioactive decay in order to reach a more stable state [1]. The reason for this is that as atomic number increases, the electrostatic repulsion between protons in the nucleus becomes more significant. In order to maintain stability, the number of neutrons in the nucleus must also increase; however, there is limit to the ratio of neutrons to protons that a nucleus can support and still remain stable [1]. Once this limit is exceeded, the parent radionuclide will undergo some mode of radioactive decay in order to produce a daughter radionuclide with a neutron to proton ratio that falls somewhere along the locus of stability. This phenomenon is presented in Figure 1. Activity, A , is the rate at which a particular radioactive species undergoes decay and, thus, is related to the number of radioactive particles emitted per unit time [1]. The SI unit for activity is the Becquerel (Bq), which is equivalent to one disintegration per second. There are several different modes of radioactive decay that coincide with the release of one or more of the four main types of radiation: alpha, beta, gamma, and neutron.

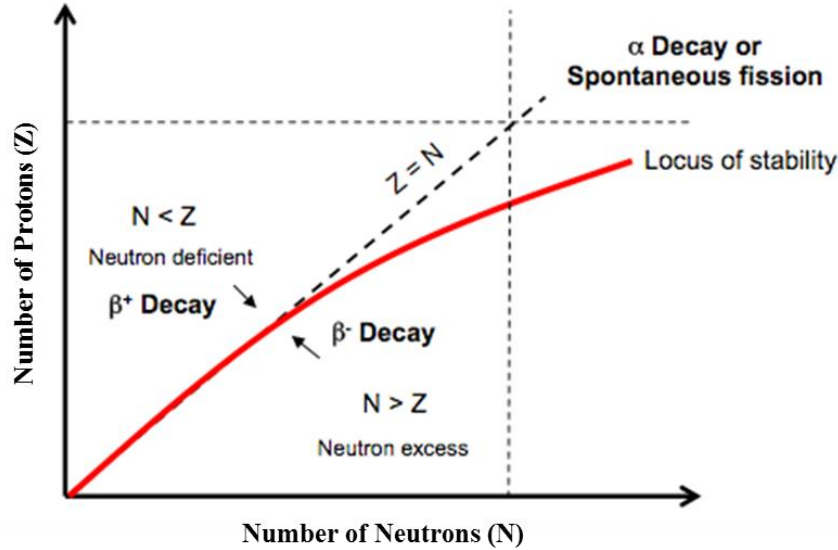


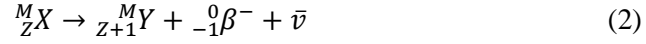
Figure 1: Radioactive decay and the locus of stability, reproduced with permission from [2]

As illustrated in Figure 1, alpha decay occurs for heavy nuclei that do not have enough neutrons to be stable and results in the release of an alpha particle in an attempt to increase the neutron to proton ratio [3]. An alpha particle is essentially a helium nucleus composed of two protons and two neutrons and carries an electrical charge of positive two [4]. Alpha particles have discrete energies that are characteristic of their parent radionuclide [3]. Equation 1 illustrates a parent radionuclide, X, undergoing alpha decay to produce a daughter radionuclide, Y, and an alpha particle, α . As a result of the production of the alpha particle, in order to ensure the conservation of mass, the mass number, M, of the daughter radionuclide must be four less than that of the parent radionuclide, while its atomic number, Z, decreases by two.



Beta decay occurs when an unstable radionuclide decays by emitting either an electron (beta minus decay) or a positron (beta plus decay). Figure 1 indicates that if there is an excess of neutrons in the nucleus, beta minus decay will occur. In this decay mode, a neutron is effectively transformed into a proton, whilst a beta minus particle and an anti-neutrino are simultaneously emitted [4]. This process is desirable as it decreases the neutron to proton ratio. Although the anti-neutrino has no electrical charge and a mass very close to zero, its presence necessitates the

sharing of the available kinetic energy between the beta particle and the anti-neutrino [4]. As a result, the emitted beta particle can have a range of energies depending on the respective kinetic energies of the anti-neutrino and daughter radionuclide. Equation 2 illustrates the beta minus decay process.



Conversely, with reference to Figure 1, if the radionuclide is deficient in neutrons, either a beta plus decay or electron capture process will occur. In beta plus decay, a proton is transformed into a neutron, while a positron (beta plus particle) and neutrino are emitted from the nuclide [4]. As a result, the neutron to proton ratio is increased. As with the anti-neutrino, the presence of the neutrino ensures that there is a continuous range of energies for the emitted beta plus particle. Equation 3 illustrates a generic representation of beta plus decay.



For situations where there is insufficient energy to allow for the emission of a positron but it is still desirable to increase the neutron to proton ratio, radioactive decay may occur by electron capture [3]. In this decay mode, a proton effectively combines with a low-orbital electron to produce a neutron and a neutrino [3]. Electron capture is often accompanied by the emission of characteristic X-rays, as outer-shell electrons fall to fill the void left by the captured electron, and Auger electrons [3]. Electron capture is commonly expressed as shown in Equation 4 [3].



In extreme cases, some radionuclides may also undergo proton emission in order to increase their neutron to proton ratio [5]. Proton emission is not a naturally-occurring decay mode, but may result via nuclear reactions and often follows beta decay in instances where the nucleus is in a highly excited state [5]. Equation 5 illustrates the generic proton emission decay mode [5].



Gamma photons are emitted when an unstable nucleus undergoes a transition from an excited, upper energy level to a lower, more stable energy state [1]. The energy of the emitted gamma photon is the difference between these two energy levels. Light nuclides often have well separated energy levels that produce hard or highly energetic gamma photons, whilst heavier nuclides are characterized as having more closely spaced energy levels that result in soft or low energy gamma photons [3]. Gamma photons are commonly produced in conjunction with other types of radiation as excited daughter nuclides return to their ground state. It is also

important to mention that the primary difference between gamma photons and X-rays is their point of origin. As mentioned earlier, gamma photons originate within the nucleus of an atom; on the other hand, X-rays originate from electronic orbitals and are produced when an electron transitions from an outer shell to an inner shell [3]. Equation 6 illustrates the emission of a gamma photon as a result of a nuclide transitioning from an excited level back to its ground state.



The final species that may be released as a result of radioactive decay is the neutron. Neutrons are emitted from heavy radionuclides ($Z > 90$, $M > 230$) as a result of spontaneous fission and have a continuous spectrum of energies [3]. In this decay process, the atomic number of the daughter nuclide is one less than that of the parent, whilst the atomic number remains unchanged. This decay mode is shown in Equation 7. Neutrons can also be produced as a result of certain nuclear reactions and by induced fission inside nuclear reactors.



2.1.2. Interaction of radiation with matter

Now that the different types of radiation and their means of production have been identified, it is necessary to illustrate how radiation interacts with matter. Radiation can interact with matter in a variety of different ways. In this regard, it is classified according to whether it is directly or indirectly ionizing [1]. Ionization is the process by which an orbital electron absorbs enough energy to overcome its binding energy and is subsequently liberated from the atom creating an ion pair. Directly ionizing radiation includes charged species, such as protons, alpha particles and beta particles, which possess sufficient kinetic energy to ionize orbital electrons [3]. As these charged particles move, they interact with nearby electrons and experience a continuous loss of energy; as a result, these particles have a well-defined range depending on the medium in which transport is taking place. Indirectly ionizing radiation consists of uncharged photons and particles, such as X-rays, gamma-rays, and neutrons, which have sufficient energy to liberate directly ionizing secondary charged particles [1]. In this sense, range is best characterized as the probability of an interaction taking place within a given medium as no amount of material completely removes all of the radiation [3]. This section outlines how each of the different types of radiation interacts with matter.

There are three main mechanisms by which alpha particles can interact with matter: electronic slowing-down, electron capture, and nuclear slowing-down [3]. Electronic slowing-down occurs at high velocities as the majority of the alpha particle's energy is dissipated as kinetic energy to orbital electrons that are then

stripped from their atoms or molecules [3]. Electron capture begins to occur when the alpha particle's velocity becomes comparable to that of the surrounding K-shell electrons [3]. As a result, the alpha particle will begin to absorb electrons from the surroundings. Finally, nuclear slowing-down occurs when the alpha particle's velocity is equivalent to that of the valence electrons of the atoms making up the medium [3]. At this stage, the alpha particle continues to lose energy due to elastic collisions with these atoms. Due to their relatively high mass and positive charge, alpha particles are highly ionizing, but only have a relatively short range (*e.g.*, a few centimetres in air) [4]. Alpha particles cannot penetrate an individual's skin, but can be extremely dangerous if they gain entry into the body via inhalation, ingestion, or through an open wound.

Beta particles interact with matter according to a variety of different processes. The first mechanism is the inelastic collision of the particle itself with atomic electrons and simply results in the excitation or ionization of these atomic electrons [3]. The second process is similar, but consists of an inelastic collision between the beta particle and the nucleus of an atom [3]. Such a collision often leaves the nucleus in an excited state whereby it will eventually return to its ground state with the accompanying emission of gamma photons. It is also possible for beta particles to transfer energy to the surrounding medium via annihilation, the Bremmstrahlung effect, or the Cerenkov effect [1]. Finally, beta particles may also undergo elastic collisions with the nuclei of the atoms making up the medium [3]. Such collisions will have a limited impact on the velocity of the beta particle, but will greatly alter its direction. Beta particles are less ionizing than alpha particles, but are much more penetrative. In most instances, a sheet of aluminium foil or wooden block offers sufficient protection from this type of radiation [3].

Gamma photons engage with matter via three main interactions: the photoelectric effect, Compton scattering, and pair production. For low energy gamma photons (< 1 MeV), the photoelectric effect is the dominant interaction mechanism [3]. In this process, an incident photon transfers all of its energy to an orbital electron that is then ejected from the atom [1]. For photons in the intermediate energy range (1-5 MeV), the dominant type of interaction is Compton scattering [3]. Compton scattering occurs when an incident photons transfers some, but not all, of its energy to an orbital electron. As a result, the electron is liberated from its energy shell and a secondary photon of decreased energy is produced [1]. Pair production is the final type of photon interaction and requires an incident photon with energy greater than 1.02 MeV [1]. The reason for this is that the incident photon creates an electron-positron pair, which will eventually undergo an annihilation event. An annihilation event results in the production of two 511 keV gamma photons travelling in opposite directions [3]. The likelihood that a certain type of interaction occurs is based on the energy of the incident photon, as shown above, and the medium material. In this regard, different materials have unique

cross-sections dictating the probability of a photoelectric effect, Compton scattering, or pair production interaction for various incident photon energies [3]. The sum of these cross-sections equates to the linear attenuation coefficient, μ , which can be normalized to a mass attenuation coefficient, $\left(\frac{\mu}{\rho}\right)$, by dividing by the material density, ρ [1]. Both the linear and mass attenuation coefficients are important in determining what thickness of material is required to reduce the intensity of the gamma radiation by a desired amount. In this regard, from a radiation safety standpoint, a high mass attenuation coefficient is advantageous as it corresponds to increased protection capabilities. Again, because gamma photons are a type of indirectly ionizing radiation, they do not have a defined range in any medium. That being said, it is possible to reduce the intensity of gamma photons using various thicknesses of materials such as lead or steel.

Like each of the other three main types of radiation, neutrons can interact with matter in a variety of different ways. In an elastic scattering collision, an incident neutron collides with a nucleus and transfers a portion of its energy to this body [3]. In an inelastic scattering collision, the target nucleus is raised to an excited state [3]. The excited nucleus will eventually return to its ground level via the emission of a photon or other radioactive species. The third type of neutron interaction is a capture event in which the neutron is absorbed by the contacting nucleus and a secondary species, such as a proton or alpha particle, is released [1]. The final interaction mechanism is called a spallation event [3]. A spallation event occurs when a collision nucleus is fragmented into several pieces by an incident neutron. In order for this mechanism to occur, the incident neutron must have upwards of 100 MeV of kinetic energy [3]. Because neutrons are a type of indirectly ionizing radiation, they do not have a defined range in any medium but are highly penetrating due to their neutral charge. However, it is possible to reduce their intensity using materials such as water or concrete.

2.1.3. Biological effects of radiation exposure

Having identified how each of the different types of radiation interacts with matter, it is now necessary to examine the effects of radiation on the human body. When any form of radiation is absorbed by biological material, there is a chance that it may disrupt cells and/or cellular DNA through either direct or indirect action [6]. Direct action occurs when energy deposited by radiation is able to directly affect a cell and/or its DNA by initiating a chain of events that results in biological change [6]. Direct action is the dominant process for radiation types with high linear energy transfer (LET) such as alpha particles, beta particles, protons, and heavy ions. Indirect action occurs when radiation, such as gamma photons or neutrons, interacts with other atoms in the cell to produce species that can then damage the cell and/or its DNA [7]. More specifically, gamma photons can react

with water to produce H_2O^+ ion radicals, which can further react with water to produce hydroxyl radicals [7]. These species are extremely reactive and are capable of disrupting the base pair backbone making up the DNA. Neutrons also damage DNA via indirect action; however, they do so by interacting with the nuclei of atoms and setting in motion charged particles such as recoil protons, alpha particles, or heavy ions [6].

Whether by direct or indirect action, the absorption of radiation can trigger complex biological chain reactions, which result in morphological and functional modifications to living cells [6]. Depending on the severity and extent of the irradiation, cellular dysfunction, sclerosis, metaplasia, mutation, or death may occur. Cellular dysfunction results in a cell's inability to function correctly and may inhibit important processes such as metabolism and reproduction [3]. Sclerosis is the premature aging of a cell, while metaplasia occurs when a differentiated cell is transformed into another type of differentiated cell [3]. Cellular mutation results when there is a transformation of the hereditary DNA stored in the nucleus and can have both somatic and genetic effects [3]. Finally, in extreme cases where the cell receives an acute dose of radiation and is not able to repair itself, cell death may occur [3].

2.1.4. Quantifying dose

While complex, the manner in which radiation reacts within the body is essentially a matter of energy transfer influenced by five important factors: the quantity of energy absorbed by the tissue, the volume of the tissue absorbing the energy, the nature of the radiation, the nature of the tissue being irradiated, and the duration of the irradiation [3]. Dosimetric quantities and, by extension, radiation and tissue weighting factors are necessary as they allow human radiation exposure to be evaluated in a quantitative manner. In this regard, it is possible to relate the effects of radiation to the dose absorbed by an individual or particular area of the body [8]. As provided in Equation 8, the International Commission on Radiological Protection (ICRP) defines absorbed dose, D , as the quotient of the mean energy transferred by ionizing radiation or particle to a volume of matter ($d\bar{\epsilon}$) per unit mass of the irradiated material (dm) in that volume [8].

$$D = \frac{d\bar{\epsilon}}{dm} \quad [\text{units: Gy}] \quad (8)$$

When using this definition, it is important to remember that the value of the mean energy is a stochastic quantity. This means that while the amount of energy imparted in many cells will be zero, in certain cells hit directly by the radiation, the amount will be several orders of magnitude greater than that of the mean [8]. The

unit of absorbed dose is the gray (Gy) which, in SI units, is equivalent to a joule per kilogram (J kg^{-1}).

The ICRP has also developed “*specific dosimetric quantities for radiological protection that allow the extent of exposure to ionizing radiation from both whole and partial body external irradiation*” [8] to be determined. Unfortunately, this is very difficult to quantify as both the radiation type and type of tissue being irradiated can drastically influence the dose that is received. The concept of effective dose, E , attempts to reconcile these two factors through the inclusion of separate radiation, w_R , and tissue, w_T , weighting factors. These weighting factor values are established from experimental data and epidemiological studies and, hence, are intended to take into consideration the stochastic effects resulting from various tissue or organ exposures to different types of radiation [8]. Additionally, the empirical nature of both weighting factor values means that they are subject to change as new radiological and biological data are gathered and interpreted over time. A summary of the latest radiation and tissue weighting factor values, as per the 2005 Recommendations of the ICRP, are provided in Table 1 and Table 2, respectively.

Table 1: Summary of radiation weighting factors (w_R) current as of the ICRP’s 2005 Recommendations [8]

Type of Radiation	Radiation Weighting Factor, w_R
Photons	1
Electrons, muons	1
Protons	2
Alpha particles, fission fragments, heavy nuclei	20
Neutrons	$2.5 + 18.2e^{-(\ln E_n)^2/6}$ for $E_n < 1\text{MeV}$ $5.0 + 17.0e^{-(\ln(2E_n))^2/6}$ for $E_n \geq 1\text{MeV}$

Table 2: Summary of tissue weighting factors (w_T) current as of the ICRP’s 2005 Recommendations [8]

Tissue	w_T
Bone marrow, Breast, Colon, Lung, Stomach	0.12
Bladder, Oesophagus, Gonads, Liver, Thyroid	0.05
Bone surface, Brain, Kidneys, Salivary glands, Skin	0.01
Remainder Tissues* (Nominal w_T applied to the average dose to 14 tissues)	0.10

*Remainder Tissues (14 in total): Adipose tissue, adrenals, connective tissue, extrathoracic airways, gall bladder, heart wall, lymphatic nodes, muscle, pancreas, prostate, small intestine wall, spleen, thymus, and uterus/ cervix

Effective dose is calculated by “*first weighting the absorbed dose according to the biological effectiveness of the different radiation qualities with a w_R* ” [8] and then summing “*the radiation weighted doses to the various tissues and organs of the human body, modified by the w_T* ” [8]. The expression for effective dose, given in units of Sieverts (Sv), is presented below in Equation 9.

$$E = \sum_T w_T \sum_R w_R D_{T,R} \quad [\text{units: Sv}] \quad (9)$$

2.1.5. Acceptable exposure limits

In order to help protect people from the harmful effects of radiation, the ICRP publishes strict guidelines identifying the acceptable exposure limits for both nuclear energy workers (NEW) and the general population. According to the 1990 Recommendations of the ICRP, NEWs may receive a dose of 100 mSv over a period of five years, with a maximum dose of 50 mSv in any one of those years being deemed acceptable [9]. As one might expect, the ICRP also advises that the general population is to receive a much smaller dose of 1 mSv per year above that contributed by natural background radiation [9].

NATO has also issued its own series of guidelines outlining acceptable radiation exposure state (RES) categories for military personnel responding to radiological events. As Table 3 illustrates, for a radiological incident, members are allowed to receive a certain dose corresponding to the RES category assigned to that event [10]. The RES categories allow commanders to understand the amount of radiation that their personnel have been exposed to during previous missions and outline recommended actions for assigning tasks in a radiation environment. It should be noted that the doses presented in Table 3 correspond to the acceptable limit that can be received in response to a single event and not a given time period [10].

Table 3: Radiation exposure state categories and corresponding dose limits [10]

RES Category	Total Cumulative Dose (mSv)
0	0 - 0.5
1A	0.5 - 5
1B	5 - 50
1C	50 - 100
1D	100 - 250
1E	250 - 750

2.2. Personal Protective Equipment

In order to help meet these acceptable exposure limits, various types of commercial personal protective equipment (PPE) are marketed with the ability to reduce wearer exposure to radiation hazards by either attenuating incident radiation or isolating the wearer from radioactive particulates. Moreover, due to the harsh and constantly-evolving threats facing first responders and military personnel during a radiological hazard scenario, PPE is essential to ensuring these individuals can carry out their jobs confidently, safely, and efficiently in a variety of different environments and conditions. Traditionally, PPE includes any type of garment, helmet, glove, boot, goggle, or other piece of individual equipment that is designed to protect the wearer or user from injury caused as a result of blunt force trauma, high-speed impact collisions, electrical hazards, chemical spills, infection, exposure to unsafe levels of radiation, or any other potential health threat [11]. It is necessary to clarify that, with regards to this project, only PPE suits are being considered and the sole parameter of interest is the extent to which these suits are able to provide protection to the wearer in the event of radiological exposure. This project will primarily focus on the general type of PPE suit currently employed by the CAF for chemical, biological, radiological, and nuclear (CBRN) operations and on a second generation commercial radio-opaque combat (CRC) suit that is used by civilian emergency response teams and NEWs.

2.2.1. Types of PPE suits

2.2.1.1. Air permeable PPE suit

The Horizon 1 Chemical Warfare Coverall (CWC) is currently used by the CAF as the basic CBRN protection suit. It consists of a hooded, one-piece garment that is used in tandem with over boots, gloves, and a gas mask or other such respirator [11]. The garment itself consists of two separate layers and is air permeable [12]. The outer layer of the suit is designed to repel water and liquid chemical agents, whilst the purpose of the inner layer is to absorb chemical agent vapours using activated charcoal [12]. Energy-dispersive X-ray (EDX) spectroscopy indicates that the outer layer of the suit is composed of 31.1 wt% oxygen and 67.2 wt% carbon [13]. Similar analysis has determined the composition of the inner layer to be 18.6 wt% oxygen and 81.1 wt% carbon [13]. Instrumental neutron activation analysis (INAA) has further identified trace amounts of calcium (0.3 wt%) and copper (0.057 wt%) in the elemental make-up of the suit [13]. It has been shown that the Horizon 1 CWC does not attenuate even low energy gamma photons or neutrons and, as such, does not provide any increase in radiological protection outside of the degree to which it prevents airborne radioactive particulates from reaching the skin [13]. Figure 2 depicts a CAF member wearing the Horizon 1 CWC.



Figure 2: CAF member modelling the Horizon 1 CWC, adapted from [11]

2.2.1.2. Air impermeable PPE suit

CRC suits are specifically designed to protect first responders, emergency personnel, and members of the nuclear and medical industries from the harmful effects of radiation. For the purpose of discussion, a generic second generation CRC suit is described in the text that follows. The second generation CRC suit consists of three distinct layers in which fibres of metallic polymer are sandwiched between an outer layer of woven, cellulose-based manufactured fibres and an inner layer of synthetic fibres [14]. The middle layer of the suit is commonly manufactured by impregnating a polyethylene-based polymer filler with nanoparticles of radio-opaque metals, such as bismuth or tungsten [15]. The resulting polymer can then be extruded to form long, thin filaments that are suitable for inclusion within the garment [15]. The addition of bismuth and tungsten is significant as these metals have high mass attenuation coefficients which afford the suit improved radiological protection capabilities; moreover, experimentation has shown that the CRC suit can attenuate low energy gamma photons [14]. Unfortunately, experimentation further indicates that this protection does not extend to higher energy photons or neutrons [13, 14]. It is important to note that the suit is air impermeable and is designed with heat-sealed seams and

seam-seal tape to guard against leaks from improperly sealed closures [11]. Consequentially, the second generation CRC suit may be classified as part of a C2 Ensemble according to the Z1610 standard published by the Canadian Standards Association (CSA) and meets the National Fire Protection Association (NFPA) 1994 Class 2 protection requirement [16]. This designation means that the suit is designed such that it offers a moderate degree of protection against vapor and liquid agents as specified under the standard and, as a result, also protects against aerosols to a reasonably high but undetermined level [16]. A traditional CRC suit is shown in Figure 3.



Figure 3: Traditional CRC suit, adapted from [11]

2.3. Aerosols

2.3.1. Properties of aerosols

An aerosol is defined as a collection of solid or liquid particles that are suspended in some type of gaseous medium [17]. In the simplest sense, aerosols are two-phase systems consisting of particulate matter and the suspension medium and can be envisioned as phenomena such as fog, dust, haze, smog, or mist [18]. There is no strict scientific method used to classify aerosols; however, they are commonly subdivided according to the physical form of the particulates making up the aerosol or based on the method in which the aerosol is generated [17]. In this respect, particulate size is the most important parameter in determining aerosol behaviour [17]. Outside of laboratory conditions, it is very rare for the particulates of an aerosol to be one size or monodisperse [18]. Most aerosols are composed of

particulates encapsulating a wide range of sizes and are said to be polydisperse [18]. This must be taken into account when analyzing an aerosol because the fundamental natural laws governing the behaviour of these particulates also change with size [17]. It should be noted that the particulate size actually refers to the diameter of the species and commonly ranges from less than 0.1 μm to greater than 10 μm . Particulates with a diameter greater than 10 μm often have limited stability in the atmosphere, but still represent a significant source of occupational exposure to workers who are in close proximity of the source [17]. When discussing particulate diameter, care must be taken to distinguish between physical or geometric diameter and aerodynamic diameter. Geometric diameter refers to the size that would be measured under a microscope; however, this poses a dilemma if the particulate is not of a spherical shape [18]. Because most real world airborne particulates are not spherical, it is necessary to normalize their diameter by some quantity, such as shape or density, to allow for a consistent standard of comparison [17]. To this end, the aerodynamic diameter, d , of a particulate is defined as the diameter of a spherical water droplet that has the same settling velocity as the original particulate and is the diameter most commonly quoted when discussing aerosol behaviour [17]. From this point forward, any discussion of particulate diameter or size refers to the aerodynamic diameter unless otherwise stated. Another commonly measured aerosol property, and one of primary importance when determining health effects and exposure limits, is concentration [18]. Concentration can be defined in terms of both mass and particulate number. Mass concentration refers to the mass of particulate matter in a volume of aerosol, whilst number concentration denotes the number of particulates per unit volume of aerosol [17]. These values are commonly measured in units of $\mu\text{g m}^{-3}$ and number m^{-3} , respectively. As discussed in the coming sections, both particulate diameter and concentration play a significant role in particulate transport.

2.3.2. Aerosol mechanics

As described above, an aerosol consists of a collection of particulates that are suspended in some form of gaseous medium. As one might expect, the motion and behaviour of these particulates within the aerosol is predominantly dictated by that of the suspending gas and is strongly influenced by particulate size [18]. Particulates smaller than 0.1 μm in diameter are regularly affected by the motion of individual gas molecules, meaning that the kinetic theory of gases can be applied to predict and describe their behaviour [19]. This region is commonly referred to as the free molecular regime [19]. The motion of large particulates is most commonly associated with the continuum regime, a continuous gas or fluid medium that is best defined using conventional gas or fluid dynamic equations [19]. Finally, intermediate-sized particulates, falling within the transition or slip regime, are treated by incorporating correction factors into the equations used to define motion

in the continuum region [19]. The following section presents a brief overview of the most pertinent theories and mechanisms describing particulate motion.

2.3.3. Uniform particulate motion

The most common type of airborne particulate motion is uniform, straight-line motion [17]. The analysis of this type of motion is extremely valuable as, under most conditions, airborne particulates will achieve a steady-state velocity almost instantaneously [17]. During uniform motion, the external forces causing the particulate to move are opposed and balanced by the particulate's aerodynamic drag force [19]. This force relates the resistive forces acting on the gas to the velocity pressure created as a result of the relative motion between the particulate and the surrounding gas [19]. The equation defining the aerodynamic drag force experienced by a particulate is known as Stokes' law and represents a solution to the Navier-Stokes equations describing fluid motion [17]. Because the Navier-Stokes equations are nonlinear partial differential equations, Stokes had to make several assumptions to attain a solution. Stokes' law assumes that the inertial forces are negligible compared to the viscous resistance forces, the surrounding gas is incompressible, there are no neighbouring walls or particulates, the particulate is a rigid sphere, the velocity of the gas at the surface of the particulate is zero, and there is uniform particulate motion [17]. Equation 10 represents the simplest form of Stokes' law.

$$F_{drag} = 3\pi\eta Vd_p \quad (10)$$

Stokes' law illustrates that the aerodynamic drag force, F_{drag} , experienced by a particulate is dependent upon its velocity, V , diameter, d_p , and the dynamic viscosity of the surrounding gas, η [17]. It should be noted that various correction terms can be applied to Equation 10 to account for deviations away from some of the aforementioned assumptions, but have not been included here in the interest of brevity [17].

Another commonly referenced parameter that can influence particulate motion is the Reynolds number [17]. The Reynolds number is defined as the ratio of the inertial force of the fluid to the frictional forces that are generated as a result of movement over a surface and provides a standard for determining whether the flow profile is laminar or turbulent [19]. As presented in Equation 11, the Reynolds number, Re , is directly proportional to the density of the fluid, ρ_g , the velocity of the fluid, V , and the characteristic linear dimension of the environment, d , and is indirectly proportional to the dynamic viscosity of the fluid, η [17].

$$Re = \frac{(\rho_g)(V)(d)}{\eta} \quad (11)$$

For pipe or annuli, laminar flow exists for $Re < 2000$, whilst turbulent flow occurs for $Re > 4000$ [17]. Under laminar conditions, the fluid flow is considered to be smooth and the individual streamlines do not circle back on themselves; contrastingly, turbulent flow is characterized as being chaotic with looping streamlines and strong inertial forces [19]. In the intermediate region, the flow profile is dominated by the prior behaviour of the fluid [19]. It is important to note that the flow Reynolds number and particulate Reynolds number define two distinct quantities. The former defines overall fluid flow conditions in a tube or channel, whilst the latter outlines the flow profile that occurs around an individual particulate located within the fluid itself [19]. Due to the fact that the vast majority of particulates making up an aerosol follow the streamlines created by the overall fluid flow, the flow Reynolds number will be an important parameter for describing their motion and must be considered when determining particulate deposition rates.

2.3.4. Deposition of airborne particulates

The rate at which airborne particulates deposit out of the air on various surfaces, be it skin, hair, clothing, or structural elements, must be considered when describing particulate motion as it has a significant impact when determining health effects and exposure limits. In most instances, it is common to express the rate of particulate deposition in terms of a deposition velocity that represents the effective velocity at which particulates move towards a surface [17]. As presented in Equation 12, deposition velocity, v_{dep} , is defined as the depositional flux of particulates on a surface, J , relative to the undisturbed number of particulates in the surrounding environment, n_0 .

$$v_{dep} = \frac{J}{n_0} \quad (12)$$

There are a number of factors that influence deposition velocity: particulate size, surface texture, surface motion, surface moisture, and whether the particulates are being transported via turbulent or laminar fluid flow [20]. There is a direct relationship between particulate size and deposition velocity, namely, that an increase in particulate size corresponds to an increased deposition velocity [21]. Surface texture can also impact deposition velocity. In this regard, experimentation has determined the deposition velocities on various surfaces as a function of particulate diameter [21]. The effects of both particulate diameter and surface texture on deposition velocity are shown in Table 4. It is more difficult to quantify the effects of surface motion and surface moisture on deposition velocity; however, experimentation has shown that the deposition velocities presented in Table 4 increase by a factor of two if the individual is moving or sweating [21]. Whether the particulates are transported via turbulent or laminar fluid flow will also impact

their deposition velocity [22]. Again, numerous studies have been conducted to determine the deposition velocities of particulates under various flow conditions. Not surprisingly, the values presented in the literature vary greatly and it is difficult to generalize as each study is based on a unique set of experimental parameters [22]. As a result, when attempting to determine the deposition velocity for a given set of conditions, it is best to select the data from the experimentation that best mimics the conditions of interest as opposed to attempting to apply a global trend.

Table 4: Best general estimate of deposition velocities on various surfaces as a function of particulate diameter [21]

Deposition Velocity / m s ⁻¹	Particulate Diameter / μm		
	0.7	4	10
Human Skin	1.0 x 10 ⁻³	1.2 x 10 ⁻²	3.0 x 10 ⁻²
Human Hair	2.6 x 10 ⁻⁴	3.0 x 10 ⁻³	-
Clothing	1.7 x 10 ⁻³	2.7 x 10 ⁻³	5.0 x 10 ⁻³

An important component of deposition velocity is gravitational settling. Gravitational settling occurs as a result the earth's gravitational field exerting a downward force on the particulate as it moves through the air [19]. After a short period of acceleration, the gravitational force is countered by the drag force of the air acting on the particulate and the particulate achieves a constant velocity. This velocity is known as the terminal settling velocity and can be derived by equating the gravitational force acting on the particulate with the drag force resisting its downward motion [19]. For particulates with a diameter greater than one micrometer, the terminal settling velocity, v_{TS} , can be calculated as per Equation 13, where g is the acceleration due to gravity and the remaining variables are unchanged as defined in Section 2.3.3.

$$v_{TS} = \frac{\rho_p d_p^2 g}{18\eta} \quad (13)$$

Equation 13 illustrates that terminal settling velocity is proportional to the particulate diameter, d_p , squared and, as such, drastically increases with particulate size [17]. In general, gravitation settling is only significant in instances involving relatively large particles and slow streamline velocities [17]. It should be noted that Equation 13 can also be used to determine the terminal settling velocity of smaller particulates ($d_p < 1 \mu\text{m}$) by including a correction factor in the numerator [17].

2.3.5. Collection of airborne particulates by PPE fabrics

From a radiation protection standpoint, PPE suits are important as they aim to attenuate some of the incident radiation and, thus, lower the dose imparted to the

wearer of the suit. That being said, the attenuation of incident radiation is not the only way in which PPE suits provide protection from airborne radioactive particulates during a radiation hazard scenario. The suits themselves, if impermeable to air and having good closures, prevent airborne particulates from reaching the skin. The fabrics making up these suits are also able to collect the particulates as they attempt to pass through the suit or as they graze the surface of the fabric itself. This creates a protective barrier that separates the skin of the wearer from the radioactive particulates in the surrounding environment.

There are three main mechanisms by which PPE fabrics are able to collect airborne particulates: impaction, interception, and diffusion deposition mechanisms [23]. As shown in Figure 4, impaction occurs when a particulate, due to its inertia, “is unable to adjust quickly enough to the abruptly changing streamlines near the fibre and crosses those streamlines to hit the fibre” [17]. This mechanism predominately takes place for particulates with a diameter greater than $0.5 \mu\text{m}$ as the larger diameter results in a greater particulate inertia and velocity [23].

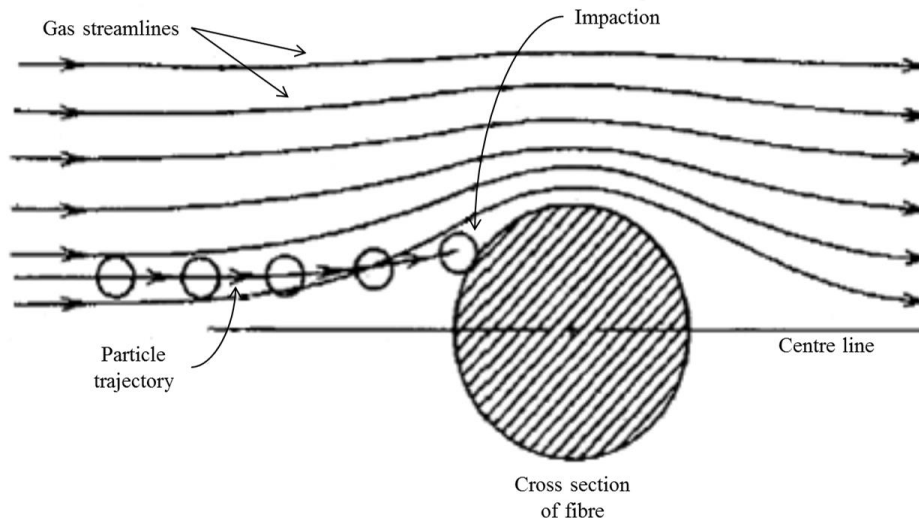


Figure 4: Collection of particulates via the impaction mechanism, adapted from [17]

Interception occurs when a particulate “follows a gas streamline that happens to come within one particle radius of the surface of a fibre” [17]. As a result, the particulate hits the fibre and is captured. As Figure 5 illustrates, only particulates travelling along certain streamlines will be collected; however, this assumes that the particulates have negligible inertia, settling, and Brownian motion effects [17]. Interception is the only deposition mechanism that does not involve the particulate

departing from its initial gas streamline [17]. Particulates with diameters in the 0.1-0.5 μm range are mainly collected by this mechanism [23].

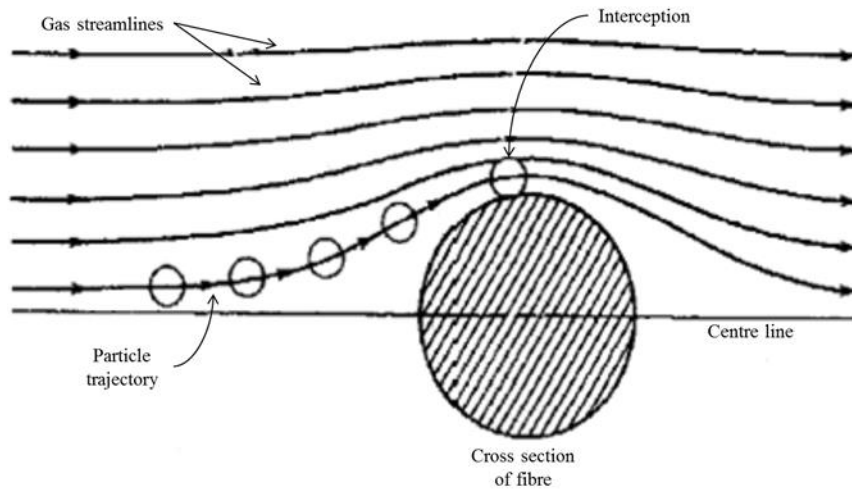


Figure 5: Collection of particulates via the interception mechanism, adapted from [17]

Diffusion is the prevailing collection method for particulates with a diameter of less than 0.1 μm [23]. Because the particulates in this range are so small, their Brownian motion is “sufficient to greatly enhance the probability of their hitting a fibre while travelling past it on a nonintercepting streamline” [17]. A schematic outlining the diffusion deposition mechanism is provided in Figure 6 [17].

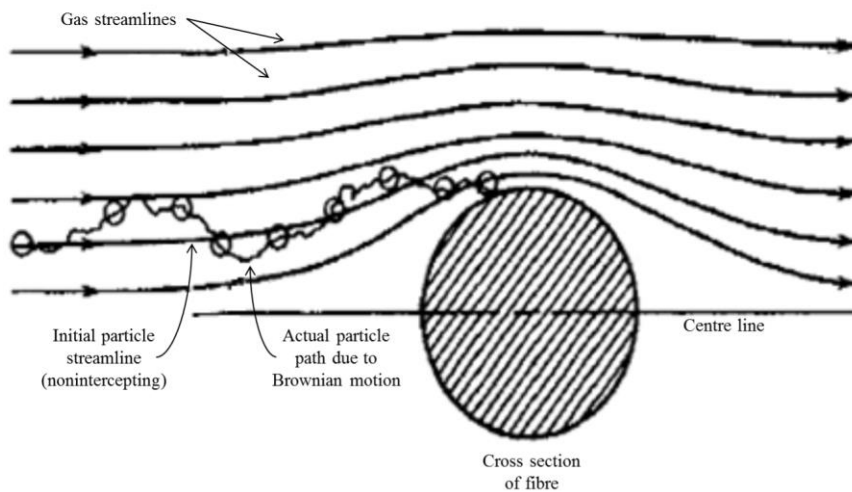


Figure 6: Collection of particulates via the diffusion mechanism, adapted from [17]

It should be noted that there are two other minor collection mechanisms, gravitational settling and electrostatic attraction, that have not been discussed at this point. The reason for their omission is the fact PPE suits collect airborne particulates much less frequently via these processes [17]. Gravitational settling is significant when describing airborne particulate behaviour, as discussed in Section 2.3.4, but is not considered to be a significant collection mechanism [17]. Electrostatic attraction is often neglected unless both the particulates and suit fibres have been charged in a quantifiable manner at the microscopic level and, as such, is neglected in the present work [17].

The ability of an air permeable fabric to collect airborne particulates is dependent on a variety of intrinsic characteristics, including material penetration, structure, thickness, and air permeability [23]. Based on these factors, for any given such fabric, it is important to note that there is a most penetrating particulate size (MPPS) that corresponds to the particulate size that is most likely to avoid collection while passing through the fabric [23]. In theory, air impermeable fabrics should not allow any particulates to pass through the protective boundary of the suit; however, penetration may still occur through fabric tears or improperly sealed seams or closures and particulate capture may subsequently occur on inner fabric surfaces.

2.4. Particulate Transport Theory

A large portion of this project is based on determining the concentration of radioactive particulates in different regions surrounding a sleeved forearm, both within and outside of the PPE fabric, during radiological exposure. As such, having outlined how airborne particulates deposit on and are collected by PPE fabrics, it is now necessary to investigate fundamental particulate transport theory and the factors that can influence this phenomenon.

There are two distinct modes by which mass can move from one location to another: convective mass transfer and diffusion [24]. Because this project considers the transport of radioactive particulates across an air-permeable fabric, a detailed understanding of the diffusion process is required; that being said, convective mass transfer will also be incorporated into the final particulate transport model as this is the governing process by which the particulates are moved into and out of the suit. Convective mass transfer is the dominant process at locations far away from the fabric-surrounding environment interface and is heavily influenced by convective fluid flow [24]. Diffusion occurs in the regions very close to the phase interface where the convective fluid flow is somewhat suppressed [24]. It can be defined as the random movement of molecules on the microscopic scale due to thermal energy and is responsible for the detailed mixing of two materials [24]. In this sense, a concentration difference between two regions gives rise to a net movement

of species from that of higher concentration to that of lower concentration [24]. This concept is the driving force behind Fick's first law of diffusion.

2.4.1. Fick's first law of diffusion

On a fundamental level, particle transport is governed by Fick's first law. As shown in Equation 14, Fick's first law states that the diffusive flux of species A, J_A , is proportional to the diffusion coefficient, D , and concentration gradient of that species, $\frac{dc_A}{dx}$ [25].

$$J_A = -D \frac{dc_A}{dx} \quad (14)$$

Equation 14 is valid for any binary solid, liquid, or gas solution so long as the diffusive flux is defined relative to the overall mixture velocity [25]. Fick's first law is only applicable to steady state diffusion or situations in which the concentration of the species of interest remains constant with time [24]. Because this project is interested in scenarios where the concentration of radioactive particulates changes with time at various locations surrounding a human forearm, it is necessary to move to Fick's second law.

2.4.2. Fick's second law of diffusion

Fick's second law of diffusion is applicable to non-steady state diffusion situations and can be derived from Fick's first law. To start, consider the differential element presented in Figure 7.

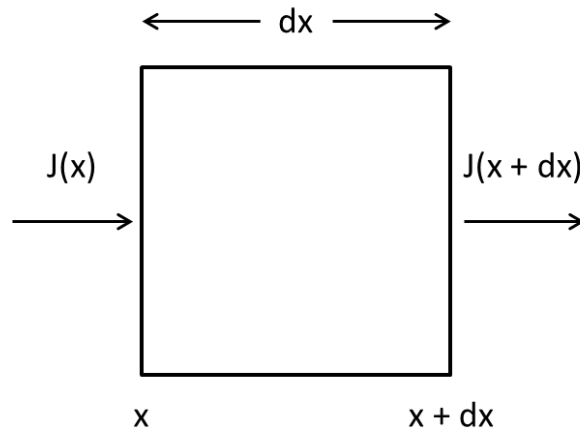


Figure 7: Differential element used in the derivation of Fick's second law of diffusion

The diffusive flux entering the element is simply $J(x)$; however, leaving the element, the flux will be equivalent to $J(x)$ plus the change, $\frac{dJ(x)}{dx}$, over the differential distance dx . This representation is shown in Equation 15.

$$J(x + dx) = J(x) + \frac{dJ(x)}{dx} dx \quad (15)$$

Next, the rate of change of the concentration, $\frac{dc(x,t)}{dt}$, within the differential element is equivalent to the change of the diffusive flux over the differential length.

$$\frac{dc(x,t)}{dt} = \frac{J(x) - J(x+dx)}{dx} \quad (16)$$

Equation 16 can now be simplified through the substitution of Equation 15.

$$\frac{dc(x,t)}{dt} = - \frac{dJ(x)}{dx} \quad (17)$$

Again, Equation 17 can be simplified by incorporating Fick's first law (Equation 14) in place of the diffusive flux term.

$$\frac{dc(x,t)}{dt} = D \frac{d^2c}{dx^2} \quad (18)$$

Equation 18 presents a simplified, one-directional version of Fick's second law of diffusion. This expression can be generalized to account for multi-directional diffusion by incorporating the del operator, ∇^2 , as shown in Equation 19 [25].

$$\frac{dc}{dt} = D \nabla^2 c \quad (19)$$

Essentially, the generic version of Fick's second law states that the rate of change of the concentration, $\frac{dc}{dt}$, is proportional to the diffusion coefficient, D , and the rate of change of the concentration gradient, $\nabla^2 c$ [25]. This is a slight simplification however, as there are other factors that can affect how the concentration of a species changes with time. In this regard, factors such as the convection term, $v^* \cdot \nabla c_A$, and rate of reaction, R_A , are often included in the expression for Fick's second law of diffusion [25]. Equation 20 illustrates Fick's second law with the inclusion of both the convection and rate of reaction terms for some species [25].

$$\frac{dc_A}{dt} + v^* \cdot \nabla c_A = D \nabla^2 c_A + R_A \quad (20)$$

Because the radioactive particulates being investigated in this project are not involved in any significant reactions, the rate of reaction term can be equated to zero; however, the convective term, consisting of the molar average velocity, v^* , will be included as it mirrors the effects of wind outside the suit and bellows effects into and out of the suit closures on the airborne radioactive particulates. Thus, Equation 21 depicts the expression for Fick's second law that is used in this thesis [25].

$$\frac{dc_A}{dt} + v^* \cdot \nabla c_A = D \nabla^2 c_A \quad (21)$$

By solving this equation, it is possible to determine the concentration of radioactive particulates at different locations as a function of time.

2.4.3. Factors affecting diffusion

As evidenced by its inclusion in both Fick's first and second laws of diffusion, one of most important variables when determining the diffusivity of an airborne particulate through a fabric is the diffusion coefficient of the fabric, D_f . For air permeable fabrics, the diffusion coefficient can be determined using Equation 22 [17]. In Equation 22, k denotes the Boltzmann constant, T is the temperature, d_p is the diameter of the particulate, η is the dynamic viscosity, and C_c is the Cunningham slip correction factor. The Cunningham slip correction factor must be applied for particulates with a diameter less than 1 μm as these species will settle faster than predicted on account of the 'slip' that occurs at the surface of the particulates and is highly dependent on the mean free path, λ , of the particulate [17].

$$D_f = \frac{kTC_c}{3\pi\eta d_p} \quad (22)$$

where

$$C_c = 1 + \frac{2.5\lambda}{d_p} \quad (23)$$

Equation 22 illustrates that the diffusion coefficient for a fabric is inversely related to the diameter of the particulates passing through it. Based on this relationship, it follows that smaller particulates will diffuse through an equivalent medium more quickly than large particulates. In this regard, Equation 22 demonstrates the importance that particulate size has on the concentration profile of airborne particulates across a PPE suit boundary. It should be noted that Equation 22 can also be applied to calculate the diffusion coefficient of other media, such as air, by simply using the parameters associated with the medium of

interest. As one might suspect, the diffusion coefficient for an air impermeable fabric is zero.

Hydrostatic force is another important parameter to consider when evaluating the diffusion of particulates across an air permeable fabric and or through leaks in air impermeable fabric closures [23]. Hydrostatic force is characterized by an air pressure difference across the fabric and originates as a result of wind or air movement against the body [23]. The pressure drop across the fabric is the sum of the resistance caused by each individual fibre on the localized air flow [17]. The resulting discrepancy between the high-pressure region outside and low-pressure region inside of the suit generates a hydrostatic force that is responsible for inducing air and particulate flow into the suit through the fabric itself or via leaks [23]. Such a process serves to increase the concentration of particulates within the protective confines of the PPE suit. Equation 24 illustrates how pressure drop, Δp , is directly proportional to viscosity, η , fabric thickness, t , free-stream velocity, U_0 , and fibre packing density, θ , and is inversely proportional to fibre diameter, d_f [17].

$$\Delta p = \frac{\eta t U_0 f(\theta)}{d_f^2} \quad (24)$$

where

$$f(\theta) = 64\theta^{1.5}(1 + 56\theta^3) \text{ for } 0.006 < \theta < 0.3 \quad (25)$$

Finally, given the right conditions, thermophoresis and electrostatic effects can affect particulate transport; however, such behaviour is extremely difficult to quantify and is often neglected due to its localized nature and limited impact on larger particulates [17]. As such, neither thermophoresis nor electrostatic effects are considered in the present work.

2.5. Radiation Hazard Scenarios

It is now necessary to outline the most common types of radiation hazard scenarios in order to highlight the reoccurring presence of radioactive particulates in these events and the serious health threat they cause. A brief historical account of the major radiological events that have occurred since the end of World War II has been included in order to provide context. An analysis of the most likely radiation hazard scenarios facing first responders and military personnel is then presented.

2.5.1. Evaluating radiological events

Throughout history, there have been numerous examples of nuclear-related accidents and incidents; however, the cause and effect of these events vary significantly. As a result, it can be very difficult to classify and compare radiological events. In order to help mitigate this problem, the International Atomic Energy Agency (IAEA) developed and introduced the International Nuclear and Radiological Event Scale (INES) in 1990 [26]. The INES classifies radiological events based on their impact on three areas: people and the environment, radiological barriers and controls at facilities, and redundant defence systems [26]. Due to its late implementation, the INES has been retrospectively applied to past radiological events for classification purposes. It is also important to note that the INES is a logarithmic based scale in which each subsequent level is ten times more severe than the one preceding it [26]. Figure 8 illustrates each of the INES levels.

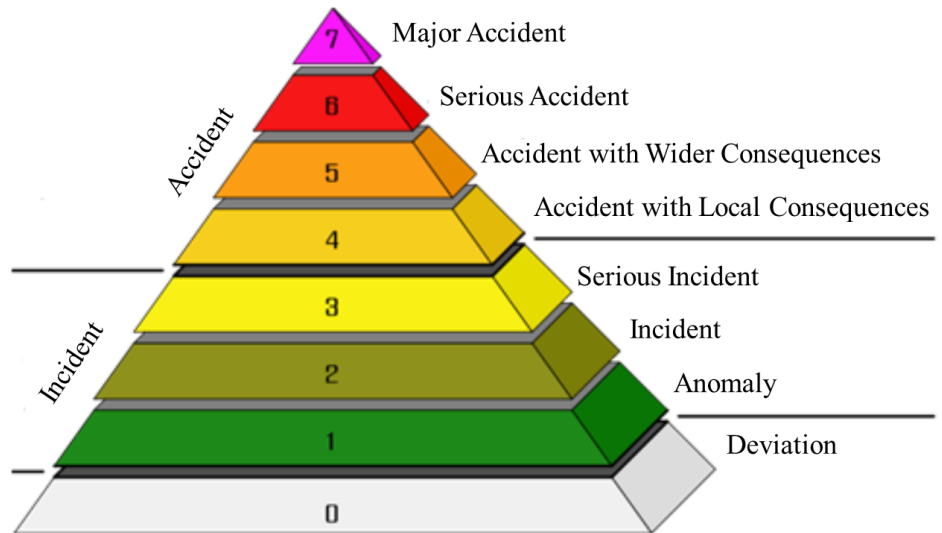


Figure 8: Levels making up the INES, adapted from [26]

2.5.2. Major radiological events since World War II

This section seeks to identify the major radiological events that have occurred world-wide since the end World War II. In the interest of brevity, it has been decided to limit the discussion to radiological events that were classified as Level 4 or higher according to the INES.

Less than seven years after the United States decided to drop nuclear bombs on the Japanese cities of Hiroshima and Nagasaki, the first major nuclear reactor

incident occurred. On December 12th, 1952, a combination of mechanical and human error led to a major power excursion that destroyed the core of the NRX reactor located in Chalk River, Ontario [27]. Five years later, a coolant system failure resulted in the partial destruction of a reactor containment vessel at a facility in Mayak, Russia. In both instances, significant quantities of radiological material were released into the surrounding environment [28]. According to the INES, the two accidents were classified as Level 5 and Level 6, respectively [27, 28].

The next major radiological event occurred on February 22nd, 1977 in Jaslovské Bohunice, Czechoslovakia when a worker forgot to remove the moisture-absorbing material from a fuel rod assembly [29]. The error caused the integrity of the fuel to be compromised, which resulted in extensive corrosion damage to the fuel cladding and the subsequent release of radioactive species into the plant area. Due to its localized nature, the event was characterized as Level 4 by the IAEA [29]. In 1979, one of the most publicised radiological hazard events took place at the Three Mile Island Nuclear Generating Station in Dauphin County, Pennsylvania. A loss of coolant accident (LOCA) caused a partial meltdown of the reactor core and required that radioactive gases be vented in order to reduce the pressure within the reactor [30]. The accident was assigned a Level 5 classification. In 1980, a Level 4 accident occurred at a facility in Orléans, France when a brief power excursion caused several fuel bundles to rupture and necessitated the local release of radioactive material [31]. Three years later, operator error resulted in a criticality excursion during the operation of the RA-2 research reactor in Constituyentes, Argentina [32]. Due to the localized nature of the event, it was classified as Level 4.

On April 26th, 1986, an uncontrolled power excursion occurred while performing safety tests at the Chernobyl Power Complex in Prypiat, Ukraine [33]. The power excursion caused severe steam and hydrogen explosions, a partial meltdown of the reactor core, and a massive release of radioactive particulates into the environment [33]. As a result of the explosion, hundreds of thousands of individuals had to be relocated away from the contamination zone and portions of the area are still unfit for inhabitation today. The Chernobyl accident is widely viewed as the worst nuclear disaster in history and was classified as Level 7 according to the INES.

Following the Chernobyl accident, it was several years before the next major radiological events. In 1993, a Level 4 scenario occurred in Tomsk, Russia when an unregulated pressure build-up caused a mechanical explosion that breached the stainless steel reaction vessel [32]. Fortunately, the release of radioactive material was limited to the immediate surroundings. The second instance was also classified as Level 4 and occurred in Tokai, Japan, in 1999, as a result of an accidental

criticality [32]. Similarly, the released fission products were contained within the facility.

The second Level 7 classification was assigned to the reactor meltdown that took place at the Fukushima Daiichi Nuclear Power Plant on March 11th, 2011 [33]. A 9.0 magnitude earthquake triggered a large tsunami that overcame the seawall designed to protect the six boiling water reactors located at the facility. The sea water eventually flooded the emergency generators and other electrical equipment needed to pump coolant throughout the system. As a result, three of the reactors at the facility experienced complete meltdown and hydrogen gas explosions, while others began to leak contaminated water [33].

It is important to note that the improper disposal of radionuclide sources has also resulted in numerous radiological incidents since the 1960s. On account of their high degree of localization, often impacting only a handful of individuals, disposal events do not garner as much significance as nuclear reactor events based on the INES; nonetheless, situations involving the improper disposal of radionuclide sources must be mentioned due to their frequent occurrence around the world. Such events have occurred in Mexico (1962), Morocco (1984), Brazil (1987), and Egypt (2000) [34]. In each case, a radionuclide source was either stolen from an abandoned radiotherapy centre or recovered from a local waste-storage facility. At this point, the protective capsule around the source was then removed or breached, resulting in localized radiological exposure to a small group of people.

2.5.3. Classification of radiological hazard scenarios

It is evident that the aforementioned events, ranging from full scale nuclear reactor meltdowns to the improper disposal of radionuclide sources, drastically differ in cause and severity; nonetheless, looking at the historical data, it is also clear that certain radiological hazard events occur more frequently than others. With this in mind, NATO has identified four prominent radiological hazard scenarios, encompassing each of the main types of radiation, that pose a significant health threat on account of their propensity to release airborne radioactive particulates into the immediate environment [35].

According to NATO, the radiation hazard scenario of greatest concern involves the deliberate dispersal of radiological material such as a terrorist act involving the detonation of a radiological dispersion device (RDD) [35]. Caesium-137 (Cs-137), in the form of caesium chloride, has been identified as the material best suited for use in a RDD as it emits moderate energy gamma photons and beta particles, is often in a powder form, and is water soluble [35]. Strontium-90 (Sr-90), a beta emitter, has also been flagged for dirty bomb suitability as it is often used as a

source in radioisotope thermoelectric generators (RTG) and, thus, could be readily accessible [35]. In much the same manner, cobalt-60 (Co-60) is the radionuclide most commonly used in industrial irradiators and could easily be used as the radiological source material in an RDD [35]. Co-60 emits high energy gamma photons and low energy beta particles [36]. Regardless of the source radioisotope, the deliberate dispersal of radiological material is especially concerning for major urban areas as their high population densities mean that even a localized dirty bomb could put many people at risk. Figure 9 illustrates the localized effects of a radiation hazard scenario involving the deliberate dispersal of radiological material.



Figure 9: Mock radiation hazard scenario involving the deliberate dispersal of radiological material, adapted from [37]

The loss or improper disposal of a radioisotope source represents the second most prominent radiological hazard scenario [35]. Many industrial-purpose irradiators, such as food sterilization irradiators or radiotherapy irradiators, use Co-60 sources [35]. Unfortunately, in many developing nations, there are no regulations regarding the proper disposal of these machines. As a result, many irradiators are simply abandoned or sent to the dump where it is not uncommon for individuals to come in contact with their highly radioactive contents. Once removed from their protective coverings, these sources are extremely radioactive and can be easily transported from one location to another, culminating in the accidental irradiation of countless unsuspecting individuals.

A tactical nuclear weapon strike is the third radiation hazard scenario outlined by NATO [35]. Such a scenario also includes a nuclear weapon incident involving the dispersal of plutonium-239 (Pu-239) by some sort of conventional explosive

[35]. Regardless, either situation involves the release of significant quantities of radioactive material into the environment [35]. It is also important to note that, during a nuclear weapon strike, many of the smaller radioactive particulates are released with sufficient energy to be carried up to high altitudes where they then disperse to low concentrations before returning to ground level [35]. Consequently, from a radiological perspective, the greatest external radiation threat is posed by the more massive radioactive particulates, which settle to ground level more quickly.

The final radiation hazard scenario identified by NATO is a nuclear reactor event akin to the Chernobyl disaster of 1986 or, more recently, the Fukushima Daiichi disaster of 2011 [35]. Serious nuclear reactor events are often characterized by breaches in the protective containment vessel that surrounds the reactor. These breaches are most commonly the result of necessary venting to mitigate dangerous pressure build-ups or hydrogen gas explosions; nonetheless, they facilitate the release of large quantities of multiple radionuclides into the surrounding environment [35]. At this point, the airborne radioactive particulates are easily influenced by local weather conditions and can be transported great distances. Figure 10 illustrates how radioactive particulates released during a nuclear reactor event can have severe health implications for a broad geographical area [35]. The release of highly radioactive fission products is also of special concern for this type of hazard scenario.

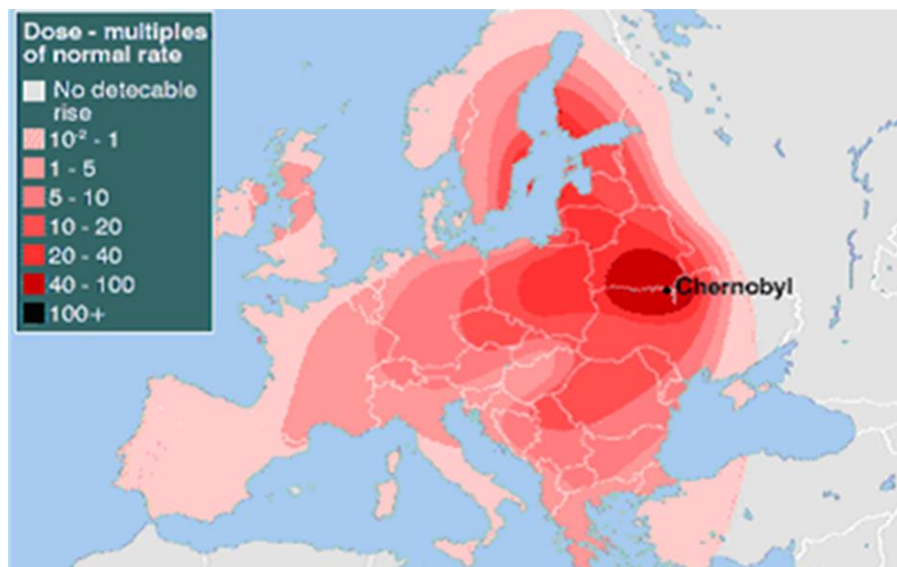


Figure 10: Geographical health implications of radioactive particulates released during a nuclear reactor event, adapted from [38]

3. PROJECT METHODOLOGY

The objective of this thesis is to create a realistic dosimetric model of the human forearm, protected by a PPE sleeve, which can be used as a tool to assess the dose imparted to the arm during a radiation hazard scenario. To achieve this objective, a two-fold modelling approach is employed. The first model uses fundamental particulate transport theory in order to determine the concentration of radioactive particulates in five different regions surrounding the sleeved forearm and aims to replicate the conditions of a typical radiation hazard scenario. The regional concentration data obtained from the particulate transport model is then incorporated as source terms in the second model. The second model is a dosimetric model that uses the Monte Carlo N-Particle (MCNP) transport code to determine the dose that is imparted to the forearm tissue. In this manner, it is possible to determine the dose imparted to a sleeved forearm as a result of exposure to a radiation hazard scenario and allows for comparison with the recommended acceptable exposure limits. Figure 11 provides a visual summary of the project methodology.

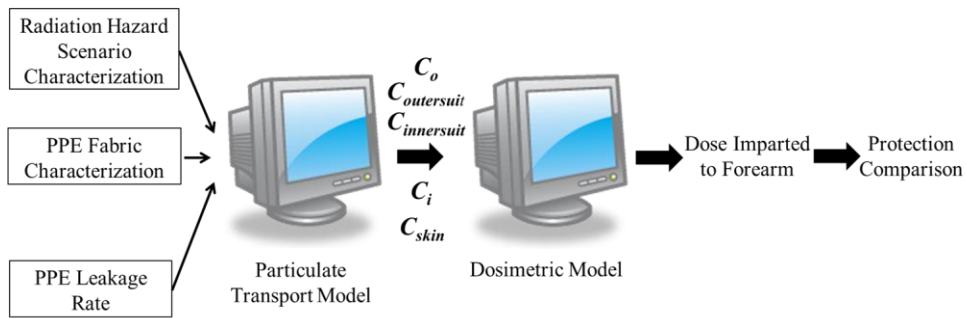


Figure 11: Schematic of project methodology

It was decided to apply a modelling approach for both the particulate transport and dosimetric aspects of this project, in place of conducting actual physical experiments, for several reasons. Firstly, due to the sensitive nature of radiological material, it is often difficult to obtain regulatory permission and comply with mandated safety and security requirements. Another important factor is cost. Because the radiation hazard scenarios being investigated involve large quantities of radionuclides, differing in type and particulate size, as well as multiple PPE suits of differing properties, it is more economical and efficient to construct computer-based models that can simulate the actual physical conditions of interest from a particulate transport and dosimetric standpoint. In this regard, by designing each model such that the user can specify and change the various input parameters as desired, one model can be used to represent numerous real world scenarios. That

being said, as a large portion of this project is based on computer modelling and simulation, it was also necessary to conduct benchmarking experimentation to ensure the suitability of each of the modelling software used in the development of the respective particulate transport and dosimetric models.

3.1. Particulate Transport Model

Recall that the primary objective of the particulate transport model is to determine the concentration of radioactive particulates in five different regions surrounding the sleeved forearm in response to radiological exposure. In this regard, the particulate transport model consists of a human forearm, protected with a sleeve of some sort of PPE fabric, which is immersed in an environment filled with airborne radioactive particulates. Applying Fick's second law of diffusion (Equation 21) to this scenario, it follows that at the initial time, t_0 , there is a concentration of radioactive particulates in the air outside of the sleeved forearm. This concentration will be referred to as concentration outer, C_o , for the remainder of the thesis and is dependent on the specific radiation hazard scenario being modelled. Figure 12 illustrates the location of C_o relative to the forearm and PPE sleeve.

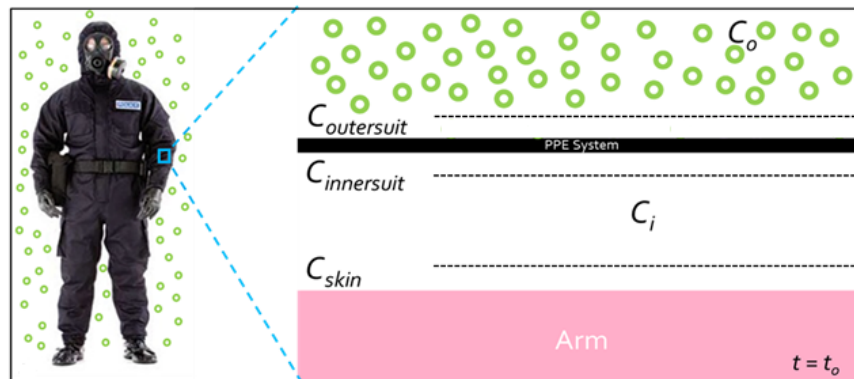


Figure 12: Location of radioactive particulates at t_0

Over time, the airborne particulates deposit on to the PPE sleeve at a rate that is dependent on their deposition velocity for clothing. As a result, there is now a concentration of radioactive particulates on the outer surface of the PPE sleeve, which will henceforth be identified as the concentration outer suit, $C_{outersuit}$. Additionally, some of the particulates will begin to diffuse through the fabric at a rate that is proportional to the diffusion coefficient of the fabric and the rate of change of the concentration gradient across its boundary. This is only possible for air permeable fabrics (CBRN suit) as air impermeable fabrics (second generation CRC suit) are designed to prevent penetration and have a diffusion coefficient of

zero. That being said, it is possible for radioactive particulates to enter air impermeable PPE suits through leaks and gaps in improperly sealed closures or fabric tears. In either case, the result is a concentration of radioactive particulates in the air gap between the arm and PPE sleeve. This concentration will be referred to as concentration inner, C_i . In much the same way as the outer airborne particulates deposited on to the outer surface of the PPE sleeve, the particulates within the PPE sleeve are able to deposit on to the inner surface of the PPE sleeve and the surface of the arm; moreover, the rate at which they do so depends on their deposition velocities for clothing and skin respectively. The former will be known as the concentration inner suit, $C_{innersuit}$, and the latter as concentration skin, C_{skin} . Figure 13 illustrates the locations of each of the five regional concentration values relative to the forearm and PPE sleeve.¹

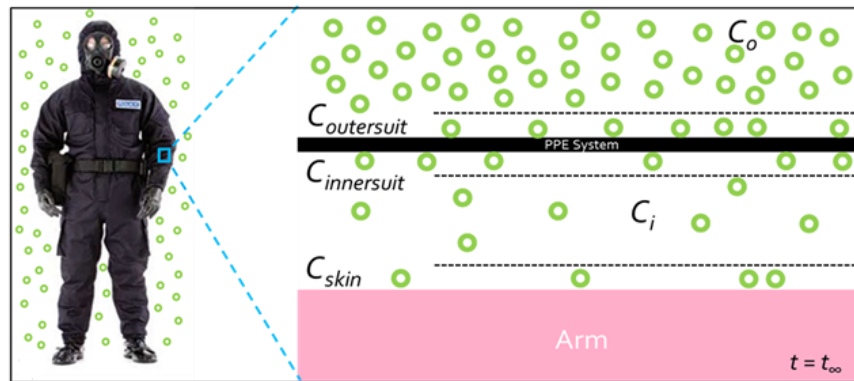


Figure 13: Location of radioactive particulates at t_{∞}

There are a variety of different methodologies that could be employed to construct the particulate transport model and solve for the five aforementioned regional concentration values. The first approach would be to use a computational fluid dynamics (CFD) software platform to develop the model. This method would subsequently necessitate the completion of benchmarking experimentation to ensure that the software could be appropriately applied to simulate the real-world particulate transport phenomena and confirm its suitability for use in this thesis. The second approach would be to develop the model from first principles using the fundamental particulate transport theory presented in Section 2.3 and Section 2.4. Adopting this approach would require performing a search of the literature or completing additional experimentation to obtain data pertinent to the transport of particulates in the presence of both air impermeable and air permeable fabrics. This thesis assesses the viability of each of the methodologies described above.

¹ Note that the surface concentrations are in areal units (number per unit area) while the airborne concentrations are in volume units (number per unit volume).

The initial approach to develop the particulate transport model and obtain solutions for each of the five regional concentration values was to use the COMSOL Multiphysics software package (COMSOL Multiphysics®, Version 4.4, 27 November 2013); however, after numerous attempts to recreate the particulate transport benchmarking experimentation, it became apparent that the software was not as conducive to developing the model as originally anticipated. The COMSOL Multiphysics software and the reasons for deciding to move on to the second particulate transport modelling approach are discussed in Section 5.1. Given the time limitations of this project, it was then decided to perform a search of the literature in order to obtain references and experimental data that could be used to assist in developing the particulate transport model as opposed to trying a different CFD software platform or conducting experimental testing. Fortunately, as discussed in Section 6.2, reference material was obtainable that allowed for the particulate transport model to be developed using fundamental particulate transport theory such that the five regional concentration values could be determined for both the air permeable and air impermeable PPE sleeve concepts.

3.2. Dosimetric Model

The purpose of the dosimetric model is to determine the dose that is imparted to the forearm in the event of a radiological hazard scenario. To this end, the five regional concentration values obtained from the particulate transport model are used as source terms in the dosimetric model. The dosimetric model is developed using the Monte Carlo N-Particle Transport Code, Version 5 (MCNP, Version 5-1.51, January 2009). As with the particulate transport model, benchmarking experimentation was carried out to ensure that the MCNP5 code could be appropriately applied to simulate real-world radiological processes and was in fact viable for use in this thesis.

A more rigorous discussion of the MCNP5 code is included in Section 5.2.1; however, essentially it is a stochastic code that is able to simulate the nuclear interactions that occur as a given type of radiation passes through a defined environment. In this regard, it is possible to define the type of radiation that is emitted and from where and how often these emissions occur. These parameters are based on the radiation hazard scenario being modelled and the results of the particulate transport model. Figure 14 illustrates where each of the regional concentration values are incorporated as source terms in the dosimetric model.

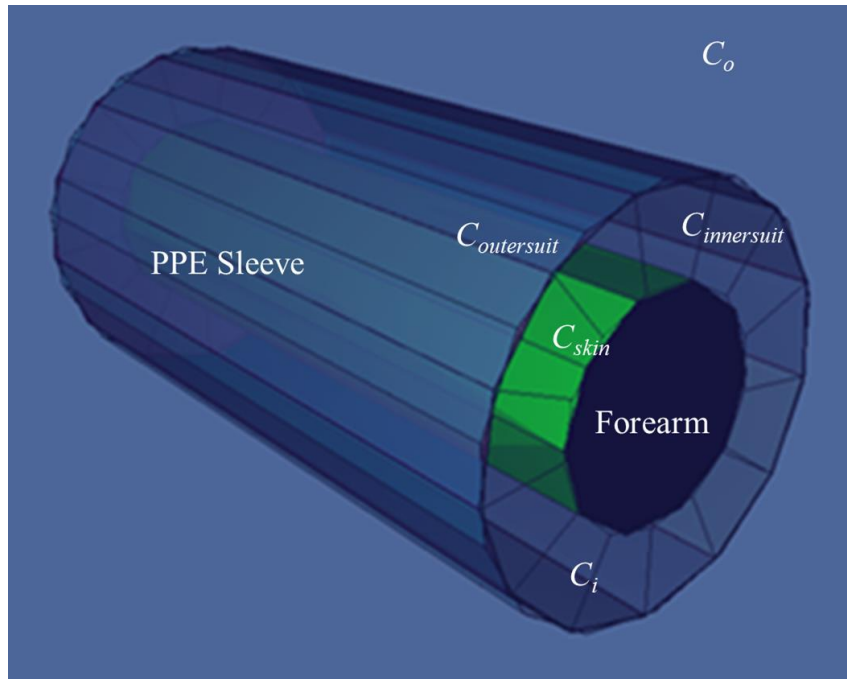


Figure 14: Dosimetric model illustrating the location of the five regional concentration source terms

The next step involves specifying the geometries that make up the environment of interest. For this project, this consists of defining the shape, dimension, composition, and density of the forearm, PPE sleeve, and surrounding air. Based on this information, the MCNP5 code is able to track the emitted radiation from the source as it moves through with the environment and measure the quantity of radiation that is deposited within the forearm volume. In this regard, it is possible to use the code to determine the dose that is imparted to the sleeved forearm as a result of exposure to a radiation hazard scenario. Additionally, the model results will indicate the level of protection provided offered by various PPE suits in different radiological environments as well as enable comparison with the acceptable exposure limits discussed in Section 2.1.5.

4. SCOPE OF PROJECT

As mentioned earlier this project seeks to develop a model that can be employed to determine the dose imparted to an individual, protected by a PPE suit, in the event of radiological exposure. This is a rather ambitious task given the wide-ranging scope of such an investigation; as a result, it was necessary to narrow the scope of the project such that it became more manageable and facilitated proper analysis. As discussed in the previous chapter, it was decided to base the model on the dose imparted to a human forearm in place of a whole-body phantom. The reasoning behind this decision is discussed in Section 4.1; however, emphasis must be placed on the fact that both the particulate transport and dosimetric models are based on this geometry. The dose that is imparted to the forearm is dependent on a variety of exposure conditions, including the type of fabric making up the PPE sleeve, the nature of the radiation hazard, and which radionuclides are present. Given the timeframe of this project, it was not feasible to use the model to analyze how every possible combination of these factors affects exposure. As such, the selection of each of the aforementioned parameters had to be limited, but still reflective of the most likely set of conditions facing military members and first responders. Additionally, as both the particulate transport and dosimetric models are software based, computational limitations were taken into consideration when selecting and defining each of the parameters. The follow sections of this chapter seek to elucidate how and why each of the exposure conditions were selected and explain how they were combined to create a series of different cases. Ultimately, each of these cases was then modelled in order to determine the dose imparted to the forearm as a result of each set of unique radiological conditions.

4.1. Forearm-based Model

Before discussing each of the aforementioned exposure conditions, it is first necessary to explain the reasoning behind selecting a forearm to represent the model geometry as opposed to using a whole-body phantom. Ideally, the selection should consist of a relatively simple geometry so as to limit computing requirements, facilitate benchmarking experimentation, and allow for comparison with the aforementioned acceptable dose limits. In this regard, modelling the dose imparted to a whole-body phantom allows for direct comparison with the recommendations put forth by the ICRP and NATO; however, it is also very computationally intensive on account of its detailed geometry and requires additional experimental resources. Conversely, modelling a single appendage is less computationally intensive and simplifies experimental considerations, but requires the use of approximations to scale the localized imparted dose to a value that is representative of the entire body.

Ultimately, it was decided to model a human forearm, protected by a PPE sleeve, in place of an entire human phantom and full-bodied suit as this significantly simplifies the geometric requirements of the model and, thus, is decidedly less computationally intensive. The decision to base the model geometry off of a human forearm also facilitated benchmarking experimentation. Combined, these benefits outweighed the difficulties associated with having to relate the localized imparted dose to a value that is representative of the whole-body. It is suggested that future models consider whole-body dose, either through changing the model geometry or implementing a set of scaling factors; however, this falls outside of the scope of this project.

4.2. Exposure Conditions

The first exposure parameter that impacts the dose imparted to the forearm is the type of fabric making up the PPE sleeve. Given the limited time frame associated with this work, it was only feasible to include a small number of PPE fabrics for analysis. In this respect, it was important to select fabrics that were representative of the broader categories in which they are classified. Thus, when deciding which types of PPE fabrics to include, the intent was to span fabrics that were either air permeable or air impermeable and that were currently in use by military personnel or first responders. Based on these criteria, both an air permeable fabric and an air impermeable fabric were identified. A generic CBRN fabric, comparable to that of the Horizon 1 CWC suit, was selected to be the representative air permeable fabric due to the fact that it is used in the basic protection suit employed by CAF members in response to radiation hazards [11]. When modelling the air permeable fabric, it was decided to assume that there were no leaks in the PPE sleeve and that particulates could only gain entry to the inner confines of the sleeve by penetrating through the fabric itself. The second generation CRC fabric was chosen to represent air impermeable fabrics as it is the industry standard in radiation protection amongst PPE suits used by first responders and NEWs [14]. Unlike the air permeable fabric, when modelling the air impermeable fabric, it was decided to assume that particulates could not transport across the PPE sleeve but could gain access to the inner confines via closure leaks. It was further decided to include a case in which the forearm was left bare and was not protected by any sort of PPE sleeve during radiological exposure. Using these three cases, it is possible to determine how the presence or absence of a PPE sleeve impacts the dose imparted to the forearm and the level of protection provided by different types of PPE sleeve concepts in a radiological environment.

The next parameter that must be considered is the type of radiation hazard scenario to which the forearm is exposed. NATO has identified four prominent radiological hazard scenarios that pose a significant health threat to military members and first responders [35]. These scenarios are: the deliberate detonation

of an RDD, the loss or improper disposal of a radioisotope source, a tactical nuclear weapons strike, and a nuclear reactor event [35]. Of the four radiation hazard scenarios listed above, dispersion events, nuclear weapons strikes, and nuclear reactor events are all similar in that they result in the release of airborne radioactive particulates into the immediate environment. On a fundamental level, it is not a stretch to see how both nuclear weapon strikes and nuclear reactor events can be represented as large-scale dispersion events, differing predominately according to the radionuclides and relative size distribution of the aerosolized particulates that are released [35]. As such, it was decided to base the modelling cases on the radiation hazard scenario involving the detonation of an RDD; moreover, this is represented in the present work as a dispersion event in which a high concentration of radioactive particulates has been aerosolized and released into the immediate environment near ground level.

Having decided to base the modelling cases on a dispersion event, the final exposure parameter that influences the dose imparted to the forearm is the type of radionuclides that are dispersed as a result of said event. It is possible for a wide variety of radionuclides to be explosively dispersed in the same manner; however, given the time limitations of this project, not all of them could be included in the cases to be modelled. As a result, it was decided to select the radionuclides that are best suited for inclusion in a RDD: Co-60, Sr-90, and Cs-137 [35]. As discussed previously, these radionuclides are used as source materials in teletherapy units, RTGs, and industrial irradiators and, thus, can be acquired in forms that are suitable for inclusion in explosive devices [35]. This made it logical to include three cases to be modelled, one in which the airborne radioactive particulates released during the dispersion event consist of Co-60, one in which the particulates are Sr-90, and one in which the particulates are Cs-137. The selection of these three radionuclides is also beneficial in that they represent a good mix of gamma and beta emitters. With reference to their decay schemes, both gamma and beta radiation are emitted during the decay of Co-60 and Cs-137, whilst only beta radiation is released during the decay of Sr-90 [36,39,40]. In this regard, it is possible to determine the level of protection offered by the selected PPE fabrics against both gamma and beta radiation and determine which has a greater contribution to the total overall dose imparted to the forearm. It was decided to focus the modelling cases on only those radionuclides that emit gamma and beta radiation as these types of radiation constitute much of the external dose threat. Alpha particles and neutrons were each omitted due to the fact that the former have a very short range in air and only pose a significant dose hazard if inhaled or allowed entry into the body via an open wound, whilst the latter are not attenuated by current suit materials [4,13].

4.3. Modelling Cases

Having selected and defined each of the exposure conditions, it is now necessary to outline how they were combined to create each of the individual cases that were modelled. In this regard, all of the modelling cases were based on the dose that was imparted to a human forearm as a result of exposure to a radiological dispersion event. The parameters that changed from case to case were the types of fabric making up the PPE sleeve concept (air permeable, air impermeable, or none) and which radionuclides were aerosolized as a result of the dispersion event (Co-60, Sr-90, or Cs-137). Contingent on the latter was the type of radiation that was emitted by the airborne radioactive particulates. Combining one variable from each of the exposure categories resulted in nine unique cases that were then modelled and analyzed. For example, the first case consisted of determining the dose imparted to the forearm, protected by a sleeve of air impermeable fabric, as a result of exposure to a dispersion event that generated airborne Co-60 particulates. The remaining eight cases are summarized additionally in Table 5.

Table 5: Summary of the nine modelling cases selected for analysis

Case	PPE Sleeve Concept	Radionuclide	Type of Radiation
1	Air impermeable (closure leak)	Co-60	γ, β
2		Sr-90	β
3		Cs-137	γ, β
4	Air permeable (perfectly sealed)	Co-60	γ, β
5		Sr-90	β
6		Cs-137	γ, β
7	None	Co-60	γ, β
8		Sr-90	β
9		Cs-137	γ, β

In summary, the nine cases listed above were selected so as to be representative of the most likely set of conditions facing military members and first responders during a radiological emergency. In this regard, by modelling the nine cases listed above, it was possible to not only determine the dose imparted to the forearm as a result of exposure to each set of conditions, but also to investigate the level of protection offered by various types of PPE fabrics against both gamma and beta radiation and to determine the contribution of each type of radiation to the total overall dose. Whilst the analysis performed by this thesis is limited to select cases, it should be noted that one of the key benefits of the model is that it can be modified and improved in order to expand the analysis to other situations as desired; thus, reducing the amount of experimentation required overall.

5. EXPERIMENTATION

Before the nine cases could be modelled, it was necessary to confirm that the software platforms chosen to develop the particulate transport model and dosimetric model were suitable for inclusion in this project. In this regard, separate particulate transport and transmittance experiments were conducted; however, the purpose of each was to serve as a benchmark against which the appropriate application of the respective software programs could be compared. The intent was to use the software programs to model the benchmarking experiments, taking into consideration the geometry and materials of the experimental set-up and the real-world physical processes being investigated. Recall that the COMSOL Multiphysics (COMSOL) software and Monte Carlo N-Particle Transport Code, Version 5 (MCNP5) were initially selected to develop the particulate transport and dosimetric models. The COMSOL and MCNP5 model results were then compared with those obtained experimentally in order to determine whether each program could be used to accurately simulate real-world physical behaviour and was suitable for use in this project.

5.1. Particulate Transport Benchmarking Experimentation

The purpose of the particulate transport experimentation was to provide a benchmark against which the suitability of the COMSOL software for use in this thesis could be compared and to confirm whether it could be used to simulate accurately the real-world transport phenomena. For this experiment, the outer and inner concentrations of surrogate airborne particulates, using a mechanical ‘*sleeved forearm*’ apparatus, were measured as a function of time. The experimentation was then modelled using COMSOL with the intent being to replicate the experimentally-generated inner concentration values for a given outer concentration and, hence, confirm the suitability of the software for use in final particulate transport model. The following sections will commence with a brief overview of the COMSOL software as a whole before moving on to describe the benchmarking experimentation and corresponding COMSOL model.

The particulate transport benchmarking experimentation was conducted in conjunction with the RMCC CBRN Protection Group. As such, it would be amiss not to acknowledge the valuable assistance provided by T. Mengistu and L. Tremblay with regards to setting up and conducting each experiment and C. McEwen during the design and construction of the mechanical ‘*sleeved forearm*’ apparatus.

5.1.1. COMSOL Multiphysics software

As mentioned above, the COMSOL Multiphysics software was used to model the particulate transport benchmarking experimentation in an attempt to replicate the experimentally-obtained results. The primary benefit of the COMSOL software is that it allows users to extend conventional models, based on one type of physics, into multiphysics models that can simultaneously solve coupled physics behaviour [41]. The software has a number of built in modules that are pre-programed with the partial differential equations describing a wide range of scientific and engineering phenomena, such as acoustics, chemical species transport, electrochemistry, fluid flow, and heat transfer [41]. In this regard, the first step in developing a COMSOL model is to select the module or series of modules that best define the physical phenomenon of interest. Having done so, it is then possible to define the type of study to be conducted. The software is equipped to handle stationary or transient studies, linear or nonlinear studies, and eigenfrequency studies [41].

Based on the physics modules and type of study selected, the COMSOL software automatically compiles the relevant theoretical equations needed to describe the physics model [41]. Thus, it is possible to model complex real-world environments by defining the physical quantities acting throughout the model geometry without having to supply the underlying equations [41]. The software further facilitates this process by including a built-in material property database and the ability to apply different loads, constraints, and sources directly to the various components of the model geometry. Before solving the model, it is necessary to mesh the model geometry such that system of equations can be solved at each node point. Again, the software assists in this process by enabling the user to select from numerous default mesh settings or manipulate the size, shape, and biasing of the mesh as desired [41]. When solving the models, COMSOL assembles and solves the previously compiled system of equations using a variety of different advanced numerical analysis techniques; however, the principal finite element discretization method used by the software is the Galerkin method [41]. Finally, the software can make use of multiprocessor computers and cluster systems to speed up the solution times for complex, coupled models [41].

The intent of the above text was to provide a brief introduction to the COMSOL software. A more detailed discussion of how it was applied to model the particulate transport benchmarking experimentation is presented in Section 5.1.4 and Appendix A, where the selection of the physics modules, model geometry, material, meshing techniques, and solution method are described in depth.

5.1.2. Experimental objective

The objective of the particulate transport experimentation was to measure the inner and outer concentrations of a surrogate particulate species of varying aerodynamic diameter, relative to a mechanical '*sleeved forearm*' apparatus, as a function of time. All aspects of the experimentation were then recreated using the COMSOL software, such that the resulting model could be benchmarked against the experimentally-obtained concentration data. In this manner, it was possible to determine the suitability of the COMSOL software for use in this project.

5.1.3. Experimental methodology

Before it was possible to begin the particulate transport experimentation, it was first necessary to design an apparatus that would be representative of a forearm protected by a PPE sleeve and allow for inner and outer concentration measurements to be taken. It was decided to base the apparatus on an air impermeable fabric with an improperly sealed closure as this greatly simplified both the design and experimental parameters relative to an air permeable fabric. With this in mind, the mechanical '*sleeved forearm*' apparatus was designed as a solid aluminum rod surrounded by an aluminum cylinder. A computer aided design (CAD) representation of the apparatus is presented in Figure 15. The aluminum rod represented the forearm, whilst the aluminum cylinder simulated an air impermeable fabric. The use of an aluminum cylinder to simulate an air impermeable fabric was consistent in that it ensured that no external particulates could gain entry to the inner volume of the apparatus via this boundary. Additionally, the use of aluminum improved the durability of the apparatus and facilitated its use in multiple experiments in the sense that it could simply be wiped clean as opposed to having to reattach a new piece of fabric for each trial. The resulting inner volume was separated into six channels orientated in the axial direction and was bounded by an end cap and sampling port. The end cap was designed with slots that could be remotely opened or closed to allow or deny the external particulates access to the inner volume of the cylinder. This was intended to simulate a leak or improperly sealed closure at the cuff of the PPE sleeve. The sampling ports were located at the opposite end of the mechanical '*sleeved forearm*' apparatus and allowed for the inner concentration of airborne particulates far from the closure to be measured.



Figure 15: Mechanical 'sleeved forearm' apparatus used in the particulate transport benchmarking experimentation

Although outside the scope of this experimentation, the apparatus design further enabled both the inner 'sleeve' and 'forearm' surface concentrations and outer 'sleeve' surface concentration to be determined via swabbing of the aluminum cylinder and rod, respectively. Additionally, as designed, the apparatus was equipped for sampling from a single channel of the inner volume; however, this was not performed as part of the particulate transport benchmarking experimentation.

Prior to commencing each experiment, the end cap slots were closed and the apparatus was sealed using a combination of paraffin wax film and silicon-based stopcock grease. The inner volume was then evacuated to ensure that there was a zero concentration of particulates within the apparatus, before it was placed horizontally on a stand in a large box that was then filled with surrogate particulates to simulate the conditions of a dispersion event. For health and safety reasons, actual radioactive particulates could not be used for the experiments; as such, surrogate particulates of a similar size range, formed using sodium chloride condensation nuclei combined with di-2-ethyl hexyl sebacate as the aerosol material, were used instead [42]. The surrogate particulates were pumped into the

confines of the box using a condensation monodisperse aerosol generator (TSI Particle Instruments, Model 3475). The use of this type of generator was significant in that it allowed for a high level of monodispersity to be achieved, even at high particulate number concentrations [42]. In this regard, it was possible to control the number of particulates being generated, as well as to specify the aerodynamic diameter of said particulates and focus their distribution about a mean value as desired. Miniature cooling fans were used to ensure a uniform distribution of particulates throughout the box. An aerodynamic particle sizer (APS) spectrometer (TSI Particle Instruments, Model 3321) was used to measure and record the concentration of surrogate particulates inside and outside of the ‘*sleeved forearm*’ apparatus. One of the primary benefits to using the APS was that it was able to measure and bin particulates ranging in aerodynamic diameter from 0.5 – 20 μm to a resolution of 0.02 μm [43]. In this manner, concentration data was collected for the particulates that were recorded within the size bins ranging from 0.835 – 0.898 μm , 0.965 – 1.037 μm , and 1.114 – 1.197 μm . For ease of discussion, each of these particulate size ranges has been designated as a unique letter listed in Table 6. An additional benefit of the APS was that it could be set to take a sample measurement for a given time increment as desired [43].

Table 6: Particulate size designations and corresponding size range

Particulate Size	Size Range / μm
A	0.835 – 0.898
B	0.965 – 1.037
C	1.114 – 1.197

Three experimental trials were completed at each particulate size to ensure the reproducibility of the results. Due to the sensitive nature of the condensation monodisperse aerosol generator, it was difficult to ensure that the overall outer concentration of particulates and mean particulate diameter were constant prior to commencing each of the three trials. As a result, the initial outer concentration of each particulate size varied slightly for each trial. The initial conditions for the three particulate transport experimental trials are presented in Table 7.

Table 7: Summary of initial conditions for the particulate transport experimentation

Trial	Overall Mean Particulate Diameter / μm	Outer Concentration ($\pm 5\%$) / particle cm^{-3}			
		Overall	Size A	Size B	Size C
1	1.02 ± 0.02	419	30	87	62
2	1.04 ± 0.02	425	30	85	63
3	1.02 ± 0.02	430	36	92	58

To begin each experimental trial, the number concentration of particulates in the outer volume of the box ($C_o(t)$) was measured on 5 s intervals over a period of 120 s, for each particulate size, using the APS spectrometer.

Following this period, the APS was attached to the sampling port on the mechanical ‘*sleeved forearm*’ apparatus and the end cap slots were turned to the open position. This allowed the particulates in the outer volume to begin to enter the apparatus, influenced by the draw of the sampling pump of the APS. The APS was then used to measure the inner concentration of particulates ($C_i(t)$) at the outlet of the apparatus, for each particulate size, on 5 s intervals over a period of 360 s.

To complete the experiment, the APS spectrometer was removed from the sampling port and, again, used to measure the outer concentration of particulates on 5 s intervals over a period of 120 s. As only a single APS was available, it was necessary to measure the outer concentration of particulates both before and after recording the inner concentration to permit interpolation of the outer concentration for the period of time that the inner concentration measurement was taking place. It should be noted that a Y-junction tube was used to reduce the sampling flowrate of the APS from its predefined value of $1.0 \pm 0.2 \text{ L min}^{-1}$ to $0.16 \pm 0.01 \text{ L min}^{-1}$ by attaching a filter to one side of the Y-junction and sampling the air within the apparatus on the other [43]. This reduction yielded a flow rate more characteristic of convection within a PPE sleeve and allowed for better resolution of the concentration measurements recorded by the APS given its aforementioned sampling interval of 5 s.

5.1.4. COMSOL modelling

In order to benchmark a COMSOL model against the particulate transport experimentation, it was first necessary to replicate the experimental set-up. In this regard, the model geometry was constructed so as to accurately reflect the dimensions of the mechanical ‘*sleeved forearm*’ apparatus. A 2D axisymmetric model was constructed in which the model geometry was revolved about the axial axis to simulate the cylindrical apparatus design. The materials making up the model also mimicked those of the experiment, namely that the apparatus was composed of aluminum and air was the fluid passing through it. The most important aspect of developing the model was selecting the physics modules required to simulate the observed phenomena. In this regard, the rate of change of the inner concentration of particulates was best described using Fick’s second law of diffusion; moreover, given the magnitude of sampling flowrate of the APS, it was evident that the convective term would heavily influence the solution. As a result, it was decided to couple the ‘*Transport of Diluted Species*’ and ‘*Laminar Flow*’ modules to make use of the software’s built-in equations describing chemical species transport and fluid flow mechanics. By coupling the two, it was

possible to first use the ‘*Laminar Flow*’ module to solve for the velocity of the air as it passed through the apparatus and then include this value in the convective term of Fick’s second law, which was subsequently solved using the ‘*Transport of Dilute Species*’ module. The decision to model the fluid flow conditions as being laminar rather than turbulent was supported by determining the Reynolds number for the flow of air through a horizontal concentric annulus with dimensions equivalent to that of the ‘*sleeved forearm*’ apparatus [17]. Using Equation 11, the Reynolds number was calculated to be 2.4, confirming that the fluid flow conditions produced during the particulate transport experimentation were in the laminar regime ($Re < 2000$) [17].

Having selected the physics modules to include in the model, it was then necessary to define a number of key variables pertaining to each. For the ‘*Laminar Flow*’ module, the condition of incompressible flow was assumed and the inlet velocity profile was set so as to be consistent with the sampling flowrate of the APS and inlet dimensions. Additionally, the fluid properties, such as density, dynamic viscosity, and diffusion coefficient, were set so as to be a function of the material, in this case air, under standard ambient conditions of temperature and pressure. For the ‘*Transport of Dilute Species*’ module, the initial inner volume concentration was said to be zero, whilst the velocity field within the apparatus was coupled to the ‘*Laminar Flow*’ module. Finally, the initial outer volume concentration was designated as a function of time based on the data obtained during the experimentation for each particulate size. In order to facilitate the modelling of multiple experiments involving particulates of different mean diameter, the upper bound of each particulate size was defined as a global modelling parameter. Doing so meant that any time this parameter was changed, the variables dependent on particulate size were automatically updated throughout the model.

The model geometry was meshed using a combination of quadrilateral and triangular shapes. The size of the mesh elements varied with location; however, the aim was to limit computational requirements whilst still enabling the smaller features of the model geometry to be resolved. A transient study was used to determine the inner volume concentration and velocity profiles as a function of time. The range was set such that solutions were obtained on 1 s intervals for a period of 360 s and, thus, enabled comparison with the experimentally-obtained results. To solve the compiled system of equations representing both the particulate transport and fluid flow, a fully coupled solution approach, employing a parallel sparse direct solver (PARDISO) with a backward differentiation formula (BDF) time stepping method, was used. For varying aerodynamic particulate diameters, the COMSOL modelling results were compared with the inner particulate concentration data obtained experimentally in order to assess the validity of the software and its use in this project. For additional detail regarding the COMSOL

model geometry dimensions, input parameters, meshing technique, or solution method, please reference Appendix A.

5.1.5. Experimental results and discussion

The particulate transport benchmarking experimentation was successfully completed for Size A, B, and C particulates. The experimentally-obtained results for the Size A particulates are presented in Figure 16. The error associated with each individual data point was $\pm 5\%$ and the dashed lines illustrate when the end cap slots were opened and closed. Similar figures for the Size B and Size C particulates are included in Appendix B.

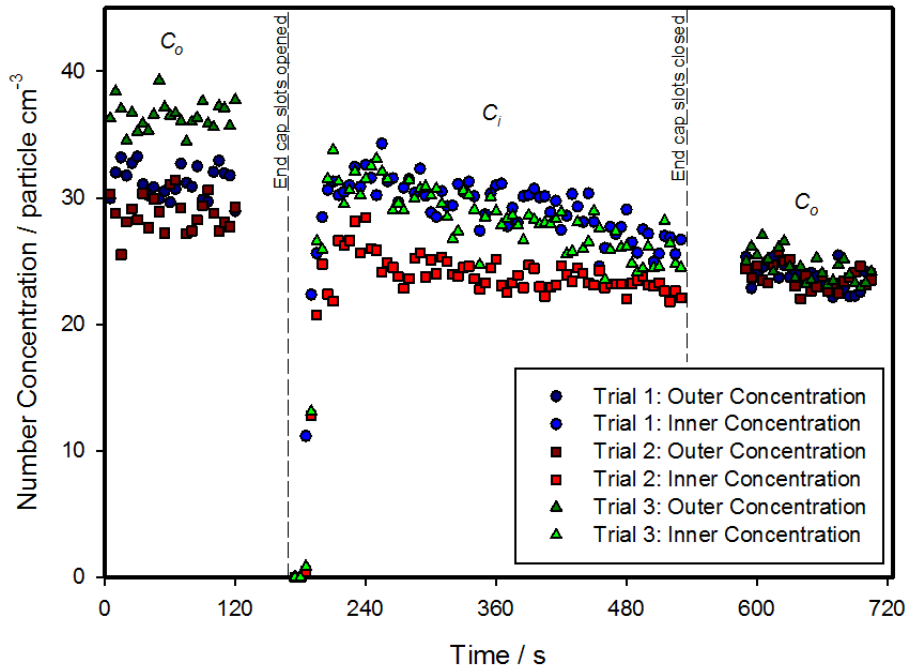


Figure 16: Experimentally-obtained inner and outer concentration results for the Size A particulates

Figure 17, Figure 18, and Figure 19 illustrate the average inner and outer concentration results for each of the three particulate sizes. These plots were obtained by averaging the inner and outer concentration results for each of the three trials and indicate a number of trends. The first trend relates to the amount of time required for the inner concentration to reach equilibrium with the outer

concentration. As the figures illustrate, approximately 15 s after the end slots were opened at 175 s, the APS measured the first particulates at the far end of the apparatus volume; moreover, 45 s after opening, the concentration of particulates within the apparatus was largely comparable to that of the interpolated outer concentration.

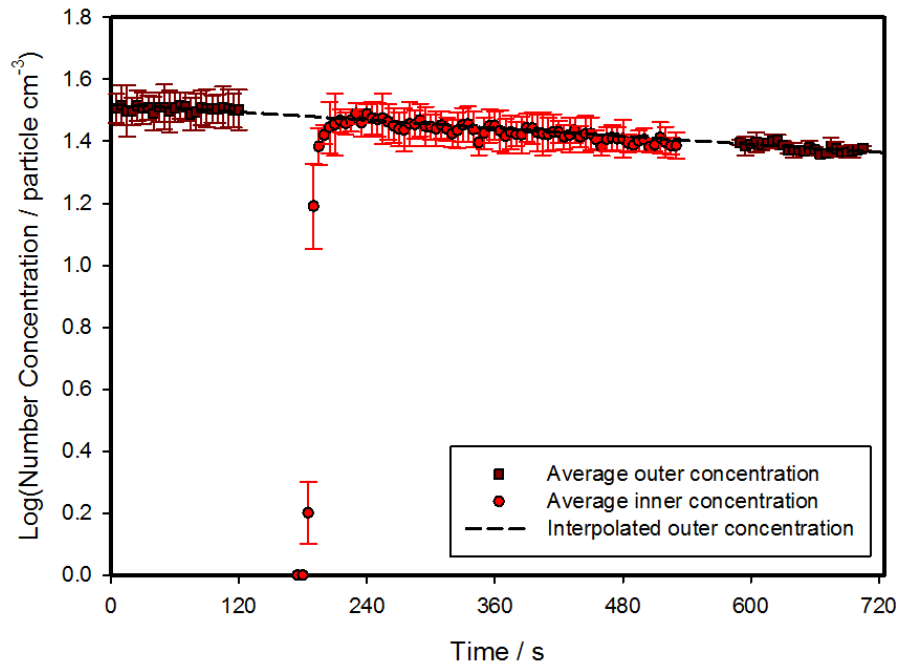


Figure 17: Experimentally-obtained average inner and outer concentration results for the Size A particulates

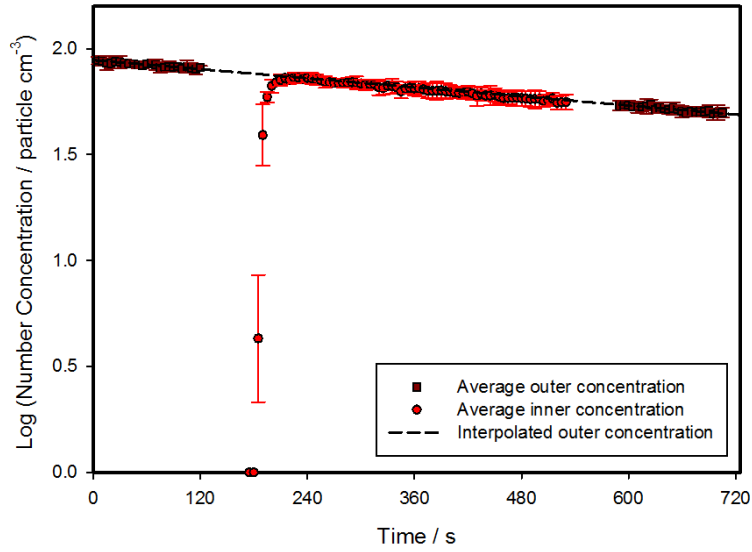


Figure 18: Experimentally-obtained average inner and outer concentration results for the Size B particulates

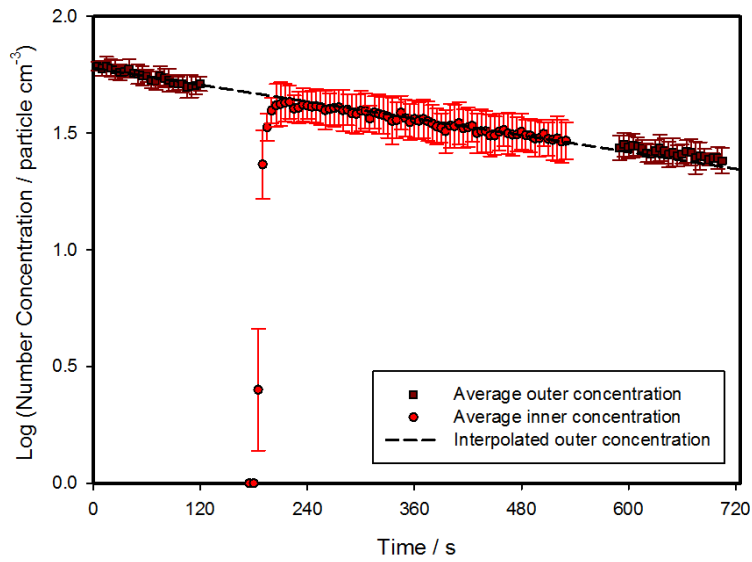


Figure 19: Experimentally-obtained average inner and outer concentration results for the Size C particulates

The reason that a general decrease in the average outer concentration was observed for each particulate size is due to the fact that a fixed number of particulates were initially pumped into the box before the APS was turned on to begin each experiment. Thus, due to the aerosol sampling flowrate of the APS and general deposition effects, the concentration of particulates within the box decreased with time. That being said, it is interesting to note that the rate at which this decrease occurred varied as a function of the particulate sizes. Because the aerosol sampling flowrate was kept constant for each of the experiments, the discrepancies could stem from differences in deposition velocity and gravitational settling for each of the particulate size ranges. In this regard, as evidenced by Table 4 and Equation 13, theory would predict that the larger particulates would have a higher deposition velocity and be more susceptible to the effects of gravitational settling than smaller particulates [21]. This was supported by the experimental results presented in Table 8, as it is evident that the outer concentration of the Size C particulates decreased more rapidly when compared with that of the Size A or Size B particulates; moreover, the rate of decrease of the outer concentration of the Size B particulates was greater than that of the Size A particulates. A two-tailed t-test, for a 95 % confidence limit, confirmed that the rate of decrease of the outer concentration of the Size C particulates relative to that of the Size B particulates was statistically significant. Similar findings were obtained when comparing the rate of decrease of the outer concentration of the Size B particulates with that of the Class A particulates. The calculations are included in Appendix C.

Table 8: Rate of decrease of the outer concentration for each of the three particulate sizes

Particulate Size	Size Range / μm	Log[Rate of Decrease of Outer Concentration / (particle cm^{-3}) s^{-1}]
A	0.835 – 0.898	$(2.17 \pm 0.05) \times 10^{-4}$
B	0.965 – 1.037	$(3.57 \pm 0.02) \times 10^{-4}$
C	1.114 – 1.197	$(5.57 \pm 0.05) \times 10^{-4}$

5.1.6. COMSOL model benchmarking

The results of the COMSOL model were compared against the averaged experimentally-obtained inner concentration data for each of the three particulate sizes. In each case, as presented in Figure 20, the COMSOL model was unable to successfully replicate the experimental results of the particulate transport benchmarking experimentation. For each of the three particulate sizes, the COMSOL model correctly predicted the general trend of the inner particulate concentration profile; however, a major time shift was observed when attempting to compare the modelling results with the experimental data. The model predicted that a longer period of time would elapse before the first particulates were measured by the APS and, subsequently, before the inner concentration reached

equilibrium with the outer concentration, compared with what was determined through experimentation. This would seem to indicate that the velocity of the particulates moving through the inner volume of the apparatus was slower in the model than in the experimentation or that there was a leak in the end cap seal that allowed the particulates to gain entry to the inner confines of the apparatus prior to the start of the experimentation. The latter seems unlikely as the APS was run for a minimum time of 120 s to ensure that the inner concentration of particulates was zero at the onset of each trial.

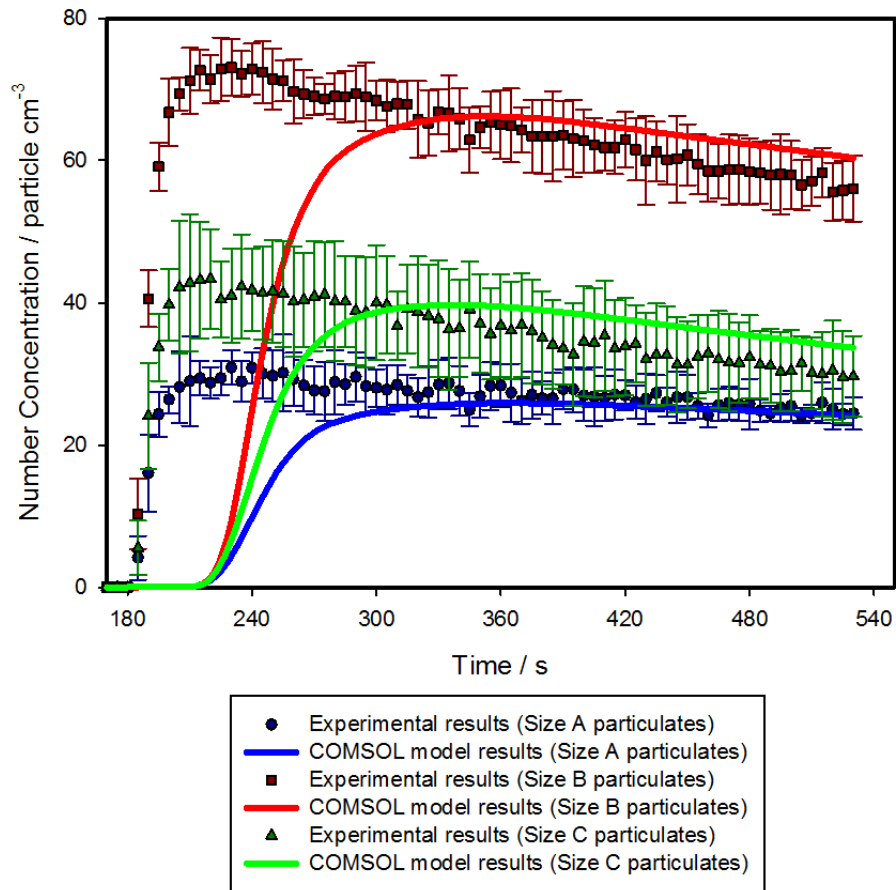


Figure 20: Comparison of the average experimental and COMSOL model inner concentration results for each particulate size

In an attempt to rectify this discrepancy, it was possible to compare the sleeve velocity profile within the '*sleeved forearm*' apparatus generated by the COMSOL model with that predicted by theory based on the experimental conditions. As illustrated in Figure 21, the sleeved velocity profile of the air (white arrows), generated by the COMSOL model, is highest furthest from the walls and decreases to zero, in accordance with the applied no slip condition along the wall boundaries. To account for this and allow for comparison with the sleeve velocity observed experimentally, the magnitude of the velocity gradient throughout the sleeve was averaged using a built-in function of the software. The average sleeve velocity produced by the COMSOL model was 0.00341 m s^{-1} , whereas, for the measured experimental flowrate and apparatus dimensions, theory predicts a value of $0.0035 \pm 0.0002 \text{ m s}^{-1}$. The fact that the COMSOL model accurately predicted the average sleeve velocity and yet still lagged behind the experimental results indicates that there may have been additional phenomena taking place during the experimentation that was not accounted for in the model. One neglected factor was the likely existence of flow-streams in the air outside the apparatus. This would have served to increase the velocity of the particulates, which would have already been moving as they reached the inlet of the apparatus, offering one explanation as to why the modelling results lag behind those obtained experimentally. Additionally, the decision to base the velocity profile of the particulates within the apparatus on the incompressible, laminar flow of air may not have been representative of the actual physical particulate transport phenomena taking place experimentally. In this regard, employing an alternative approach to describing the convective transport of the particulates may result in a model that yields better results and is worthy of study in a future work.

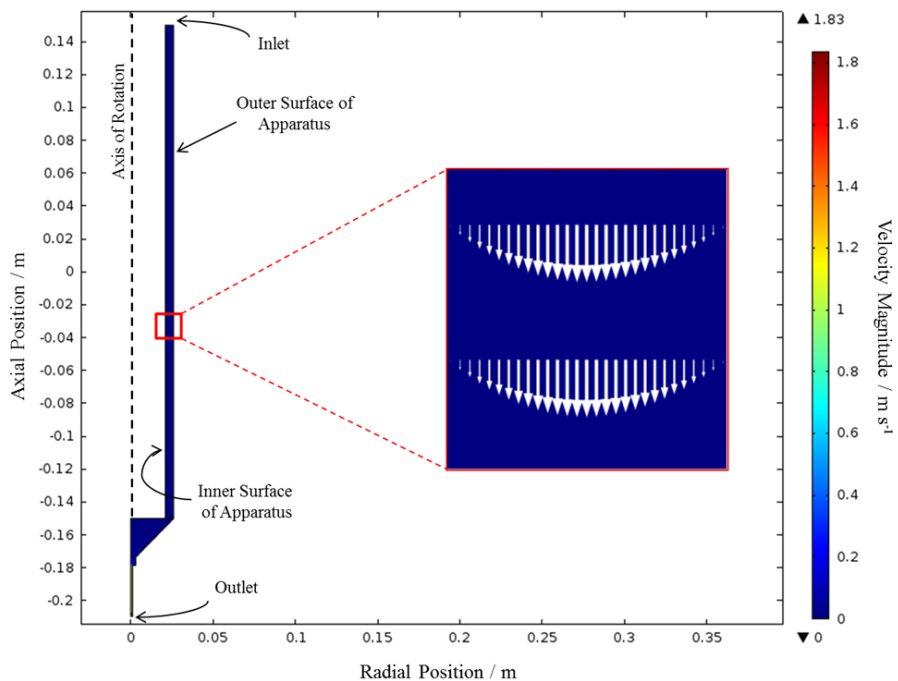


Figure 21: COMSOL model results of the velocity profile of the air flowing through the experimental apparatus

Figure 22 has been included to demonstrate the fit between an adjusted COMSOL model and the experimental data for the Size B particulates. For the adjusted COMSOL model, the flowrate measured during the experimentation was ignored and the inlet velocity was increased from a value of 0.00352 m s^{-1} to 0.015 m s^{-1} , so as to eliminate the time shift. Figure 22 illustrates that the adjusted COMSOL model is fully consistent with the experimentally-obtained results for the Size B particulates. Similar behaviour is also observed for the Size A and C particulates. These results strongly indicate that including a mechanism within the model to account for the flow-streams outside of the apparatus inlet may produce a more realistic velocity profile and eliminate the time shift discrepancy. Without the author gaining further expertise with the COMSOL software or critically assessing other finite element software packages, the addition of these complexities are beyond the time restraints of this thesis. As discussed in Chapter 8, the development of a more robust finite element particulate transport model could be considered for a future thesis topic.

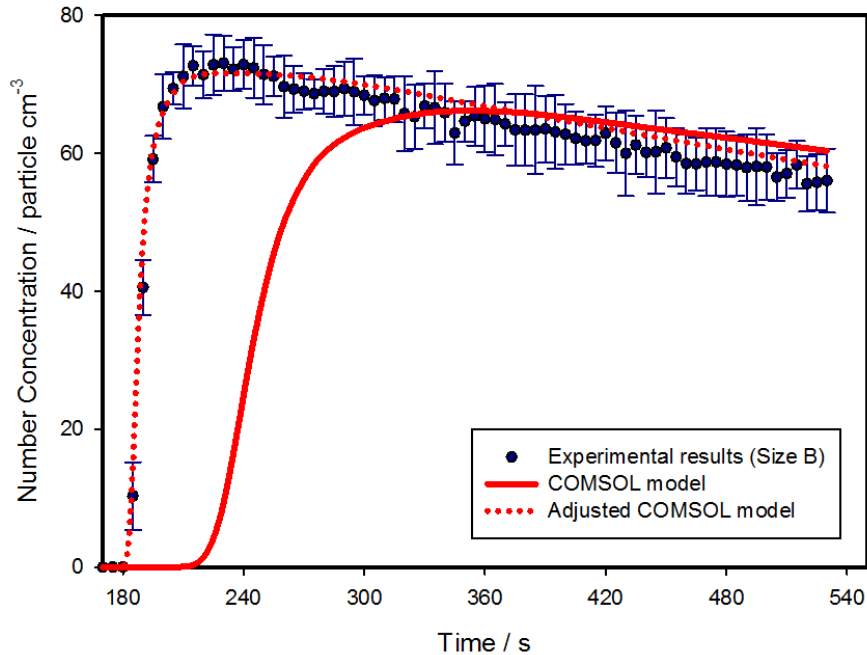


Figure 22: Comparison of the average experimental and adjusted COMSOL model inner concentration results for the Size B particulates

5.1.7. Summary of particulate transport experimentation and COMSOL modelling

The COMSOL model was not successfully benchmarked against the results of the particulate transport experimentation. As such, it can be concluded that the COMSOL software, with the current module selection, is not suitable for use in the remainder of this project. It is recommended that additional finite element particle transport modelling be attempted as part of a future work, using either the COMSOL software with a different module or an alternative CFD platform better equipped to simulate particulate transport phenomenon. These recommendations are discussed in greater detail as part of Chapter 8. As the first approach to developing and solving the particulate transport model was deemed to be unviable, a theoretical approach, incorporating data from the literature, will be used for the remainder of this project to construct the model such that the five regional concentration values can be determined for each of the nine modelling cases. This approach is presented in Section 6.2.

As a result of the observed discrepancies, it was not possible to use the inner and outer concentration data collected during the particulate transport experimentation in the first principles model. The reason for this is that the experimental conditions and ‘*sleeved forearm*’ apparatus were designed for the sole purpose of providing a reference against which the COMSOL model could be benchmarked and the experimental conditions used were not characteristic of an actual exposure scenario. In this regard, the experimentation was limited in a number of ways. Firstly, the initial outer concentration was much lower than that observed during an actual dispersion scenario [35]. Secondly, the end cap slots were too large to be representative of the standard size of a closure leak or improperly sealed wrist cuff. Additionally, because the apparatus was constructed out of aluminum, data allowing for the determination of skin and cloth deposition velocities for each of the three particulate sizes could not be obtained. Finally, the sampling flowrate of the APS ensured that the motion of the particulates was relatively uniform and unidirectional, moving solely from the inlet to the outlet of the ‘*sleeved forearm*’ apparatus. In reality, the motion of the individual wearing the PPE suit would contribute to a greater mixing of the particulates within the confines of the suit and they would be able to exit as well as enter through any leak or improperly sealed closure [17].

5.2. Transmittance Benchmarking Experimentation

The purpose of the transmittance experimentation was to provide a benchmark against which the suitability of the MCNP5 code for use in this project and its ability to simulate real-world radiological phenomena could be compared. The experimentation was completed as part of a separate paper, entitled ‘*Analysis and Monte Carlo modelling of radio-opaque personal protective fabrics*’, which has been published in the Journal of Radioanalytical and Nuclear Chemistry and was first authored by the author of this thesis [14]. In the interest of brevity, it has been decided to omit the material presented in the publication that falls outside of the scope of this project; moreover, the following sections are intended to provide an overview of the publication while additional emphasis is placed on the portions pertinent to the benchmarking of the MCNP5 code for use in this project. In this regard, a brief introduction to the code is provided before illustrating how it was benchmarked against the transmittance experimentation and experimentally-obtained results. Please reference the journal publication if further detail is required [14].

It must be noted that the transmittance experimentation could not have been completed without the assistance of the RMCC Analytical Science Group (ASG), especially D.G. Kelly, C. McDonald, and P. Samuleev, as well as R.D. Whitehead and J. Snelgrove.

5.2.1. Monte Carlo N-Particle Transport Code, Version 5

MCNP5 was developed by the Los Alamos National Laboratory (LANL) and is the internationally recognized simulation code for analyzing gamma photon, electron, and neutron transport using the Monte Carlo method [44]. It is a stochastic computer code that allows the user to generate detailed replicas of realistic environments; moreover, using a random number generator and physical cross section data, MCNP5 is able to determine the likelihood that a species undergoes a nuclear event while traversing through said geometries [44]. Additionally, the code can be used to simulate the production of different types of secondary radiation, such as the emission of delta rays, Auger electrons, characteristic X-rays, and bremsstrahlung photons, that are produced as a result of interactions between source particles and the environmental geometry [44]. By repeating this for a large number of source particles, MCNP is able to provide the user with the most probable outcome and an associated uncertainty per source particle [44].

A typical MCNP5 input file is broken down into three integral cards: the cell card, the surface card, and the data card [44]. These cards represent different sections of the input file and, together, play an important role in allowing the user to convert the realities of the physical setting that are being modelled into a form that the program can understand and run. The cell card is used to define the location and density of each of the different materials making up the model, whilst the surface card is used to construct the geometric structure of the model [44]. The data card is the most complex of three cards and has two primary functions. The first is to define the radiation source of interest; moreover, information relating to the initial position of the source, its radius, the axis in which it extends, the particle type being emitted from the source, and the energies of these particles can be included [44]. The second function of the data card is to define the type of tally that is being solved for [44]. From a radiation protection standpoint, MCNP5 can be used to calculate a number of different physical quantities, including the particle flux through a surface, the current in or through a surface, or the dose imparted to a given volume [44]. In this manner, by combining the three cards it is possible to use the MCNP5 code to solve for many different values as a result of a wide range of radiological conditions.

A detailed description of the contents of each card for the final MCNP5 dosimetric model is included in Section 6.3. It was deemed redundant to include a likewise in-depth explanation for the benchmarking transmittance experimentation model; however, the following sections will briefly outline the various aspects of the code pertinent to reproducing the experimental set-up and experimentally-obtained results. The actual MCNP5 input file used to simulate the transmittance experimentation has been annotated and included for reference in Appendix D.

5.2.2. Experimental objectives

The objective of the publication was multi-faceted and, in this sense, also allowed for the simultaneous benchmarking of an MCNP5 model against experimentally-obtained results. The primary objective of the work was to characterize the composition of a second generation CRC fabric and analyze its gamma photon attenuation capabilities. A prior publication by Corcoran *et al.* performed a similar analysis on a variety of different PPE materials, including a first generation CRC fabric [13]. The first generation CRC fabric is an earlier model of the second generation CRC fabric, manufactured in the same manner but differing in terms of thickness, elemental composition, and density [13, 14]. As such, these data were used as basis against which the experimentally-obtained characterization and attenuation results for the second generation fabric could be compared. The second objective was to illustrate that a Monte Carlo-based computational model could be used to assist in the design and optimization of new CRC fabrics without incurring expensive manufacturing and testing costs. In order to complete this, it was first necessary to illustrate that the MCNP5 software could be properly used to create a model capable of simulating real-world, radiological processes. As such, an MCNP5 model was benchmarked against the experimental results obtained during second generation CRC fabric transmittance experimentation.

5.2.3. Experimental methodology

5.2.3.1. Fabric characterization

A variety of different analytical techniques was used to characterize the second generation CRC fabric. Scanning electron microscopy (SEM) was performed in order to generate high-resolution images of each of the various layers making up the fabric, whilst Fourier transform infrared (FTIR) spectroscopy was employed to assist in identifying the respective types of material composing each layer. Energy-dispersive X-ray (EDX) spectroscopy was then used to obtain a qualitative measurement of the elemental composition of each layer. This measurement was quantifiably supported using a combination of inductively coupled plasma-mass spectrometry (ICP-MS) and instrumental neutron activation analysis (INAA). Finally, the thickness and density of the second generation CRC fabric were measured and determined experimentally. For additional information regarding the procedures followed or apparatuses involved in each characterization analysis, please reference the published paper [14].

5.2.3.2. Transmittance of gamma photons

A transmittance experiment was set up to analyze the gamma photon attenuation capabilities of a second generation CRC fabric. In order to do so, the reduction in transmittance of a multi-radionuclide challenge source by a single layer of the second generation CRC fabric and a fabric-free reference was tested using one hour exposures with real-time gamma photon detection. Additionally, trials were conducted to determine the reduction in transmittance for multiple (2, 4, 6, 8, 10, and 20) fabric layers. A NIST-traceable multi-radionuclide challenge source, emitting gamma photons ranging from 50-1850 keV, was used for each of the trials, while a high-purity germanium detector and multi-channel analyzer, shielded by a lead castle, were used to measure and bin the incident photons in both the presence and absence of the second generation CRC fabric. Additional software was then used to analyze the experimentally-obtained spectra. A custom-designed acrylic holder was used to immobilize the challenge source and ensure it maintained a constant distance from the detector during each of the trials.

5.2.4. MCNP5 modelling

In order to benchmark a MCNP5 model against the transmittance experimentation, it was first necessary to model the geometry of the experimental set-up to a high degree of accuracy. In this regard, the design specifications for the high purity germanium detector were referenced from the manufacturer; moreover, this included information pertaining to the dimensions, density, and elemental composition of each of the components making up the detector. Additionally, detailed geometric measurements of the acrylic holder, protective lead castle, and multi-radionuclide challenge source were made, whilst the certificate of calibration, provided with the challenge source, was referenced to ensure the source activities included in the model were consistent with those of the experimentation. Finally, the elemental composition, thickness, and density of the second generation CRC fabric were modelled based on the results of the various characterization tests.

Once the experimental geometry had been modelled successfully, a pulse height or f8 tally was employed to count the number of pulses within the detector volume in the presence and absence of the second generation CRC fabric. Discrete energy bins were included in the model such that the energy of the incident gamma photons could be determined; moreover, this enabled the transmittance of a single layer of the fabric to be calculated at each of the energies corresponding to the radionuclides of the challenge source. For the second generation CRC fabrics, the MCNP5 modelling results were compared with the experimentally-obtained gamma photon transmittance results to assess the validity of the software for further use in this project.

5.2.5. Experimental results and discussion

It has been decided to only present a discussion of the results that are pertinent to the benchmarking of the dosimetric model. For the additional material presented in the published work, please see Reference 14.

5.2.5.1. Fabric characterization

The thickness of the second generation CRC fabric was determined to be 0.79 ± 0.02 mm, whilst its density was calculated to be 2.4 ± 0.2 g cm⁻³ [14]. As shown in Figure 23, the results of the SEM imaging indicate that there are three distinct layers making up the fabric [14]. EDX spectroscopy further indicates that the middle layer contains elevated concentrations of the radio-opaque metals bismuth and, to a lesser extent, tungsten. The addition of bismuth differentiates the second generation CRC fabric from its first generation predecessor, which has been shown to rely solely on tungsten additives by Corcoran *et al.* [13, 14]. Table 9 presents the elemental concentrations of the first and second generation CRC fabrics as determined by ICP-MS and INAA. The results quantitatively support the results of the EDX spectroscopy analysis, specifically that the main difference between the first and second generation fabrics is the inclusion of bismuth in the latter. In both fabrics, the characterization analyses identified the presence of a variety of secondary metals that are likely the result of impurities in the commercial bismuth or tungsten sources [14].

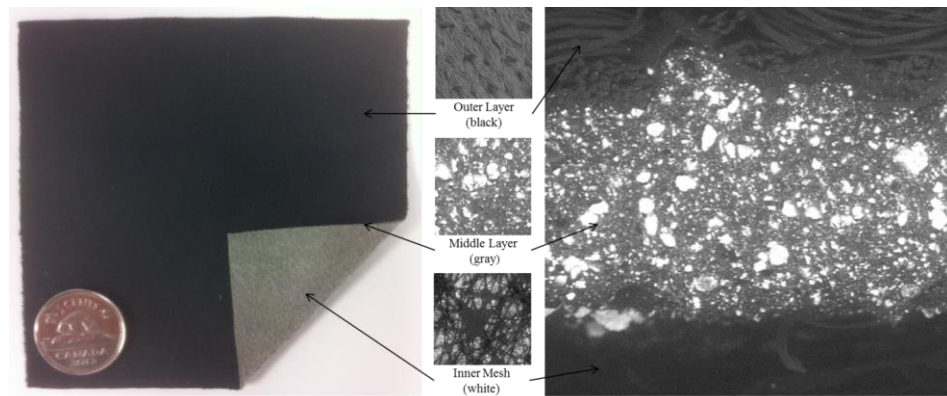


Figure 23: Photograph and SEM images (100× magnification, using 20.0 keV electrons at 1 mbar) of the second generation CRC fabric [14]

Table 9: ICP-MS and INAA(*) results for the first and second generation CRC fabrics [14]

Element	Symbol	First Generation CRC Fabric Concentration [13] / $\mu\text{g}\cdot\text{g}^{-1}$	Second Generation CRC Fabric Concentration / $\mu\text{g}\cdot\text{g}^{-1}$
Bismuth	Bi	-	580000 ± 2000
Tungsten	W	$326000 \pm 1000^*$	$160000 \pm 600^*$
Calcium	Ca	-	1100 ± 45
Iron	Fe	$9000 \pm 400^*$	930 ± 40
Nickel	Ni	-	800 ± 20
Cobalt	Co	$2238 \pm 3^*$	460 ± 10
Sodium	Na	-	280 ± 11
Chromium	Cr	$3190 \pm 9^*$	220 ± 4
Aluminum	Al	-	150 ± 3
Potassium	K	-	46 ± 2
Copper	Cu	-	35 ± 1
Manganese	Mn	-	15 ± 1
Zinc	Zn	-	4.3 ± 0.4
Antimony	Sb	$18.7 \pm 0.3^*$	< 0.25
Tantalum	Ta	$86.0 \pm 0.1^*$	-
Lanthanum	La	$1.0 \pm 0.3^*$	-

5.2.5.2. Transmittance of gamma photons

Gamma photon transmittance is most commonly defined as presented in Equation 26.

$$T = \frac{I}{I_o} \quad (26)$$

where T denotes transmittance, I_o represents the intensity of the mono-energetic photons that impact the detector surface, and I is the intensity of the gamma photons that pass through the CRC fabrics and contact the detector [4]. Single layer transmittance results for both the first and second generation CRC fabrics are presented in Figure 24. Comparing the two, it is evident that the second generation fabric shows a decreased transmittance compared to the first generation fabric at lower photon energies, namely in the 50-300 keV region. For higher energy gamma photons, 300-1850 keV, statistically significant reductions in transmittance are not observed for either of the CRC fabrics.

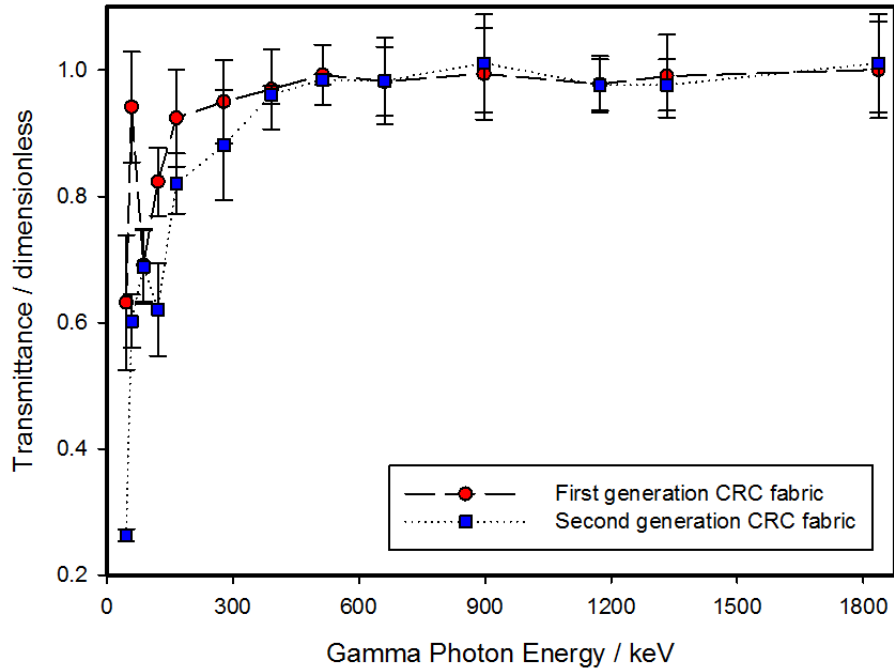


Figure 24: Experimentally-obtained transmittance results for a single layer of the first and second generation CRC fabrics as a function of gamma photon energy [14]

5.2.5.3. MCNP5 model benchmarking

The MCNP5 software was successfully used to model the gamma photon transmittance experimentation carried out for a single layer of the second generation CRC fabric. As illustrated in Figure 25, with the exception of the range of photon energies between 50-80 keV, the experimental and MCNP5 transmittance results closely align for the range of gamma photon energies tested. Experimentally, the region of discrepancy corresponds to a single experimental datum at 59.5 keV; moreover, it is plain that the MCNP5 model drastically over-predicts the observed experimental transmittance at this energy.

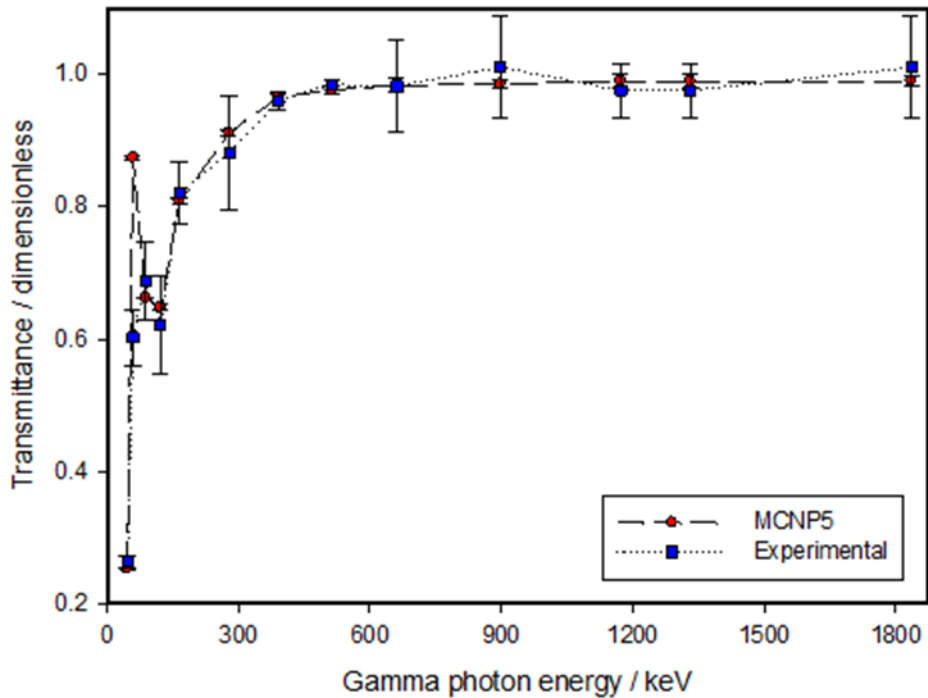


Figure 25: Comparison of experimental and MCNP5 transmittance results for a single layer of the second generation CRC fabric as a function of gamma photon energy [14]

In order to explain this discrepancy, it was necessary to gain more information regarding the energies of the gamma photons incident on the detector, both experimentally and in the MCNP5 model. As such, a refined MCNP5 model was developed in which the energy bins used to catalogue the incident gamma photons were reduced to 0.1 keV widths. The results presented in Figure 26 indicate that, within the region of discrepancy, the majority of the photons incident on the detector possess energies of either 58.2 keV or 59.5 keV. The former is characteristic of the energy of the secondary X-rays released due to transitions between the L- and K- electron orbital shells in tungsten [45], whilst the later corresponds to the photons that are emitted by the Americium-241 (Am-241) isotope in the multi-radionuclide challenge source.

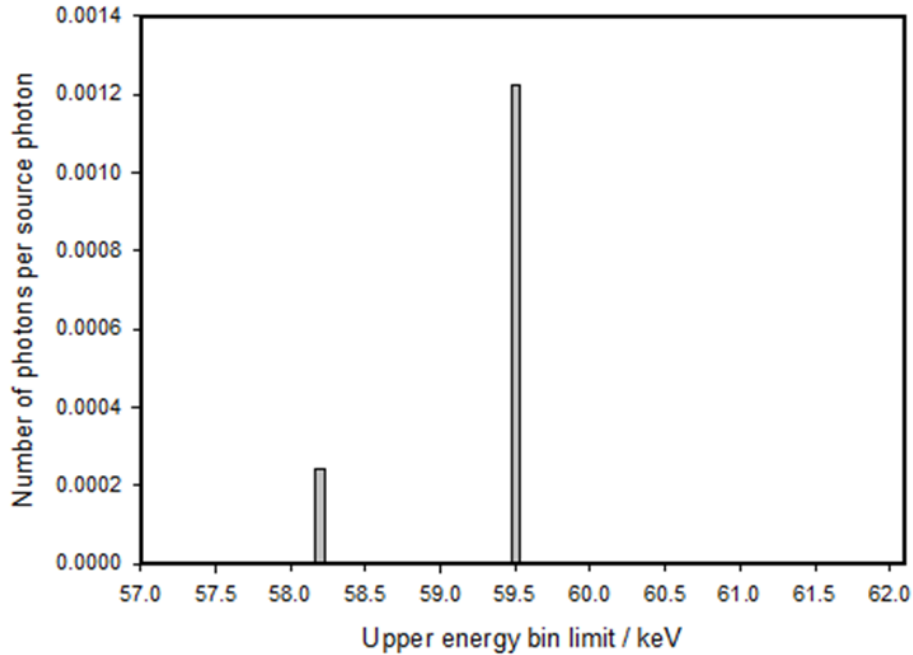


Figure 26: Refined MCNP5 model illustrating the distribution of gamma photons incident on the detector during the transmittance experimentation [14]

Upon comparing the results of the refined MCNP5 model with the experimentally-obtained spectrum, it was identified that the computer software used to perform the analysis integrated solely under the peak corresponding to the Am-241 challenge radionuclide and excluded the counts generated by the secondary X-rays. This exclusion explains why the MCNP5 model over-predicted the experimentally-obtained results; furthermore, it was possible to determine what percentage of the overall transmittance stems from the secondary X-rays by dividing the number of particles incident on the detector with an energy of 58.2 keV by the total number of particles incident on the detector. Using this ratio, the initial transmittance value at 59.5 keV could be adjusted in order to account for the exclusion of the counts generated by the secondary X-rays. Doing so results in an improved MCNP5 model that is fully consistent with the experimentally-obtained transmittance results, given each of their respective uncertainties, as shown in Figure 27.

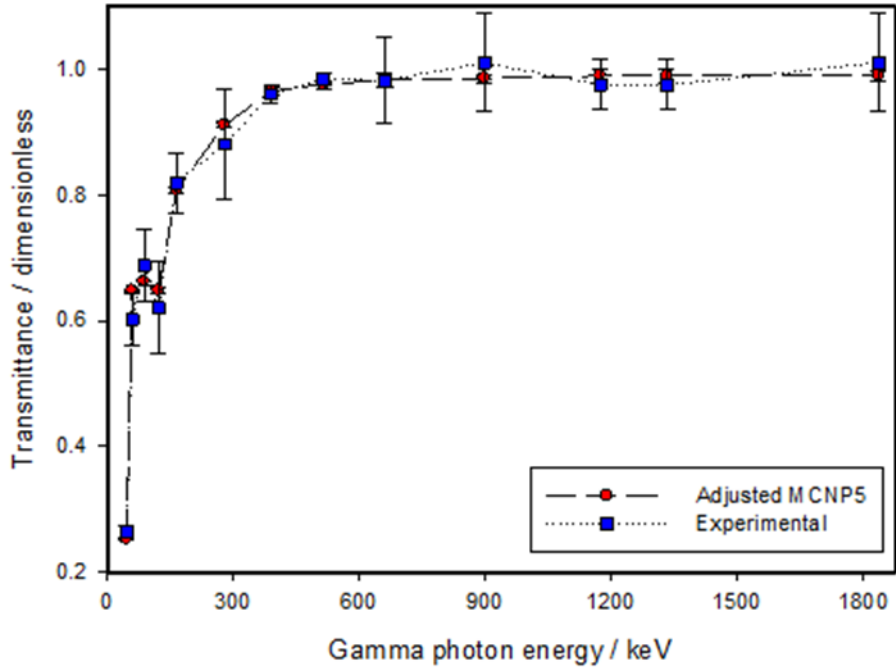


Figure 27: Comparison of experimental and adjusted MCNP5 transmittance results for a single layer of the second generation CRC fabric as a function of gamma photon energy [14]

5.2.6. Summary of transmittance experimentation and MCNP5 modelling

The MCNP5 code was successfully used to model the experimentally-obtained transmittance results for a single layer of the second generation CRC fabric. Additionally, the results illustrate that the software is able to account for the generation and transport of secondary particles which is significant as these species must be considered when determining dose. This demonstrates that the software can be used as a tool to simulate accurately real-world, radiological processes relevant to the use of protective materials in PPE suit concepts. As such, it can be concluded that the MCNP5 software is suitable for use in this thesis and will be used to develop and solve the dosimetric model.

6. MODELLING

As was discussed in the project methodology, it was decided to apply a modelling approach to this project for a number of reasons. Firstly, due to the sensitive nature of radiological material, it is difficult to obtain the regulatory permission necessary to carry out realistic experiments; moreover, the strict safety mandates and security requirements severely limit the types of experimentation that can be conducted. The second consideration was cost. Because the radiological exposure conditions being investigated involve large quantities of radionuclides, varying in type and particulate size, as well as multiple PPE fabrics of differing properties, it was more economical and efficient to construct computer-based models that can simulate the actual physical conditions of interest. Thus, by designing the model such that the user can specify and change the various input parameters as desired, one model can be used to represent numerous real world scenarios without incurring excessive experimental costs or requiring regulatory approval.

In the present work, a two-fold modelling approach was employed in order to quantify the dose imparted to the forearm for each of the aforementioned nine modelling cases. As each of the modelling cases was based on a dispersion event involving the aerosolization of radioactive material, it was first necessary to develop a particulate transport model to determine the concentration of radioactive particulates at five locations surrounding the sleeved forearm. As will be discussed in detail in Section 6.2, three particulate transport models, based on literature data, were created in order to account for each of the three PPE sleeve concepts (air impermeable fabric, air permeable fabric, and no sleeve). The regional concentration data obtained from the particulate transport models were then included as source terms in a dosimetric model, which was used to quantify the dose imparted to the forearm tissue. In this manner, for the nine modelling cases outlined in Section 4.3, it was possible to determine the dose imparted to the forearm as a result of exposure to each set of unique exposure conditions. The following sections seek to explain how the particulate transport and dosimetric models were set up, as well as to identify the key parameters and limitations associated with each.

6.1. Universal Modelling Dimensions

As the output of the particulate transport model was used as an input variable in the dosimetric model, it was necessary that the dimensions of the model geometries be consistent for each. In this regard, before developing either model, it was necessary to decide upon the length and radius of the forearm, the thickness of the air gap between the arm and PPE sleeve, and the thickness of the fabric making

up the PPE sleeve. Additionally, the aerodynamic diameter of the radioactive particulates used in each model was defined in accordance with the radionuclides selected for inclusion in the nine modelling cases.

Because dose is defined as the ratio of the amount of energy deposited to a volume of matter per unit of mass, it was necessary that the dimensions of the forearm be selected so as to be representative of an average military member or first responder and kept uniform for each of the modelling cases [4]. With that in mind, the forearm measurements for an average male member of the CAF were obtained from the Land Forces Anthropometric Survey and are presented in Table 10 [46].

Table 10: Forearm dimensions corresponding to an average male member of the CAF [46]

Measurement Description	Value / cm
Elbow – Wrist Length	28.0 ± 1.4
Forearm Circumference, Relaxed	30.6 ± 1.9
Wrist Circumference	17.6 ± 0.8

According to the above values, the average male forearm has a maximum radius of roughly 4.8 cm at the elbow and decreases to 2.8 cm at the wrist. This gives the forearm the shape of a truncated cone; however, modelling such a shape is more difficult and computationally-intensive than modelling a cylinder. As a result, it was decided to average the two values to produce a cylinder with a uniform radius of 3.8 cm that spanned the entire length from elbow to wrist. For simplicity, the radius of the forearm was rounded to a value of 4.0 cm. Similarly, while the length of the average male forearm was found to be 28.0 cm, an adjusted length of 30 cm was selected for use in each model. It was also necessary to define the thickness of the air gap separating the forearm from the PPE sleeve. This value is heavily dependent on the type of PPE being worn and its location on the body; however, typical thickness range from 0 – 1 cm [47]. As such, an average air gap thickness of 0.5 cm was selected for use in both models.

The next dimension to be included was the thickness of the PPE sleeve fabrics. Because this project considered both air permeable and air impermeable fabrics, thickness values for each of the representative fabrics were obtained from the literature. In this manner, the thickness of the CBRN fabric (air permeable) was set as 1.14 ± 0.02 mm, while that of the second generation CRC fabric (air impermeable) was set as 0.79 ± 0.02 mm [13, 14].

The final dimension to be included in the particulate transport and dosimetric models was the aerodynamic diameter of the airborne radioactive particulates. As the three radionuclides selected for inclusion in the nine modelling cases were Co-

60, Sr-90, and Cs-137, the particulate size was selected so as to be representative of each. Fortunately, experimental testing has indicated that the mean particulate aerodynamic diameter of the aerosols generated in a dispersion scenario for each of the three aforementioned radionuclides is 2.3 μm [35]. As such, a particulate aerodynamic diameter of 2.3 μm was selected for inclusion in each model. A summary of the forearm, air gap, PPE fabric thickness dimensions, and the particulate aerodynamic diameter used in both the particulate transport and dosimetric models is provided in Table 11.

Table 11: Summary of dimensions used in both the particulate transport and dosimetric models

Measurement Description	Value / cm
Forearm, radius	4.0
Forearm, length	30.0
Air gap thickness	0.5
Air permeable fabric thickness	11.4×10^{-2}
Air impermeable fabric thickness	7.9×10^{-2}
Particulate aerodynamic diameter	2.3 μm

6.2. Particulate Transport Model

The primary objective of the particulate transport model was to determine the concentration of radioactive particulates at five regions surrounding the sleeved forearm in response to the exposure conditions defined by the nine modelling cases. The original intent was to use the COMSOL Multiphysics software to develop and solve the particulate transport model; however, due to the fact that the software could not be successfully benchmarked against the particulate transport experimentation, it was necessary to employ a second approach that developed the model from theory and data obtained from the literature. Ultimately, due to differences in particulate transport with regards to air impermeable and air permeable fabrics, separate particulate transport models were created to account for the inclusion of both fabrics in the nine modelling cases. In this manner, one model was used for the cases in which the forearm was surrounded by the air impermeable PPE sleeve with a closure leak and will hereafter be referred to as the first principles model, whilst a second was employed for those involving the air permeable PPE sleeve that was perfectly sealed and will be termed as the penetration model. Further, an additional particulate transport model was developed for the modelling cases in which no PPE sleeve was used. Each of the particulate transport models was designed such that the regional concentration values could be determined and then incorporated as source terms in the dosimetric model. The models are discussed in greater detail in the following sections.

6.2.1. First principles model

The first principles model was designed using fundamental particulate transport theory for the modelling cases in which the PPE sleeve was composed of an air impermeable fabric with a closure leak. As outline in Section 4.2, the second generation CRC fabric was selected to be representative of a generic air impermeable material and, as such, served as the basis when constructing this model. The model geometry was consistent in all aspects with the dimensions outlined in the Section 6.1.

When developing the first principles model, it was assumed that if a PPE sleeve composed of the second generation CRC fabric was placed in an environment with a constant concentration of airborne particulates, these particulates would not be able to diffuse through the fabric of the sleeve, but could gain entry through any improperly sealed closures or leaks. As a result, at any period of time, the particulate concentration within the sleeve would be equivalent to the net rate at which the external particulates entered the sleeve minus the rate at which these particulates had deposited onto the surface of the forearm or inner surface of the sleeve itself. It should be noted that particulates would also have deposited on the outer surface of the PPE sleeve; however, this would have no effect on the inner concentration so long as the outer concentration was assumed to remain constant and unaffected by this process. In the system outlined above, a number of processes are occurring, including the rate of convective transfer of particulates into and out of the PPE sleeve (k_c , k_c'), the rate of deposition of particulates onto the surface of the forearm (k_s) and inner surface of the PPE sleeve (k_{is}), and the rate of attempted diffusion of particulates through the PPE sleeve (k_p). Each of these processes is illustrated in Figure 28.

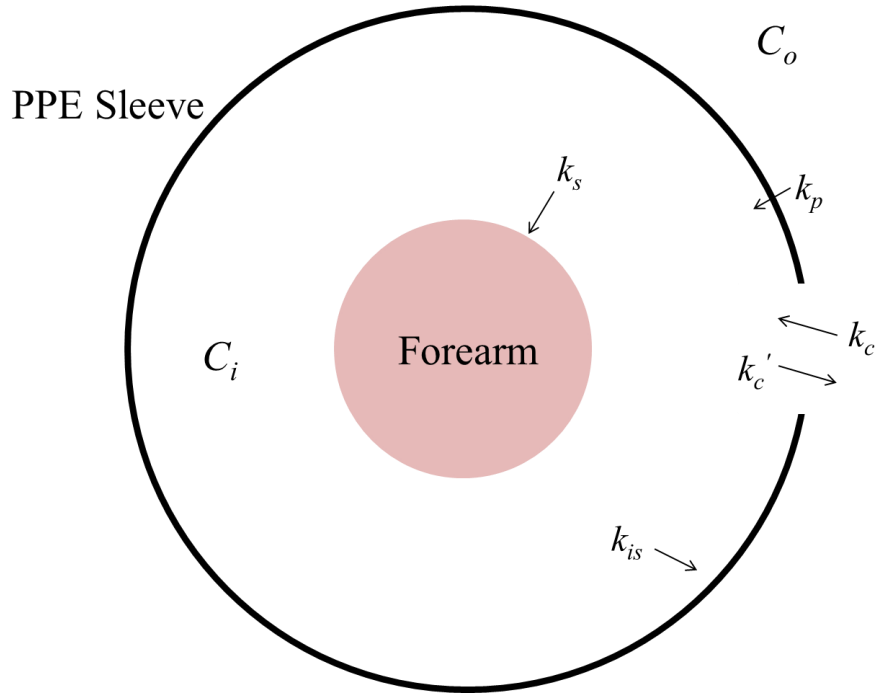


Figure 28: Schematic describing particulate transport for an air impermeable fabric

Assuming that the interior volume is fixed and well-mixed, the inner concentration (C_i) varies as a function of time, the outer concentration (C_o) remains constant, the rates of convection into and out of the PPE sleeve are equal ($k_c = k_c'$), and the rate of diffusion through the fabric of the PPE sleeve is zero, it was possible to describe the above system with Equation 27 [48].

$$\frac{dC_i(t)}{dt} + (k_c + k_s + k_{is})C_i(t) = (k_c)C_o \quad (27)$$

Recall that k_c denotes the rate of convective transfer of particulates into and out of the PPE sleeve, while k_s and k_{is} refer to the rate of deposition of particulates onto the surface of the forearm and inner surface of the PPE sleeve, respectively. This expression was then solved for the time dependent inner concentration as shown in Equation 28.

$$C_i(t) = C_o(t) * \left(\frac{k_c}{k_c + k_s + k_{is}} \right) * (1 - e^{-(k_c + k_s + k_{is}) * t}) \quad (28)$$

Before it was possible to solve Equation 28, it was first necessary to determine the values of each of the rate constants. It was possible to calculate the values of k_s

and k_{is} using their respective deposition velocities. In this regard, the deposition velocities were obtained from the literature and were selected so as to be representative of both the size of the radioactive particulates and the surfaces on which the deposition was taking place, in this case skin and clothing [21]. The former was multiplied by the surface area of the forearm, and the latter by the inner surface area of the PPE sleeve, in order to determine the volumetric flowrate of the particulates depositing on each of the respective surfaces. A factor of two was further included to account for the effects of movement [21]. The values for the surface areas were calculated based on the dimensions outlined in Section 6.1. The resulting volumetric flowrates were then divided by the volume of the air gap between the forearm and PPE sleeve to calculate the values of the rate constants k_s and k_{is} .

In order to determine the value of k_c , it is important to remember that the second generation CRC fabric meets the NFPA 1994 Class 2 protection requirements when incorporated into a suit with a particular maximum leakage rate for vapour agents [16]. As such, the suit is required to provide a protection factor, defined as the ratio of the outer concentration to inner concentration, of 180 in the region of the arm [49]. A literature review of experimental studies indicated that skin and cloth deposition velocities are commonly accepted to be 2 cm min^{-1} and 0 cm min^{-1} , respectively, for vapor agents [50]. These values were then used to calculate k_s and k_{is} , for a scenario involving exposure to a vapor agent, in the same manner as outlined above. Using these values and a protection factor of 180, it was then possible to rearrange Equation 28 and solve for the value of k_c . While the value of k_c was calculated for vapor agents, it is not unreasonable to use an equivalent value for an aerosol agent as, in either case, k_c is a result of the convective flow of the air and not the ‘contaminant’ following the airstream [17]. In this manner, it was possible to determine values for each of the three rate constants. The values of k_s , k_{is} , and k_c used in the first principles model are presented as a function of deposition velocity in Table 12.

Table 12: Summary of k_s , k_{is} , and k_c values used in the first principles model

Deposition Velocity ($2.3 \mu\text{m}$) / m s^{-1}		k_s / min^{-1}	k_{is} / min^{-1}	k_c / min^{-1}
Skin	Clothing			
0.0062 [21]	0.0023 [21]	140	59	0.021

Having determined the values for each of the rate constants, it was possible to define the expressions that would be used in the first principles model to determine each of the five regional concentration values (C_o , C_i , $C_{outersuit}$, $C_{immersuit}$, and C_{skin}) in the cases where the forearm was protected by an air impermeable PPE sleeve. For each of the modelling cases being investigated, the outer concentration was assumed to be a constant value independent of time and was referenced from the

literature data [35]. Using this value and those of the previously-calculated rate constants, it was possible to calculate the inner concentration as a function of time using Equation 28.

Having determined values for C_o and C_i , it was then possible to calculate each of the surface concentrations as a function of time. Equation 29 illustrates the expression used to determine $C_{outersuit}$.

$$C_{outersuit}(t) = 2 * v_{dep,cloth} \int_0^t C_o(t) * dt \quad (29)$$

However, given that C_o was assumed to be a constant, Equation 29 could be further simplified.

$$C_{outersuit}(t) = 2 * v_{dep,cloth} * C_o * t \quad (30)$$

Similarly, Equation 28 can be substituted into Equation 31 and Equation 32 in order to determine $C_{innersuit}$ and C_{skin} , respectively.

$$C_{innersuit}(t) = 2 * v_{dep,cloth} \int_0^t C_i(t) * dt \quad (31)$$

$$C_{skin}(t) = 2 * v_{dep,skin} \int_0^t C_i(t) * dt \quad (32)$$

In the above equations, $v_{dep,cloth}$ refers to the deposition velocity for clothing, $v_{dep,skin}$ refers to the deposition velocity for skin, and the factor of two was included to account for an increased deposition velocity due to movement [21]. Deposition velocity varies as a function of both particulate size and surface type [21]. As such, it was necessary to obtain literature values that were reflective of the radionuclides selected for inclusion in the modelling cases, each of which has a mean aerodynamic diameter of 2.3 μm as outlined in Section 6.1, and the surfaces on which the deposition was taking place, in this case skin and clothing. Additionally, because there is a significant amount of deviation amongst published deposition velocities, developing the model in this manner would allow for a wide spectrum of values to be tested and the resulting effect on the regional concentration values to be observed [20, 21]. While this is not performed in the present thesis, it may be completed in a future work looking to develop a more robust particulate transport model as discussed in greater detail in Chapter 8.

Using the equations presented above, the first principles model could be used to determine each of the five regional concentration values as a function of time. It is important to note that this model was only applicable for each of the modelling cases in which the PPE sleeve was composed of an air impermeable fabric. For the

modelling cases that involved an air permeable PPE sleeve or no sleeve, separate particulate transport models were developed.

6.2.2. Penetration model

The particulate transport model developed from first principles was only applicable to air impermeable fabrics. The reason for this stems from the fact that k_p was assumed to be zero, which is not the case for an air permeable fabric. Whilst it may have been possible to determine k_p for an air permeable fabric using its diffusion coefficient, this value was not known with certainty for the CBRN fabric. Additionally, the first principles model was designed to account for leaks caused by improperly sealed closures and, as such, was heavily influenced by the convective transfer of the particulates into and out of the confines of the PPE sleeve. In this work, it was assumed that the air permeable fabric was perfectly sealed and that the only way for particulates to gain entry to the volume within the PPE sleeve was by penetrating through the fabric itself. In this manner, a penetration model, based on particulate transport data obtained from the literature, had to be constructed for the modelling cases in which the PPE sleeve was composed of an air permeable fabric. Again, all aspects of the model geometry were consistent with the values presented in Section 6.1.

A literature search was conducted in order to obtain data that would be suitable for inclusion in the penetration model. The most important criterion when selecting the data was that it needed to be appropriate to the nine modelling cases selected for analysis in this project. In this regard, it was desired that the experimentation be representative of a dispersion event and that it test the ability of particulates in the 2.3 μm -size range to penetrate a material with similar properties to that of the CBRN fabric. A study, entitled '*Aerosol penetration through protective fabrics*', was found with experimental parameters that met each of the aforementioned criteria [23]. The aim of the study was to evaluate the aerosol penetration efficiency for three different PPE fabrics under a variety of different test conditions [23]. To accomplish this, an aerosol swatch test rig was developed such that the concentration of particulates upstream and downstream from the swatch of PPE fabric could be measured for different particulate sizes and face velocities [23]. In this manner, it was possible to express the aerosol penetration efficiency, P , as the ratio of the downstream concentration, C_{down} , to the upstream concentration, C_{up} [23]. The resulting expression is presented in Equation 33.

$$P = \frac{C_{down}}{C_{up}} \quad (33)$$

The experimentation was designed such that multiple trials were conducted to determine the penetration efficiency for three different PPE fabrics at three

different face velocities as a function of particulate size [23]. For each trial, a sodium chloride-based salt aerosol, consisting of particulates ranging in diameter from 0.03 – 3.0 μm , was generated upstream of the fabric swatch [23]. A mass flow controller was then used to manipulate the flow of the particulates such that face velocities of 5, 10, or 25 cm s^{-1} were created at the surface of the fabric swatch [23]. The three PPE fabrics included in the study were the Remploy No.1 NCB MKIV over-garment, Melba Industries Black CB Suit, and the Paul Boyé suit, each of which is currently in use by either the Australian or Singapore Defence Force [23]. For each combination of parameters, the testing apparatus was run for a period of 30 min to achieve steady-state conditions [23]. After this time period, isokinetic sampling was conducted upstream and downstream of the fabric swatch and the particulate concentration measurements were binned according to size intervals of 0.03 – 0.3 μm , 0.3 – 1.0 μm , and 1.0 – 3.0 μm [23]. By taking the ratio of these measurements, it was possible to determine the penetration efficiency for the given set of parameters as a function of particulate size. For additional detail regarding the experimental methodology, set-up, or apparatuses, refer to Reference 23.

When deciding which of the study results to use in the penetration model, it was necessary to select the data that best represented the exposure conditions outlined in the nine modelling cases. In this regard, results obtained for the combination of experimental parameters (particulate size, type of PPE fabric, and air face velocity) that best correspond to the performance of the CBRN fabric during a radiological dispersion event were included. Logically, it was decided to base the penetration model off of the experimental results obtained for particulates in the 1.0 – 3.0 μm size range as each of the radionuclides selected for analysis in this work has an aerodynamic diameter of 2.3 μm . When comparing each of the three fabrics tested in the study to the CBRN fabric, it was evident that the Paul Boyé fabric was most comparable; moreover, as presented in Table 13, the material properties for the CBRN and Paul Boyé fabrics are very similar. As such, it was decided to include the experimentally-obtained results for the Paul Boyé fabric in the penetration model. The final experimental parameter to consider was the air face velocity. Because air face velocity was not an exposure condition that was explicitly defined in the modelling cases², the results obtained at 10 cm s^{-1} were used as they yielded the highest penetration efficiency given the selection of the other two parameters. In this manner, it was decided to model the worst-case scenario as the increased penetration efficiency corresponds to a higher inner concentration of radioactive particulates, which would result in a greater dose imparted to the forearm tissue.

² In a dispersion event scenario, at a given location downwind of the release, the dose that is contributed by airborne particulates is independent of wind speed, as concentration and time are inversely related.

Table 13: Comparison of the CBRN fabric and Paul Boyé fabric

Property	CBRN fabric [12]	Paul Boyé fabric [23]
Construction	Outer: woven cloth Inner: composite bonded filter material w/ activated carbon	Outer: twill weave Inner: carbon impregnated foam bonded to a skin liner
Mass per unit area / g m^{-2}	510 (max)	452 ± 5
Thickness / mm	1.5 (max)	1.9 ± 0.2
Air Permeability / mm s^{-1}	250	248 ± 16

For the given set of parameters outlined above, it was possible to determine a penetration efficiency value from the experimental study that was deemed to be representative of the modelling cases involving the PPE sleeve concept composed of an air permeable fabric. The experimental study found that the penetration efficiency of particulates in the 1.0 – 3.0 μm size range for the Paul Boyé fabric at a face velocity³ of 10 cm s^{-1} was 0.763 ± 0.012 [23]. This penetration efficiency value was subsequently selected for inclusion in the penetration model. The study results for the remaining combination of experimental parameters have been included in Appendix E.

Having determined the penetration efficiency to be used in the penetration model, it was possible to use this value to determine the inner concentration of particulates as a presented in Equation 34.

$$C_i(t) = P * C_o(t) \quad (34)$$

Because penetration efficiency is a property of the material, it takes very little time for steady state conditions to be achieved and its value does not change significantly with time (provided any clogging effects are neglected). As such, for this thesis, it was assumed that the penetration efficiency through the air permeable fabric remained constant at 0.763 for the time interval investigated. With this in mind, it was possible to calculate the inner concentration of particulates, C_i , as a function of time.

³ The study does not present the corresponding wind speed but does state that it is representative of the wind conditions likely to occur in a real-world environment.

As in the first principles model, the outer concentration, C_o , was assumed to be a constant value that was referenced from literature data depending on the modelling case being investigated [35]. Having determined the values of C_i and C_o , it was then possible to employ Equation 30, Equation 31, and Equation 32 from the first principles model in the penetration model to calculate $C_{outersuit}$, $C_{innersuit}$, and C_{skin} , respectively. In this manner, the penetration model was used to determine each of the five regional concentration values for the modelling cases involving the air permeable PPE sleeve concept such that they could be included as source terms in the dosimetric model.

6.2.3. No shielding cases

For the modelling cases in which no PPE sleeve was used to protect the forearm, fundamental particulate transport theory was used to determine the regional concentration values. All aspects of the model geometry remained consistent with the dimensions outlined in Section 6.1; however, due to the absence of a PPE sleeve, the outer volume was expanded so as to encompass the outer sleeve, inner sleeve, and inner volume regions that were previously defined in the first principles and penetration models. As a result of this simplified geometry, it was only necessary to determine the concentration of particulates on the surface of the forearm, C_{skin} , and in the surrounding outer volume, C_o .

As in the first principles and penetration models, C_o was assumed to be a constant value, independent of time, which was referenced from literature data depending on the modelling case under analysis [35]. Using this value, it was possible to calculate C_{skin} as a function of time using Equation 35. The value of the skin deposition velocity is provided in Table 12.

$$C_{skin}(t) = 2 * v_{dep,skin} * C_o * t \quad (35)$$

In this manner, it was possible to employ fundamental particle transport theory to determine each of the regional concentration values for the modelling cases in which no PPE sleeve was present. These values could then be integrated as source terms in the dosimetric model.

6.3. Dosimetric model

The purpose of the dosimetric model was to determine the dose imparted to the forearm tissue for each set of exposure conditions outlined by the modelling cases. It was possible to not only determine the dose imparted to the forearm as a result of exposure to various radiation environments, but also to investigate the level of protection offered by the various types of PPE fabrics against both gamma and beta

radiation and to determine the contribution of each type of radiation to the total overall dose. Additionally, the modelling results enabled comparison with the aforementioned acceptable exposure limits put forth by the ICRP.

As discussed in the previous chapter, the MCNP5 code was successfully benchmarked against the data collected during the gamma photon transmittance experimentation and deemed suitable for use in the remainder of this work. As a result, MCNP5 was selected for use in developing and solving the dosimetric model for each of the nine modelling cases outlined in Table 5. The following section seeks to explain how the MCNP5 code was used to create the dosimetric model.

The first stage in the developing the dosimetric model was to construct the model geometry. Within the MCNP5 input file, the cell card was used to define the location and density of each of the different materials included in the model, whilst the surface card was used to construct the geometric structure of the model. In this regard, right circular cylinders of various sizes, used to represent the forearm and PPE sleeve, were located within a much larger cylinder that simulated the external environment. The dimensions of each structure were defined in accordance with those of the particulate transport model as per the previously outlined universal modelling dimensions (Section 6.1). The cylinder used to represent the forearm was filled with human tissue, whilst the other mimicked the composition of the PPE sleeve, be it the air impermeable or air permeable fabric. Recall that the second generation CRC fabric was selected to be representative of a generic air impermeable fabric and the CBRN fabric was chosen to characterize an air permeable fabric. For the modelling cases in which no PPE sleeve was used, the cylinder used to represent the PPE sleeve was filled with air. Finally, the remainder of the model geometry, including the air gap and surrounding environment, was filled with air. The density and elemental composition of each of the materials used in the dosimetric model are presented in Table 14. A schematic of the dosimetric model geometry is illustrated in Figure 29.

Table 14: Density and elemental composition of each material used in the dosimetric model

Material	Density / g cm ⁻³	Composition	
		Element	wt %
Air Impermeable Fabric [14]	2.4	C	24.0
		O	2.0
		W	16.0
		Bi	58.0
Air Permeable Fabric [12]	0.219	C	74.15
		O	24.85
Human Tissue [51]	0.52633	H	10.454
		C	22.663
		N	2.490
		O	63.525
		Na, Mg, Si, P, S, Cl, K, Ca, Fe, Zn, Rb, Zr	trace
Air [52]	0.001	C	trace
		N	75.527
		O	23.178
		Ar	1.283

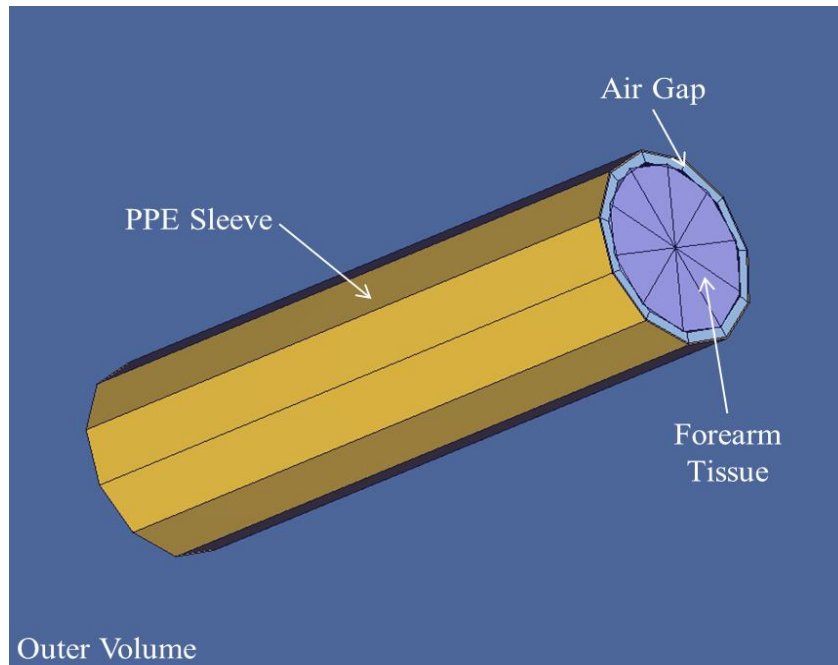


Figure 29: Schematic of the dosimetric model geometry

Having constructed the model geometry, it was then possible to define the location and type of radiation source. The location of the source was modelled in accordance with the regional concentration values obtained from the particulate transport model. Unique source terms were included to represent the presence of the radioactive particulates at five different locations relative to the model geometry: on the surface of the forearm, in the inner air gap, on the inner surface of the PPE sleeve, on the outer surface of the PPE sleeve, and in the outer environment. Defining a source location in MCNP5 is equivalent to specifying the region in which the source particles originate. Thus, for each source particle that the code is told to run, the code randomly assigns a starting location somewhere within the boundaries outlined by the source definition. In this regard, by running a large number of source particles, it is possible to effectively populate the defined source location. This is important as regardless of which radiological quantity is being solved for, the code sums the results of each of the individual source particle runs and averages the total according to the total number of particle histories. As a result, the output generated by the code corresponds to that of a single source particle that is reflective of the location and contribution of all the source particles run. Figure 30 illustrates each of the five source term locations with respect to the forearm and PPE sleeve. Note that the red dots correspond to the randomly-assigned origins of each of the individual source particles within the five source locations.

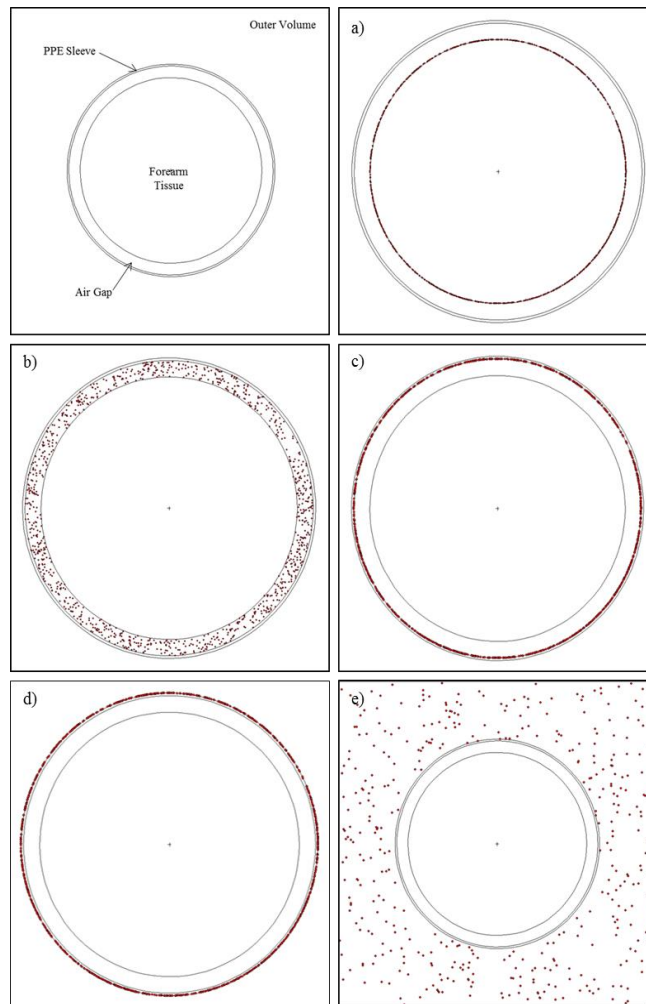


Figure 30: End view of the dosimetric model geometry illustrating each of the five source locations: a) surface of the forearm, b) inner air gap, c) inner surface of the PPE sleeve, d) outer surface of the PPE sleeve, and e) outer environment

It was decided to use separate input files to model the five source locations, as opposed to amalgamating each into a single file, as this allowed for the contribution of dose from each region to be assessed relative to the total dose. For example, by designing the dosimetric model in this manner, it was possible to compare the dose imparted to the forearm from the particulates located on the surface of the arm itself with the dose contributed by the particulates in the outer environment. For the modelling cases in which no PPE sleeve was used to protect the forearm, it was only necessary to define two source locations: on the surface of the forearm and in the surrounding outer environment. For these cases, the outer

volume was defined so as to encompass the regions previously defined as outer suit, PPE sleeve, inner suit, and inner volume.

The modelling case being investigated also had an impact on how the source was defined. In this sense, individual sources needed to be created to account for the fact that Co-60, Sr-90, and Cs-137 were the three radionuclides selected for inclusion in the nine modelling cases and each has a unique decay scheme. The energy and decay probability for each radionuclide, as included in the dosimetric model, is presented in Table 15. Because the MCNP5 code is only able to generate one type of source particle at a time, it was necessary to use two input files for the radionuclides that emitted both gamma and beta radiation. The overall dose imparted to the forearm could then be calculated by summing the results of each. Also, developing the dosimetric model in this manner allowed for contribution of each type of radiation to the total overall dose to be determined.

Table 15: Decay schemes for Co-60, Sr-90, and Cs-137 as used in the dosimetric model [36, 39, 40]

Radionuclide	Type of Radiation	Energy / keV	Decay Probability / %
Co-60	γ_{1a}	1.173	100
	γ_{1b}	1.332	100
	β_1	0.318	100
Sr-90	β_1	0.546	100
Cs-137	γ_1	0.662	94.4
	β_1	0.514	94.4
	β_2	1.176	5.6

Having fully defined the source for each of the modelling cases, it was then necessary to select the type of tally. While the MCNP5 code is capable of performing numerous tallies, an *f8 or energy deposition tally was selected for use in the dosimetric model. This type of tally works by summing the total amount of energy (nominal units of MeV) deposited as a result of nuclear interactions within a specified volume, in this case the volume of the forearm tissue cylinder, per source particle [44]. As the volume and density of the forearm cylinder are known, it is possible to calculate the corresponding mass of tissue within the geometry. This is significant because in order to relate the tally output to a dosimetric value, it must then be divided by the mass of the forearm tissue cylinder [44]. The model results now have units of MeV g⁻¹ per source particle, which can be easily converted to other dosimetric units for the purpose of comparison (*e.g.*, Gy or Sv). As outlined in Section 5.2.1, MCNP5 is a stochastic code, which means that this process is repeated multiple times according to the number of source particles to be run and then averaged to determine a mean value per source particle and an associated uncertainty [44]. In this manner, for each of the five source locations, it

was possible to use an *f8 tally to determine the average dose imparted to the forearm tissue per source particle and an associated uncertainty. An example of one of the MCNP5 input files used in the dosimetric model has been included for reference in Appendix F.

Because MCNP5 determines the dose imparted to the forearm per source particle, these values were then multiplied by the regional concentration data obtained from the particulate transport model in order to scale the dosimetric model results based on the number of particles present at each of the five locations (two locations for the modelling cases involving no PPE sleeve). The regional dose values could then be summed in order to determine the total dose imparted to the forearm. The results of the particulate transport model were integrated with those of the dosimetric model to determine the total dose imparted to the forearm tissue as a result of each set of exposure conditions outlined by the nine modelling cases.

7. RESULTS AND DISCUSSION

The following chapter commences with a discussion of the results generated by both the particulate transport and dosimetric models. The outputs of the latter were then multiplied by those of the former in order to scale the dose imparted to the forearm tissue according to the concentration of particulates present at each of the five source locations (two locations for the modelling cases involving no PPE sleeve). In this manner, the results of the particulate transport model were integrated with those of the dosimetric model to determine the total dose imparted to the forearm tissue for each set of exposure conditions defined in the nine modelling cases (Table 5). The chapter concludes with a discussion of the integrated results.

7.1. Particulate Transport Model

The objective of the particulate transport model was to determine the concentration of radioactive particulates in five regions surrounding the sleeved forearm. Due to differences in particulate transport across air impermeable and air permeable fabrics, it was necessary to develop two separate models to account for the inclusion of both fabrics in the nine modelling cases. In this regard, a first principles model was designed for the cases involving the air impermeable PPE sleeve with a closure leak, while a penetration model was developed for those involving the air permeable fabric that was perfectly sealed. The results of both particulate transport models are presented in the following sections, along with a discussion comparing the results of each. Finally, the particulate transport model results for the modelling cases in which the forearm was not protected by a PPE sleeve are presented and analyzed for comparison.

7.1.1. First principles model

The first principles model was used to determine the five regional concentration values (C_o , C_i , $C_{outersuit}$, $C_{innersuit}$, and C_{skin}) for the modelling cases in which the PPE sleeve was composed of the air impermeable fabric. Recall that this model was based on the assumption that particulates could only gain entry to the inner confines of the PPE sleeve via transport through a closure leak and not as a result of diffusing through the impermeable fabric making up the sleeve. The second generation CRC fabric of interest was selected as the representative air impermeable fabric to be analyzed in this project. For the modelling cases involving the air impermeable fabric, the first principles model was used to analyze the transport of each of the three radionuclides (Co-60, Sr-90, and Cs-137) selected for inclusion in this thesis.

For each radionuclide under analysis, the outer concentration, as outlined in Section 6.2.1, was assumed to be a constant value, independent of time; moreover, these values were obtained from a literature study that measured the concentration of a variety of different radioactive aerosols following the simulated detonation of a radiological weapon [35]. The study was conducted such that measurements were collected close to the ground at a location 100 m from the detonation site, assuming that the aerosolized particulates were carried by wind with an average velocity of 3 m s^{-1} [35]. Additionally, the study results represent the average concentration of particulates present in the air over a period of fifteen minutes for outdoor conditions [35]. As a result, using the outer concentrations reported by the study represents modelling a severe worst-case dispersion event scenario as it is more likely that the outer concentration of particulates would decrease with time as the plume of dispersed material is affected by meteorological phenomena instead of remaining at a constant value.

The outer concentration values used in the first principles model for each radionuclide are presented in Table 16. It should be noted that the outer concentration values in Table 16 are activity concentrations. As explained in Section 2.1.1, activity denotes the rate at which a radioactive species undergoes decay per unit time; as such, determining each of the regional concentration values in terms of an activity facilitated the later integration of the particulate transport results with those of the dosimetric model.

Table 16: Outer concentration values used in the first principles model for each radionuclide [35]

Radionuclide	$C_o / \text{Bq m}^{-3}$
Co-60	1.5×10^6
Sr-90	1.5×10^8
Cs-137	1.3×10^8

Using the outer concentration values listed in Table 16 and the rate constant and deposition velocity parameters from Table 12, it was possible to determine the inner concentration and outer suit concentration values as a function of time by solving Equation 28 and Equation 30, respectively. The inner concentration values could then be substituted into Equation 31 and Equation 32 to calculate the time dependent inner suit and skin concentrations. As the inner concentration remained unchanged over the time period investigated, it was considered a constant when solving Equation 31 and Equation 32. In this manner, it was possible to use the first principles model to determine the five regional concentration values as a function of time for the three modelling cases involving the air impermeable fabric with a closure leak, one for each of the radionuclides of interest. Table 17 contains the results generated by the first principles model for the modelling case involving the

air impermeable fabric and Co-60 particulates. It was decided to present the results on fifteen minute intervals for the first hour and then every sixty minutes up to a maximum time of three hours. Similar tables were produced for the modelling cases involving Sr-90 and Cs-137 and are included for reference in Appendix G.

Table 17: Regional concentration values generated by the first principles model for the case in which the air impermeable fabric was exposed to Co-60 particulates

Time / min	C_o / Bq m⁻³	$C_{outersuit}$ / Bq m⁻²	C_i / Bq m⁻³	$C_{innersuit}$ / Bq m⁻²	C_{skin} / Bq m⁻²
0	1.5E+06	0.0E+00	0.0E+00	0.0E+00	0.0E+00
15	1.5E+06	6.1E+06	1.5E+02	6.4E+02	1.7E+03
30	1.5E+06	1.2E+07	1.5E+02	1.3E+03	3.5E+03
45	1.5E+06	1.8E+07	1.5E+02	1.9E+03	5.2E+03
60	1.5E+06	2.4E+07	1.5E+02	2.6E+03	6.9E+03
120	1.5E+06	4.9E+07	1.5E+02	5.2E+03	1.4E+04
180	1.5E+06	7.3E+07	1.5E+02	7.7E+03	2.1E+04

In order to determine the total activity of the particulates within each region, the regional concentration values were then multiplied by the area or volume of their respective regions. Given that the PPE sleeve was composed of the air impermeable fabric, the magnitudes of the outer and inner volumes and outer sleeve, inner sleeve, and forearm surface areas were calculated in accordance with the dimensions outlined in Section 6.1 and are listed in Table 18.

Table 18: Magnitudes of each of the five regions for the PPE sleeve composed of the air impermeable fabric

Region	Area or Volume
Outer volume	942.4 x 10 ⁵ cm ³
Surface area of outer sleeve	863.1 cm ²
Surface area of inner sleeve	848.2 cm ²
Inner volume	400.6 cm ³
Surface area of a forearm	754.0 cm ²

The reasons for scaling the regional concentration values by their corresponding volume or surface area magnitudes were two-fold. Firstly, it gave a more accurate representation of the total number of radioactive decay events occurring within each region. Furthermore, because activity is proportional to the number of radioactive particulates present, it provided a better means by which to analyze the first principles model results from a particulate transport standpoint. Secondly, because the output of the dosimetric model defines the dose imparted to

the forearm tissue on a per source particle basis, knowing the total number of particulates undergoing decay events per second at each region greatly facilitated the integration of the particulate transport model results with those obtained from the dosimetric model. Table 19, Table 20, and Table 21 present the regional activity values for the modelling cases involving the air impermeable fabric and Co-60, Sr-90, and Cs-137 particulates, respectively.

Table 19: Regional activity values for the modelling case in which the air impermeable fabric was exposed to Co-60 particulates

Time / min	A_o / Bq	$A_{outersuit}$ / Bq	A_i / Bq	$A_{innersuit}$ / Bq	A_{skin} / Bq
0	1.4E+08	0.0E+00	0.0E+00	0.0E+00	0.0E+00
15	1.4E+08	5.3E+05	6.2E-02	5.5E+01	1.3E+02
30	1.4E+08	1.1E+06	6.2E-02	1.1E+02	2.6E+02
45	1.4E+08	1.6E+06	6.2E-02	1.6E+02	3.9E+02
60	1.4E+08	2.1E+06	6.2E-02	2.2E+02	5.2E+02
120	1.4E+08	4.2E+06	6.2E-02	4.4E+02	1.0E+03
180	1.4E+08	6.3E+06	6.2E-02	6.6E+02	1.6E+03

Table 20: Regional activity values for the modelling case in which the air impermeable fabric was exposed to Sr-90 particulates

Time / min	A_o / Bq	$A_{outersuit}$ / Bq	A_i / Bq	$A_{innersuit}$ / Bq	A_{skin} / Bq
0	1.4E+10	0.0E+00	0.0E+00	0.0E+00	0.0E+00
15	1.4E+10	5.3E+07	6.2E+00	5.5E+03	1.3E+04
30	1.4E+10	1.1E+08	6.2E+00	1.1E+04	2.6E+04
45	1.4E+10	1.6E+08	6.2E+00	1.6E+04	3.9E+04
60	1.4E+10	2.1E+08	6.2E+00	2.2E+04	5.2E+04
120	1.4E+10	4.2E+08	6.2E+00	4.4E+04	1.0E+05
180	1.4E+10	6.3E+08	6.2E+00	6.6E+04	1.6E+05

Table 21: Regional activity values for the modelling case in which the air impermeable fabric was exposed to Cs-137 particulates

Time / min	A_o / Bq	$A_{outersuit}$ / Bq	A_i / Bq	$A_{innersuit}$ / Bq	A_{skin} / Bq
0	1.2E+10	0.0E+00	0.0E+00	0.0E+00	0.0E+00
15	1.2E+10	4.6E+07	5.3E+00	4.7E+03	1.1E+04
30	1.2E+10	9.1E+07	5.3E+00	9.4E+03	2.3E+04
45	1.2E+10	1.4E+08	5.3E+00	1.4E+04	3.4E+04
60	1.2E+10	1.8E+08	5.3E+00	1.9E+04	4.5E+04
120	1.2E+10	3.7E+08	5.3E+00	3.8E+04	9.0E+04
180	1.2E+10	5.5E+08	5.3E+00	5.7E+04	1.4E+05

The regional activity values determined using the first principles model illustrate several important trends regarding particulate transport through closure leaks in the air impermeable fabric. The first trend is that, for each of the radionuclides analyzed, there existed a significantly higher activity outside of the protective confines of the PPE sleeve than inside. This indicates that a relatively low number of radioactive particulates were able to gain entry into the sleeve through closure leaks and is illustrated by the fact that, in each of the above tables, A_o and $A_{outersuit}$ are several orders of magnitude greater than A_i , $A_{innersuit}$, and A_{skin} . This result is indicative of the relatively low value for the rate of convective transfer of particulates into the air impermeable PPE sleeve that was determined in Section 6.2.1, using the protection factor required for NFPA 1994 Class 2 approval. Secondly, the results indicated that A_i achieves steady-state almost instantaneously. While difficult to see given the time scale presented in the above tables, for each of the three radionuclide species, A_i reached its steady-state value in less than 5 s. The reason that steady-state was achieved so quickly is due to the fact that the particulates are depositing on the inner surface of the PPE sleeve and skin much more quickly than they are entering the inner confines of the sleeve. The rate constants used in the first principles model are shown Table 12 and, as k_{is} and k_s are much greater than k_c , further explain why the values of $A_{innersuit}$ and A_{skin} are several orders of magnitude higher than that of A_i in each of the above tables. It should be noted that a particulate resuspension factor was not accounted for in the first principles model, but represents another parameter that could be included in a more robust particulate transport model and warrants investigation as part of a follow-on work.

7.1.2. Penetration model

As the first principles model was only applicable to the modelling cases in which the PPE sleeve was composed of the air impermeable fabric, the penetration model was used for those cases involving the air permeable PPE sleeve concept. Recall that, unlike the first principles model, the penetration model assumed the PPE sleeve was perfectly sealed (no closure leakage) and that the only way for particulates to gain entry to its inner confines was by penetrating through the air permeable fabric. The CBRN fabric was selected as the representative air permeable fabric. In this regard, for the modelling cases involving the air permeable fabric, the penetration model was used to determine the five regional concentration values for each of the three radionuclide species.

Similar to the first principles model, the outer concentration values were obtained from the literature and assumed to remain constant with time [35]. These values are presented in Table 16. Using these values and the clothing deposition velocity listed in Table 12, Equation 30 could then be solved to determine the concentration of particulates on the outer surface of the PPE sleeve. In order to solve for the inner concentration as a function of time, Equation 34 was used assuming a constant penetration efficiency of 0.763. As outlined in Section 6.2.2, this datum was obtained from a literature study testing the penetration of aerosols through various types of protective fabrics, one of which had properties very similar to that of the CBRN fabric of interest [23]. In this manner, it was possible to determine the inner concentration as a function of time for the three radionuclides. These inner concentration expressions could then be included in Equation 31 and Equation 32 to solve for the time dependent inner sleeve and skin surface concentrations. Table 22 contains the regional concentration results generated using the penetration model for the modelling case involving the air permeable PPE sleeve and Co-60 particulates. Similar tables were produced for the modelling cases involving Sr-90 and Cs-137 and are included for reference in Appendix H.

Table 22: Regional concentration values generated by the penetration model for the case in which the air permeable fabric was exposed to Co-60 particulates

Time / min	C_o / Bq m ⁻³	$C_{outersuit}$ / Bq m ⁻²	C_i / Bq m ⁻³	$C_{innersuit}$ / Bq m ⁻²	C_{skin} / Bq m ⁻²
0	1.5E+06	0.0E+00	0.0E+00	0.0E+00	0.0E+00
15	1.5E+06	6.1E+06	1.1E+06	4.7E+06	1.3E+07
30	1.5E+06	1.2E+07	1.1E+06	9.3E+06	2.5E+07
45	1.5E+06	1.8E+07	1.1E+06	1.4E+07	3.8E+07
60	1.5E+06	2.4E+07	1.1E+06	1.9E+07	5.0E+07
120	1.5E+06	4.9E+07	1.1E+06	3.7E+07	1.0E+08
180	1.5E+06	7.3E+07	1.1E+06	5.6E+07	1.5E+08

As with the outputs of the first principles model, the regional concentration values were then multiplied by the magnitude of their respective volumes or surface areas in order to determine the total activity of the particulates within each region. The area or volume of each of the five regions are listed in Table 23 and were calculated in accordance with the dimensions outlined in Section 6.1.

Table 23: Magnitudes of each of the five regions for the PPE sleeve composed of the air permeable fabric

Region	Area or Volume
Outer volume	942.5 x 10 ⁵ cm ³
Surface area of outer sleeve	869.7 cm ²
Surface area of inner sleeve	848.2 cm ²
Inner volume	400.6 cm ³
Surface area of a forearm	754.0 cm ²

The regional activity values for the modelling cases involving the air permeable fabric and Co-60, Sr-90, and Cs-137 particulates are presented in Table 24, Table 25, and Table 26, respectively. Recall that the reasons for scaling the penetration model results according to their geometric magnitudes were that doing so provided a better representation of the total number of radioactive decay events occurring within each region and facilitated their integration with the outputs of the dosimetric model.

Table 24: Regional activity values for the modelling case in which the air permeable fabric was exposed to Co-60 particulates

Time / min	A_o / Bq	$A_{outersuit}$ / Bq	A_i / Bq	$A_{innersuit}$ / Bq	A_{skin} / Bq
0	1.4E+08	0.0E+00	0.0E+00	0.0E+00	0.0E+00
15	1.4E+08	5.3E+05	4.5E+02	4.0E+05	9.5E+05
30	1.4E+08	1.1E+06	4.5E+02	7.9E+05	1.9E+06
45	1.4E+08	1.6E+06	4.5E+02	1.2E+06	2.8E+06
60	1.4E+08	2.1E+06	4.5E+02	1.6E+06	3.8E+06
120	1.4E+08	4.3E+06	4.5E+02	3.2E+06	7.6E+06
180	1.4E+08	6.4E+06	4.5E+02	4.8E+06	1.1E+07

Table 25: Regional activity values for the modelling case in which the air permeable fabric was exposed to Sr-90 particulates

Time / min	A_o / Bq	$A_{outersuit}$ / Bq	A_i / Bq	$A_{innersuit}$ / Bq	A_{skin} / Bq
0	1.4E+10	0.0E+00	0.0E+00	0.0E+00	0.0E+00
15	1.4E+10	5.3E+07	4.5E+04	4.0E+07	9.5E+07
30	1.4E+10	1.1E+08	4.5E+04	7.9E+07	1.9E+08
45	1.4E+10	1.6E+08	4.5E+04	1.2E+08	2.8E+08
60	1.4E+10	2.1E+08	4.5E+04	1.6E+08	3.8E+08
120	1.4E+10	4.3E+08	4.5E+04	3.2E+08	7.6E+08
180	1.4E+10	6.4E+08	4.5E+04	4.8E+08	1.1E+09

Table 26: Regional activity values for the modelling case in which the air permeable fabric was exposed to Cs-137 particulates

Time / min	A_o / Bq	$A_{outersuit}$ / Bq	A_i / Bq	$A_{innersuit}$ / Bq	A_{skin} / Bq
0	1.2E+10	0.0E+00	0.0E+00	0.0E+00	0.0E+00
15	1.2E+10	4.6E+07	3.9E+04	3.4E+07	8.2E+07
30	1.2E+10	9.2E+07	3.9E+04	6.8E+07	1.6E+08
45	1.2E+10	1.4E+08	3.9E+04	1.0E+08	2.5E+08
60	1.2E+10	1.8E+08	3.9E+04	1.4E+08	3.3E+08
120	1.2E+10	3.7E+08	3.9E+04	2.7E+08	6.5E+08
180	1.2E+10	5.5E+08	3.9E+04	4.1E+08	9.8E+08

The regional activity results calculated for the air permeable fabric using the penetration model illustrate several of the same trends as outlined by the first principles model for the air impermeable fabric. In this regard, the values of A_o and $A_{outersuit}$ were equivalent for each of the fabrics as evidenced by comparing the respective columns of Table 19 and Table 24. This was expected as the same C_o values and deposition velocities were used in both models and the magnitudes of the outer volume and outer sleeve surface areas were very similar for each fabric. Additionally, for both fabrics, the regional activity results show that the lowest activity and, thus fewest particulates, existed in the inner volume region between the PPE sleeve and forearm. That being said, A_i for the modelling cases in which the PPE sleeve was composed of the air permeable fabric was several orders of magnitude greater than those cases involving the air impermeable fabric. Correspondingly, $A_{innersuit}$ and A_{skin} were much greater for the air permeable PPE sleeve. This is significant as it illustrates that the air impermeable fabric, assuming a closure leak rate consistent with a Class 2 NFPA 1994 protection requirement, does a much better job of preventing particulates from gaining access to the inner confines of the PPE sleeve than the air permeable fabric, which has zero closure leakage. From a radiation protection standpoint, it is important to limit the number of particulates within the PPE sleeve as, once the particulates are inside, the sleeve can no longer attenuate any of the incident radiation and it becomes possible for the particulates to enter the body via open wounds. Additionally, because exposure decreases with the square of separation distance, it is desirable to maximize the separation distance between the radioactive particulates and the forearm tissue. Finally, the outputs of the respective models further indicate that steady state conditions for A_i are achieved almost instantaneously for both the air permeable and air impermeable fabrics. Recall, for the air impermeable fabric, this is due to the fact that the particulates deposit on the inner surface of the PPE sleeve and skin much more quickly than they are able to leak into the inner confines of the sleeve, while, in the case of the air permeable fabric, it is the result of only a short period of time being required for the particulates to penetrate through the fabric itself.

7.1.3. No shielding cases

As outlined in Section 6.2.3, for the modelling cases in which no PPE sleeve was used to protect the forearm, fundamental particle transport theory was used to determine the regional concentration values for each of the three radionuclide species. As a result of the absence of the PPE sleeve, it was only necessary to determine the concentration of radioactive particulates in the outer volume surrounding the forearm and on the surface of the forearm itself. As with the first principles and penetration models, the outer concentration values for each radionuclide were obtained from the literature and are presented in Table 16. Using these values and the skin deposition velocities listed in Table 12, it was possible to calculate the concentration of particulates on the surface of the forearm using

Equation 35. The resulting regional concentration values for the modelling case involving no PPE sleeve and the Co-60 particulates are presented in Table 27. Similar tables were produced for the modelling cases involving Sr-90 and Cs-137 and are included in Appendix I.

Table 27: Regional concentration values generated using fundamental particulate transport theory for the case in which no PPE sleeve was used to protect the forearm from exposure to Co-60 particulates

Time / min	$C_o / \text{Bq m}^{-3}$	$C_{skin} / \text{Bq m}^{-2}$
0	1.5E+06	0.0E+00
15	1.5E+06	1.6E+07
30	1.5E+06	3.3E+07
45	1.5E+06	4.9E+07
60	1.5E+06	6.6E+07
120	1.5E+06	1.3E+08
180	1.5E+06	2.0E+08

Again, the regional concentration results were scaled according to the magnitude of the outer volume and surface area of the forearm in order to determine the total activity of the particulates within each region. These values are listed in Table 28 and vary slightly from those used to scale the first principles and penetration models due to the absence of the PPE sleeve.

Table 28: Magnitudes of each of the outer volume and forearm surface area given the absence of a PPE sleeve

Region	Area or Volume
Outer volume	$942.6 \times 10^5 \text{ cm}^3$
Surface area of a forearm	754.0 cm^2

Table 29, Table 30, and Table 31 present the regional activity values for the modelling cases involving no PPE sleeve and exposure to Co-60, Sr-90, and Cs-137 particulates, respectively. These values were subsequently integrated with those of the dosimetric model in order to determine the dose imparted to the forearm tissue for the three modelling cases in which no PPE sleeve was used for protection.

Table 29: Regional activity values for the modelling case in which PPE sleeve was used to protect the forearm from exposure to Co-60 particulates

Time / min	A_o / Bq	A_{skin} / Bq
0	1.4E+08	0.0E+00
15	1.4E+08	1.2E+06
30	1.4E+08	2.5E+06
45	1.4E+08	3.7E+06
60	1.4E+08	5.0E+06
120	1.4E+08	9.9E+06
180	1.4E+08	1.5E+07

Table 30: Regional activity values for the modelling case in which no PPE sleeve was used to protect the forearm from exposure to Sr-90 particulates

Time / min	A_o / Bq	A_{skin} / Bq
0	1.4E+10	0.0E+00
15	1.4E+10	1.2E+08
30	1.4E+10	2.5E+08
45	1.4E+10	3.7E+08
60	1.4E+10	5.0E+08
120	1.4E+10	9.9E+08
180	1.4E+10	1.5E+09

Table 31: Regional activity values for the modelling case in which no PPE sleeve was used to protect the forearm from exposure to Cs-137 particulates

Time / min	A_o / Bq	A_{skin} / Bq
0	1.2E+10	0.0E+00
15	1.2E+10	1.1E+08
30	1.2E+10	2.1E+08
45	1.2E+10	3.2E+08
60	1.2E+10	4.3E+08
120	1.2E+10	8.6E+08
180	1.2E+10	1.3E+09

Comparing the regional activity values for the modelling cases in which the PPE sleeve was absent with those generated by either the first principles or penetration models does not produce any surprising results. Firstly, A_o was consistent across each of the particulate transport models for the three radionuclides as defined by the model inputs. That being said, the absence of the PPE fabric meant that the outer volume region encompassed the outer sleeve, inner sleeve, and inner volume regions as defined in both the first principles and penetration model. Thus, although each of the particulate transport models produced consistent results with regards to the number of particulates located in the outer volume region, these particulates were significantly closer to the forearm for the modelling cases involving no PPE sleeve. This, as discussed previously, will have a detrimental effect on the dose imparted to the forearm tissue. Secondly, the value of A_{skin} for the modelling cases involving no PPE sleeve was only marginally greater in magnitude relative to those in which the sleeve was composed of the air permeable fabric for each of the three radionuclide species analyzed. The reason for this is that the C_o for the modelling cases in which no PPE sleeve was used (Table 27) is slightly larger than the C_i for those cases in which the air permeable fabric was used (Table 22). This trend serves to further indicate that the air permeable fabric as modelled is not particularly effective at preventing particulates from gaining access to the inner confines of the PPE sleeve, which is consistent with the relatively high penetration efficiency value.

7.2. Dosimetric Model

As discussed in Section 6.3, the MCNP5 code was used to develop the dosimetric model such that the dose imparted to the forearm tissue could be determined for each set of exposure conditions outlined in the nine modelling cases. When constructing the dosimetric model, it was decided to use separate input files to model the five source locations (surface of the forearm, inner air gap, inner surface of the PPE sleeve, outer surface of the PPE sleeve, and outer environment), as this made it possible to assess the contribution to the overall dose provided by the radioactive particulates in each individual region. Additionally, because the MCNP5 code is only able to generate one type of source particle at a time, it was necessary to create two input files for the modelling cases involving Co-60 and Cs-137 as these radionuclides emit both gamma and beta radiation when decaying (Table 15). Developing the model in this manner was of further benefit as it enabled the level of protection offered by the selected PPE fabrics against both gamma and beta radiation to be assessed and allowed for an analysis of which has a greater impact on the total overall dose imparted to the forearm. Hence, it was possible to not only determine the dose imparted to the forearm as a result of exposure to various radioactive particulate species, but also to investigate the level of protection offered by the various types of PPE fabrics against both gamma and beta radiation as a function of source location and to determine the contribution of

each type of radiation to the total overall dose. It is important to recall that the output of the dosimetric model is expressed in terms of a dose per source particle (in this case, source particles refer to the gamma photons and beta particles produced during the decay of the respective radioactive particulate species) and, at this stage, does not take into account regional concentration variations. As the outputs of the dosimetric model were in terms of a dose per source particle, it was possible to compare the radiological protection capabilities of each fabric relative to the no shielding case as a result of exposure to each of the three radionuclides selected for analysis.

7.2.1. Co-60 and Cs-137 modelling cases

As a result of their similar decay schemes, the dosimetric model outputs for the modelling cases involving Co-60 and Cs-137 showed similar trends, differing only in terms of the magnitude of the imparted dose. This difference can be attributed to the difference in energy of the respective gamma photons and beta particles emitted during the decay of Co-60 and Cs-137 (Table 15). As such, for the dosimetric model outputs, it was decided to present in detail only those results relating to Co-60 exposure for initial discussion. The dosimetric model results for the modelling cases involving Cs-137 have been included for reference in Appendix J.

Figure 31 illustrates the overall dose imparted to the forearm as a function of source location for the three PPE sleeve concepts (second generation CRC fabric, CBRN fabric, and no shielding) when exposed to Co-60 particulates. Error bars have been included, but are too small to be seen given the scale of the y-axis. As outlined in Section 6.3, for the modelling cases in which no PPE sleeve was used to protect the forearm, it was only necessary to define source locations on the surface of the forearm and in the surrounding outer environment; moreover, in these cases, the outer volume was defined so as to encompass the regions previously defined as outer sleeve, inner sleeve, and inner volume. Thus, the outer volume region was larger for the modelling cases in which the PPE sleeve was absent as compared to when it was present. As a result, it is not correct to directly compare the dose imparted to forearm as a function of source location for the cases in which no PPE sleeve was used with those in which it was composed of either the second generation CRC fabric or CBRN fabric, as the source particle density within each of the regions is not equivalent. In order to overcome this problem, an additional MCNP5 model was developed in which the region normally defined as one of the two PPE fabrics was filled with air; otherwise, the model was fully consistent with those developed to analyze the second generation CRC and CBRN fabrics and ensures a consistent source particle density in each of the source location regions. It must be stressed that the results generated for the model in which the PPE sleeve was replaced with air are included solely to provide a basis against which to

compare the protection capabilities of each of the fabrics and are not used in the analysis of any of the nine modelling cases.

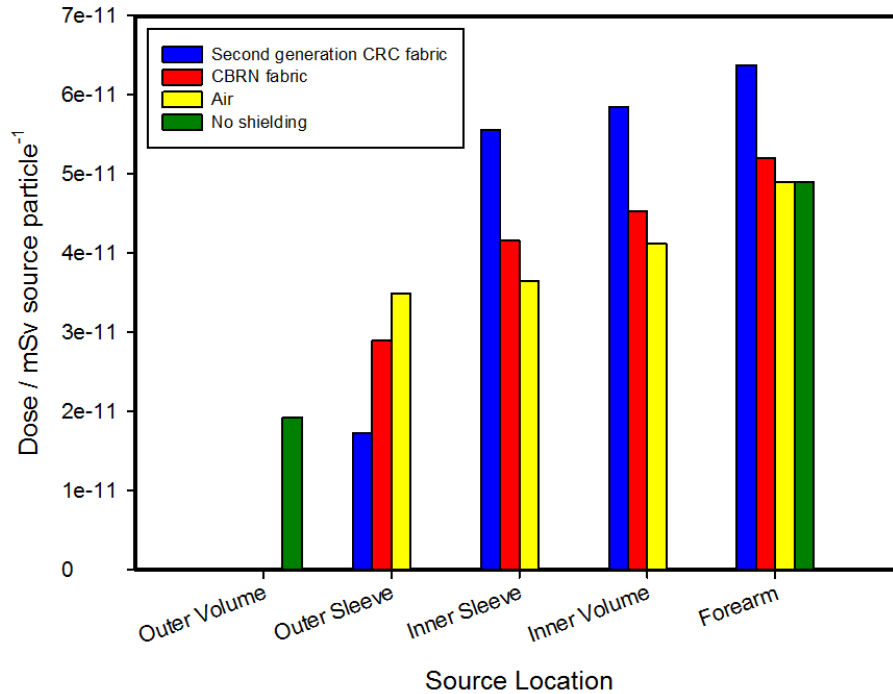


Figure 31: Overall dose (gamma and beta) imparted to forearm as a function of source location for each of the PPE sleeve compositions when exposed to Co-60 particulates

For each of the PPE sleeve concepts, the modelling results show that on a per source particle basis the regions closest to the forearm would contribute a greater percentage to the overall dose than those located further away. More simply put, the Co-60 particulates located on the surface of the forearm would impart the highest dose to the forearm tissue, while those from the outer volume region would contribute the least. This trend is to be expected as exposure is inversely proportional to the square of distance. It is surprising that very little of the total imparted dose stems from the Co-60 particulates located in the outer volume region; however, this can be explained by recalling that the dosimetric model output is averaged on a per source particle basis. In this regard, given the size of the outer volume, the likelihood that a gamma photon or beta particle from this region is incident on the forearm is very small. The reason for this is due to the fact that as the distance between the source particle and forearm increases, the angle

subtended by these two entities decreases. Thus, if the vast majority of source particles from the outer volume region are not incident on the forearm, then they do not impart any dose and taking their average in order to determine the mean dose results in a very small value. This trend is further supported by the results of the no shielding case. Recall that, in this case, the outer volume region extends all the way to the forearm; as such, on average, the source particles originating in the outer volume region will be much closer to the forearm. As a result, a greater dose was imparted to the forearm from the outer volume region for the case in which no shielding was used compared those in which a PPE sleeve was present.

Another surprising trend illustrated in Figure 31 is that the forearm tissue would receive a greater overall dose when surrounded by a PPE sleeve composed of either fabric compared to when it was surrounded by air. This is counterintuitive, but indicates that both the second generation CRC and CBRN fabrics reflected a significant amount of the radiation emitted from within the confines of the PPE sleeve back to the forearm tissue. In essence, radiation that was originally moving away from the forearm was reflected by the PPE sleeve back in the opposite direction. As a result, significantly more radiation was imparted to the forearm tissue as opposed to when no fabric was present. Additionally, the dose contributed by the reflected radiation exceeded that which originated outside of the PPE sleeve and was attenuated by the fabrics. This explains why, even though the fabrics were able to attenuate some of the radiation emitted from outside the confines of the PPE sleeve, the total dose was greater for the modelling cases in which they were present. This has important ramifications from a radiation protection standpoint as depending on the relative activities of the particulates in each region, the use of a PPE sleeve may actually contribute a greater dose to the forearm than it prevents. This will be examined in Section 7.3 when the regional activity concentration results of the particulate transport model are integrated with those of the dosimetric model for each of the nine modelling cases.

Figure 32 and Figure 33 illustrate the contribution to the overall dose provided by the gamma and beta radiation, respectively, as determined by the dosimetric model. Again, error bars have been included for each figure, but are too small to be viewed. With regards to Figure 32, the gamma-contributed dose imparted to the forearm tissue was equivalent regardless of the composition of the PPE sleeve. This indicates that neither the second generation CRC fabric nor the CBRN fabric was able to attenuate a significant portion of the incident gamma photons. These findings are consistent with the published results from the transmittance experimentation (Section 5.2), which showed that the second generation CRC fabric was only effective at attenuating low energy gamma photons (< 300 keV).

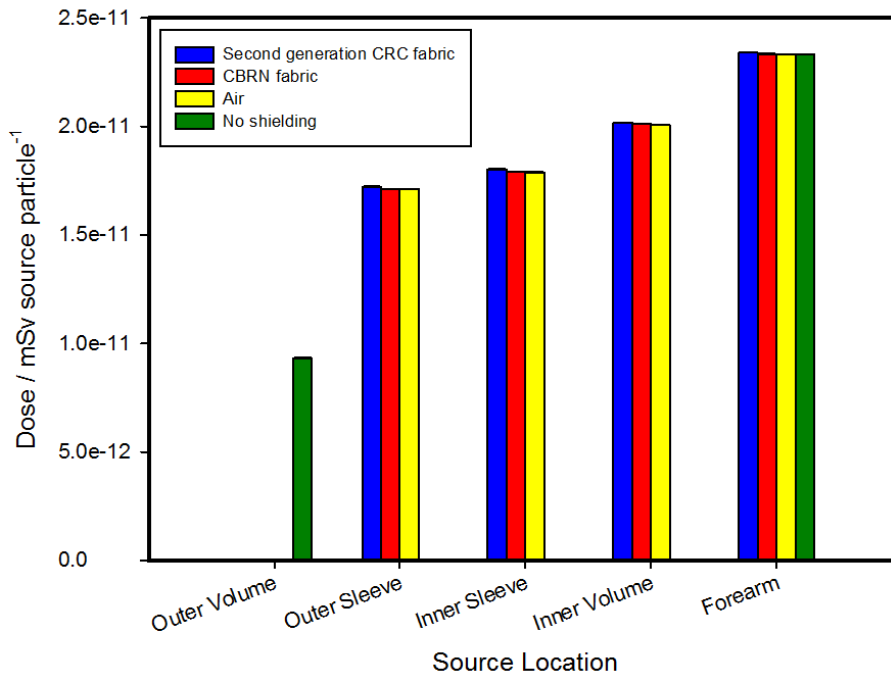


Figure 32: Gamma-contributed dose imparted to forearm as a function of source location for each of the PPE sleeve compositions when exposed to Co-60 particulates

The dosimetric model results from Figure 33 illustrate that the beta-contributed dose was greatest when the PPE sleeve was composed of the second generation CRC fabric and least when the forearm was surrounded by air. As discussed above, the reason for this is that the PPE sleeves reflected the beta radiation that was originally moving away from the forearm back in the opposite direction such that it was incident on the forearm. Further evidence of this phenomenon is seen in that the dose imparted to the forearm tissue from the outer volume and outer sleeve regions was very low for the cases in which the sleeve was composed of one of the fabrics. In fact, when the PPE sleeve was composed of the second generation CRC fabric, almost all of the beta radiation was attenuated. In this instance, as the radiation originated outside of the sleeve, it was absorbed or reflected away from the forearm as opposed to towards it. The reason this phenomenon was not observed for the gamma radiation was because neither of the fabrics was able to attenuate the gamma photons, meaning that they simply passed through the each of the PPE sleeve fabrics and were not reflected back in the direction of the forearm.

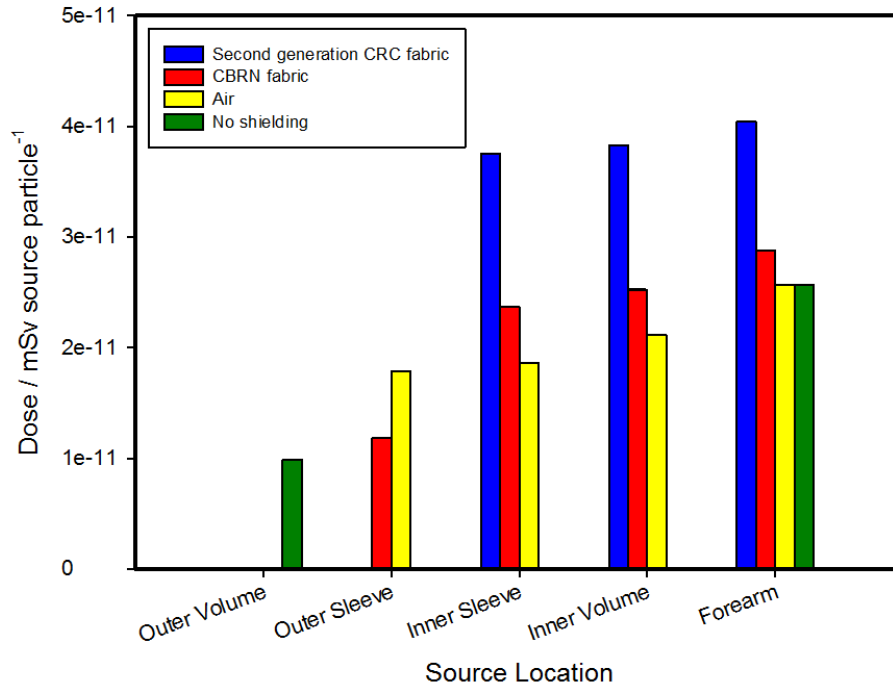


Figure 33: Beta-contributed dose imparted to forearm as a function of source location for each of the PPE sleeve compositions when exposed to Co-60 particulates

Comparing Figure 32 and Figure 33 for the three PPE sleeve compositions, it is evident that the gamma and beta radiation each contributed roughly 45 % and 55 %, respectively, of the total dose imparted to the forearm tissue for the modelling cases involving exposure to Co-60 particulates. The ratio of the gamma-contributed dose to the beta-contributed dose changed drastically for the modelling cases involving Cs-137 as the latter contributed nearly ten times as much to the overall dose as the former, regardless of PPE sleeve composition. These results are presented in Appendix J. The disparity between the ratios of the gamma-contributed dose to the beta-contributed dose for Co-60 and Cs-137 can be attributed to the fact that the energies of the respective gamma photons and beta particles emitted during the decay of Co-60 and Cs-137 are different. As presented in Table 15, Co-60 (1.173 MeV and 1.332 MeV) emits gamma photons of significantly higher energy than those released during the decay of Cs-137 (0.662 MeV); however, this is reversed when comparing the energies of the beta particles produced by each radionuclide (0.318 MeV for Co-60 and 0.514 MeV or 1.176 MeV for Cs-137). In this regard, the dosimetric model results are in agreement with those anticipated from theory.

The ability of the PPE sleeve to protect the forearm from incident radiation, be it gamma or beta, is largely related to its mass attenuation coefficient. For a given material, mass attenuation coefficient varies as a function of both the type and energy of the incident radiation [1]. In this manner, a material can have a drastically different mass attenuation spectrum for each type of radiation; that being said, regardless of the type of radiation, mass attenuation coefficient decreases as the energy of the incident radiation increases. The reason for this, as outlined in Section 2.1, is that mass attenuation coefficient is a reflection of the probability that incident radiation undergoes some sort of nuclear interaction when passing through or contacting a material [1]. Using this definition, it follows that it is desirable to use materials with high mass attenuation coefficients for radiation protection purposes as the inclusion of these materials results in more nuclear interaction events which, in turn, corresponds to a reduction and alteration in the energy and direction of the incident radiation, respectively. Of the two fabrics, the second generation CRC fabric has a higher mass attenuation coefficient than the CBRN fabric due to the addition of nanoparticles of bismuth and tungsten to its composition (Section 2.2). The inclusion of these radio-opaque metals explains why the PPE sleeve was able to attenuate a greater percentage of the incident beta radiation when it was composed of the second generation CRC fabric relative to the CBRN fabric. Unfortunately, at high gamma photon energies, the mass attenuation coefficient of each fabric is very low [14]. Correspondingly, neither fabric was able to attenuate a significant quantity of the incident gamma photons when exposed to the Co-60 or Cs-137 particulates. Again, this analysis is on a per source particle basis and does not reflect the regional activity values associated with each fabric.

7.2.2. Sr-90 modelling cases

The results generated using the dosimetric model for those cases involving exposure to Sr-90 particulates are illustrated in Figure 34. Error bars have been included, but are too small to be seen on the graph. These results are consistent with the beta-contributed dose results obtained for the modelling cases involving Co-60 (Figure 33) and Cs-137 (Figure A.16); moreover, this is to be expected as Sr-90 emits only beta radiation when undergoing radioactive decay. In this regard, the fact that a greater dose was imparted to the forearm tissue for the modelling cases in which the PPE sleeve, composed of either fabric, was present can be explained by the sleeve's propensity to reflect outgoing radiation back to the forearm as discussed in Section 7.2.1. Additionally, as for the cases involving Co-60 and Cs-137, the second generation CRC fabric was able to attenuate almost all of the beta radiation originating outside of the PPE sleeve. This is evidenced by the fact that the dose imparted to the forearm tissue from the outer volume and outer sleeve regions on a per source particle basis is very low. Unfortunately, the protection offered by the sleeve against the external radiation was exceeded by the

additional dose received from the reflected internal radiation. Again, this explains why the dose per source particle imparted to the forearm was greatest for the modelling cases in which the PPE sleeve was present, even though the fabrics were able to attenuate some of the beta radiation emitted from outside the confines of the PPE sleeve.

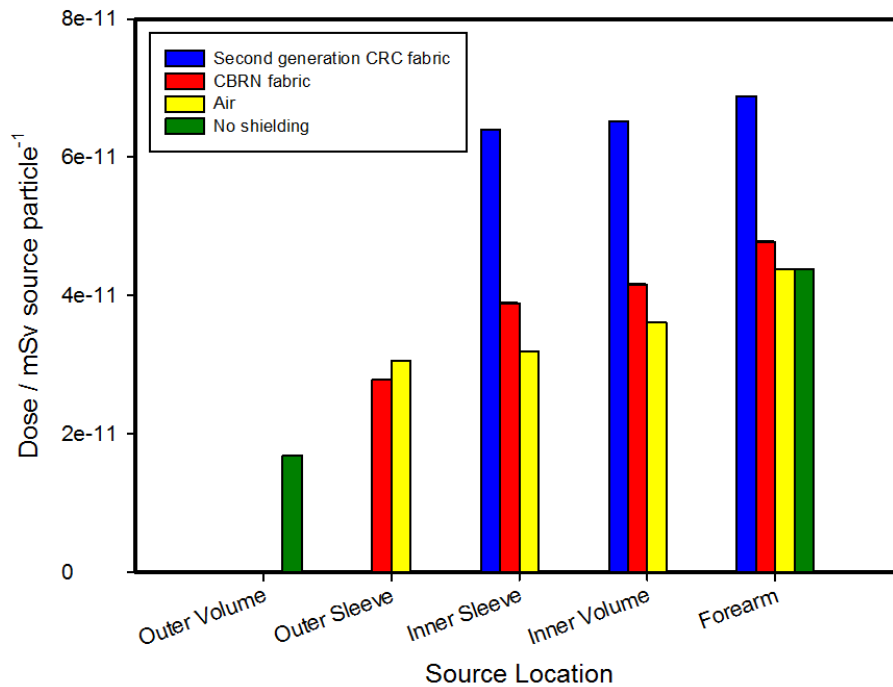


Figure 34: Overall dose imparted to forearm as a function of source location for each of the PPE sleeve compositions when exposed to Sr-90 particulates

7.3. Analysis of the Nine Modelling Cases

The aim of developing the nine modelling cases was to determine the dose imparted to the human forearm as a result of exposure to aerosolized radioactive particulates released in a dispersion event. It was desired that these cases be representative of the most likely set of conditions facing first responders and military personnel during a radiological dispersion event. As such, an analysis of the dose imparted to the forearm tissue was carried out for each combination of the three PPE sleeve concepts (second generation CRC fabric, CBRN fabric, or no fabric) and three radionuclide species (Co-60, Sr-90, or Cs-137). A summary of

each combination of exposure parameters making up the nine modelling cases can be referenced in Table 5.

7.3.1. Regional dose rate

In order to determine the dose imparted to the forearm tissue for each of the nine modelling cases, the results of the particulate transport model were integrated with those of the dosimetric model. Recall that the particulate transport model was used to determine the activity of the particulates located at each of the five regions surrounding the sleeved forearm as a function of time, while the dosimetric model was used to determine the dose imparted to the forearm tissue by particulates in each region on a per source particle basis. In this regard, it was possible to scale the regional dosimetric results by the number of particulates undergoing decay per second in each of the respective regions. Because the activity of the particulates was measured in terms of the number of decays occurring per second, when the results of the two models were multiplied, the resulting value became a dose per unit time or dose rate. In this manner, it was possible to determine the dose rate at each of the five regions surrounding the sleeved forearm as a function of time for each of the nine modelling cases. The resulting dose rates are no longer on a per source particle basis, but are representative of the actual number of particulates undergoing radioactive decay per second in each region as determined by the particulate transport model.

Figure 35, Figure 36, and Figure 37 illustrate the results obtained for the modelling cases involving exposure to Co-60 particulates for each of the three PPE sleeve concepts. As the initial input values for the particulate transport models were literature estimates based on a generic radiological dispersion event scenario, a nominal error estimate of $\pm 10\%$ has been applied to the outputs of each of the particulate transport models in order to account for deviations that would arise for different event conditions. The trends presented in the figures are consistent for each of the radionuclide species analyzed. As such, it was decided to base the discussion on the results for the modelling cases involving exposure to Co-60 particulates while those pertaining to the Sr-90 and Cs-137 particulates are included in tabular form in Appendix K.

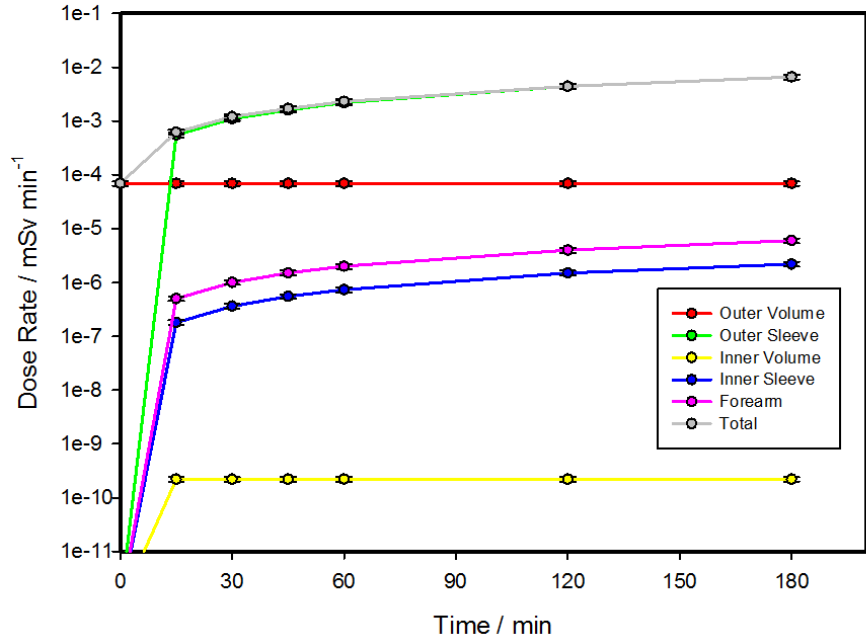


Figure 35: Regional dose rates for the modelling case in which the forearm was surrounded by a PPE sleeve composed of the second generation CRC fabric and exposed to Co-60 particulates

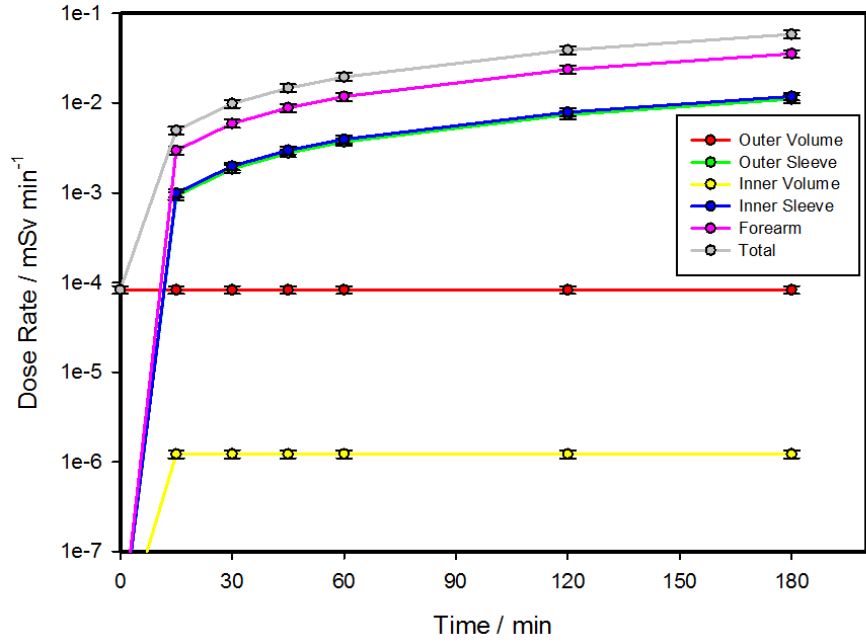


Figure 36: Regional dose rates for the modelling case in which the forearm was surrounded by a PPE sleeve composed of the CBRN fabric and exposed to Co-60 particulates

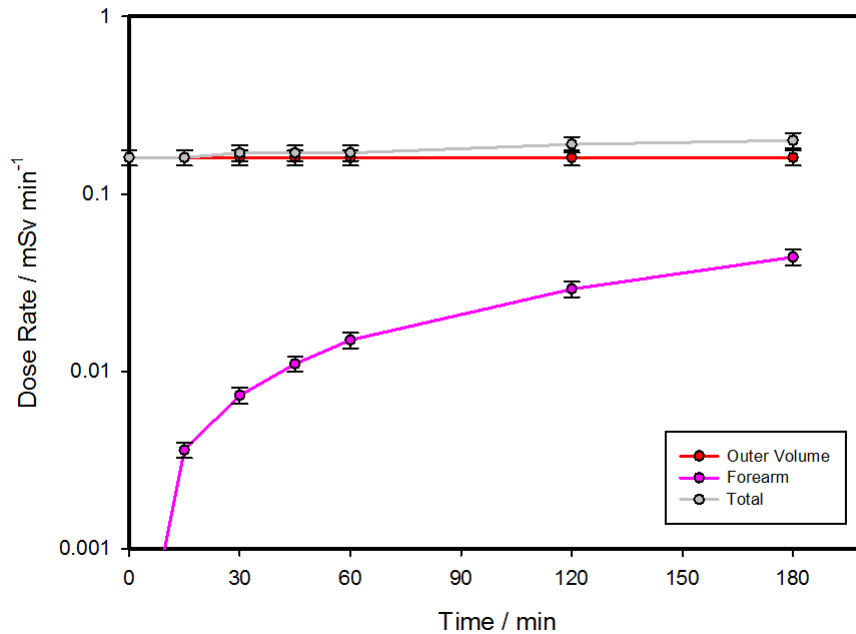


Figure 37: Regional dose rates for the modelling case in which the forearm was not surrounded by a PPE sleeve and was exposed to Co-60 particulates

Figure 35 illustrates that, for the modelling cases involving the second generation CRC fabric, the greatest dose rate is contributed by the particulates that have deposited on the outer surface of the PPE sleeve. In this regard, even though the outer sleeve region contributed a marginally smaller dose on a per source particle basis than the inner sleeve, inner volume, or forearm regions (Figure 31), the fact that there was a significantly higher particulate activity in this region (Table 19) explains why it contributed the greatest dose rate to the forearm tissue. Figure 36 demonstrates that, for the modelling cases in which the PPE sleeve was composed of the CBRN fabric, the greatest dose rate was contributed by the particulates that had deposited on the surface of the forearm. Relative to the second generation CRC fabric (impermeable with a closure leak, Table 19), a significantly higher number of particulates were able to gain access to the inner confines of the PPE sleeve and deposit on the sleeve of the forearm for the modelling cases involving the CBRN fabric (air permeable with a perfect closure, Table 24). This, combined with the fact that the particulates located on the surface of the forearm impart the greatest dose to the forearm on a per source particle basis (Figure 31), explains why the forearm region contributed the greatest dose rate.

It is evident when comparing Figure 35 and Figure 36 that the total dose rate imparted to the forearm tissue is almost an entire magnitude greater when the PPE sleeve is composed of the CBRN fabric, even though it is perfectly sealed, relative to when it is composed of the second generation CRC fabric with a closure leak consistent with a Class 2 NFPA 1994 protection requirement. As the dosimetric model illustrated that the dose imparted to the forearm on a per source particle basis was comparable regardless of which fabric made up the PPE sleeve (Figure 31), it follows that significantly fewer particulates were able to gain access to the inner confines of the PPE sleeve when it was composed of the second generation CRC fabric. In summary, the reason that a smaller dose rate was imparted to the forearm tissue for the modelling cases in which the PPE sleeve was composed of the second generation CRC fabric can be explained by the fact that the leakage of particulates through the impermeable fabric (Table 19) is much lower than the penetration through the air permeable fabric (Table 24). From a radiation protection standpoint, this indicates that it may be preferable to have an impermeable PPE sleeve with a small leak than a permeable one with no leak. Further, the ability of the fabric to limit the number of particulates that gain entry to the inner confines of the PPE sleeve has a greater impact on reducing the dose imparted to the forearm than its ability to attenuate the incident radiation for each of the radionuclide species investigated. Figure 37 illustrates the regional dose rates when the forearm was not surrounded by a PPE sleeve and exposed to Co-60 particulates. In this case, the greatest contribution to the total dose rate came from the outer volume region. As expected, the total dose rate imparted to the forearm was greatest for the modelling case in which no PPE sleeve was present.

It should be noted that the regional dose rate results are somewhat removed from realistic dispersion event conditions due to the assumption that the outer concentration of particulates remained constant, over the time interval investigated, at a value that was reflective of the average concentration after fifteen minutes. In reality, it is more likely that the outer concentration would decrease as a function of time as the plume of dispersed material was transported by meteorological phenomena. In this case, each of the regional dose rates and, subsequently, the total dose rate imparted to the forearm would decrease significantly with time after the initial contact period of fifteen minutes. As such, the results represent a worst-case scenario in which the plume of dispersed radioactive material was stagnant for an extended period of time.

7.3.2. Nine modelling cases

Having determined the regional dose rates as a function of time for the nine modelling cases, it was then possible to integrate these values in order to calculate the dose imparted to the forearm tissue in each case. To do this, the five regional dose rate values were first summed in order to determine the total dose rate. The

total dose rate was then plotted as a function of time for each of the nine modelling cases. A regression analysis was applied to each plot using the SigmaPlot software (Systat Software, Version 11.0, November 2008) and the resulting equation was subsequently integrated in order to determine the total dose imparted to the forearm tissue as a function of time [53]. Figure 38 illustrates the total dose rate plot and regression equation for the modelling case in which the forearm was surrounded by a PPE sleeve composed of the second generation CRC fabric and exposed to Co-60 particulates. The corresponding regression equations for the remaining eight modelling cases are included in Appendix L.

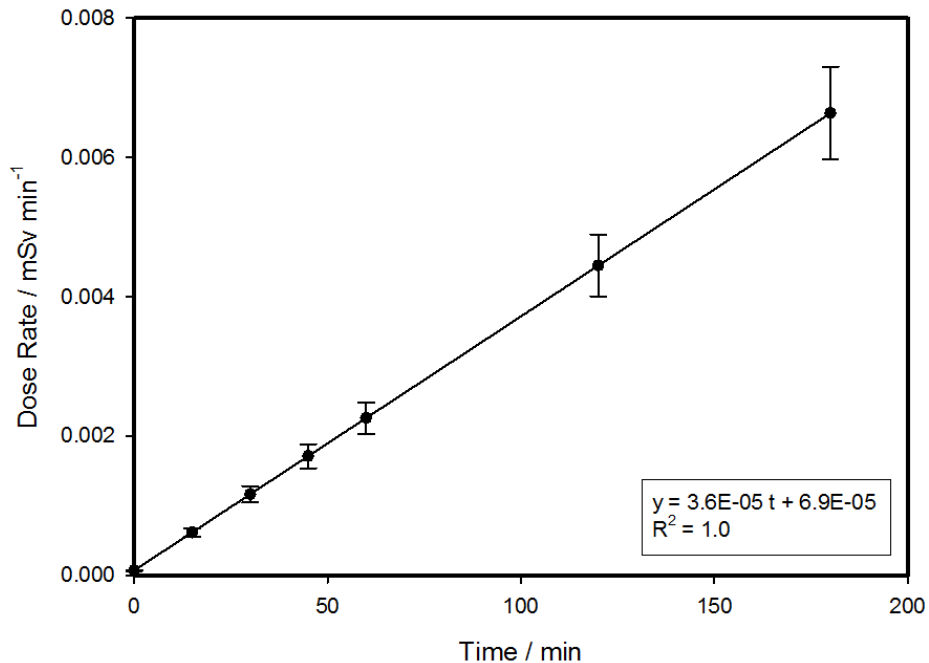


Figure 38: Total dose rate plot and regression equation for the modelling case in which the forearm was surrounded by a PPE sleeve composed of the second generation CRC fabric and exposed to Co-60 particulates

Table 32, Table 33, and Table 34 present the total dose imparted to the forearm tissue as a function of time for each of the modelling cases. For ease of analysis, the results have been separated into three tables according to the radionuclide species to which the forearm was exposed. The results are also presented in graphical form in Figure 39, Figure 40, and Figure 41, respectively.

Table 32: Total dose imparted to the forearm tissue as a function of time for the modelling cases involving exposure to Co-60 particulates

Time / min	Dose / mSv		
	Second Generation CRC Fabric	CBRN Fabric	No Shielding
0	0.0E+00	0.0E+00	0.0E+00
15	5.1E-03	3.5E-02	2.4E+00
30	1.8E-02	1.4E-01	4.9E+00
45	4.0E-02	3.1E-01	7.4E+00
60	7.0E-02	5.4E-01	9.9E+00
120	2.7E-01	2.2E+00	2.1E+01
180	6.0E-01	4.9E+00	3.2E+01

Table 33: Total dose imparted to the forearm tissue as a function of time for the modelling cases involving exposure to Sr-90 particulates

Time / min	Dose / mSv		
	Second Generation CRC Fabric	CBRN Fabric	No Shielding
0	0.0E+00	0.0E+00	0.0E+00
15	1.9E-03	3.7E+00	2.1E+02
30	7.2E-03	1.5E+01	4.3E+02
45	1.6E-02	3.3E+01	6.5E+02
60	2.8E-02	5.8E+01	8.8E+02
120	1.1E-01	2.3E+02	1.8E+03
180	2.5E-01	5.2E+02	2.9E+03

Table 34: Total dose imparted to the forearm tissue as a function of time for the modelling cases involving exposure to Cs-137 particulates

Time / min	Dose / mSv		
	Second Generation CRC Fabric	CBRN Fabric	No Shielding
0	0.0E+00	0.0E+00	0.0E+00
15	1.4E-01	4.2E+00	2.6E+02
30	5.0E-01	1.7E+01	5.3E+02
45	1.1E+00	3.7E+01	8.0E+02
60	1.9E+00	6.6E+01	1.1E+03
120	7.4E+00	2.6E+02	2.3E+03
180	1.7E+01	5.9E+02	3.5E+03

It is important to remember that one cannot compare the results of the modelling cases for one radionuclide with those of another radionuclide. The reason for this is due to the fact that each of the radionuclide species had a different initial outer volume activity concentration (Table 16). Thus, it is misleading to compare the Co-60, Sr-90, and Cs-137 cases above and conclude that a dispersion event involving exposure to Cs-137 particulates is more dangerous than one involving exposure to Co-60 particulates, except inasmuch as the activities of the applied dispersion event scenarios may have been realistic. That being said, it is possible to identify and compare trends present within the results of the nine modelling cases. In this regard, the above results indicate that, for each radionuclide species, the forearm tissue received the lowest dose when it was surrounded by the PPE sleeve composed of the second generation CRC fabric and the highest dose when no sleeve was present. This indicates that, compared to the other PPE sleeve concepts, the fact that the second generation CRC fabric was significantly better at limiting the number of radioactive particulates that gained entry to the inner confines of the PPE sleeve (Section 7.1) exceeded the fact it also resulted in a marginally higher dose being imparted to the forearm on a per source particle basis (Section 7.2) due its propensity to reflect internal radiation back to forearm. This trend is most noticeable for the cases involving exposure to Sr-90 particulates as shown in Table 33. The reason for this is that the second generation CRC fabric not only prevented the particulates from entering the PPE sleeve, but also attenuated the majority of the beta radiation originating outside of the PPE sleeve. As a result, the dose imparted to the forearm was several orders of magnitude less, instead of just one, when the PPE sleeve was composed of the second generation fabric relative to when it was composed of the CBRN fabric or not present. Thus, it can be concluded that given current radiation attenuation technologies, the ability of the fabric to limit the transport of radioactive particulates has a greater impact on reducing the dose imparted to the forearm than its ability to attenuate the incident radiation and that low particulate leakage through closures consistent with a Class 2 NFPA 1994 protection requirement is a significant contributor to protection.

It is not strictly correct to compare the results of the nine modelling cases with the acceptable exposure limits outlined by the ICRP because those guidelines pertain to a whole-body dose as opposed to a forearm dose. That being said, doing so clearly illustrates the extreme hazard that certain types of radiological dispersion events may pose to emergency personnel and military personnel depending on their choice of protective suits, which can have drastically different closure quality and fabric properties. Recall that, as a worst-case scenario, the ICRP recommends that no individual receive a whole-body dose exceeding 50 mSv over a time period of one year [9]. As presented in Figure 39 below, the results for the modelling cases involving exposure to Co-60 particulates compare favourably with this value regardless of sleeve concept; moreover, even for the case in which no sleeve was

present, the forearm only received a dose of 32 mSv. For the modelling cases involving exposure to Sr-90 or Cs-137 particulates (Figure 40 and Figure 41), only the second generation CRC fabric sleeve concept offered significant protection as the forearm received a dose greater than 50 mSv in just over one hour when surrounded by the CBRN fabric. Furthermore, for these radionuclides, less than fifteen minutes was required for the forearm to exceed the advised maximum acceptable dose when no PPE sleeve was present. Again, it should be noted that the values presented in the figures below correspond only to the dose imparted to the forearm and not the whole body. In this regard, it is expected that the corresponding whole-body dose would be much higher for each of the nine modelling cases, further illustrating the limitations of current PPE fabrics and styles; this expectation is worthy of further examination in a future work.

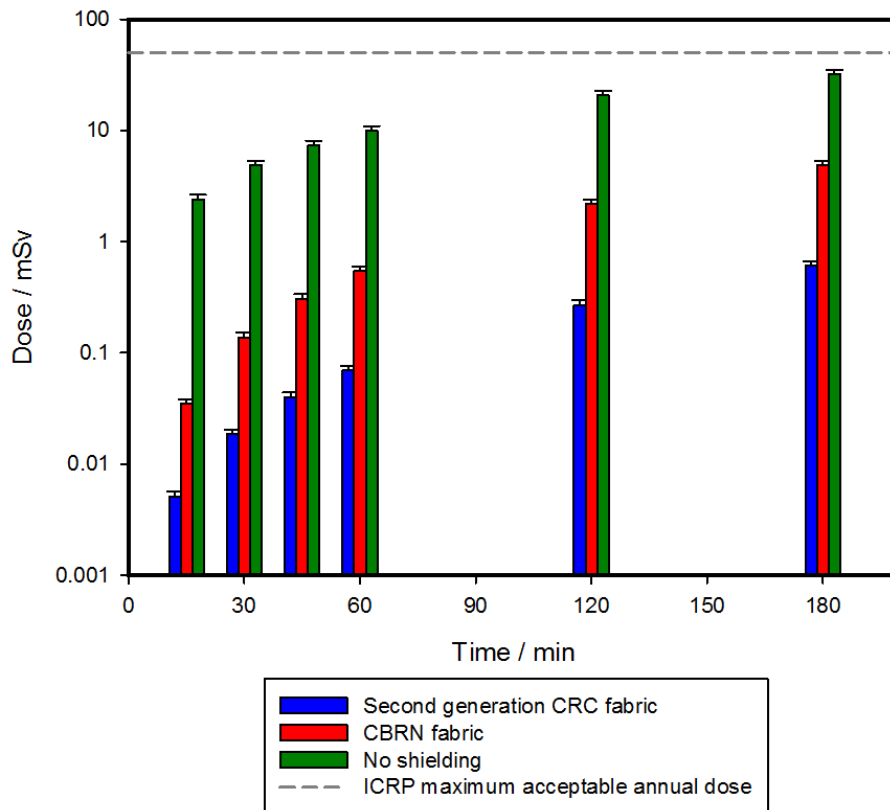


Figure 39: Comparison of the total dose imparted to the forearm tissue as a function of time for the modelling cases involving exposure to Co-60 particulates and the ICRP maximum acceptable whole-body annual dose

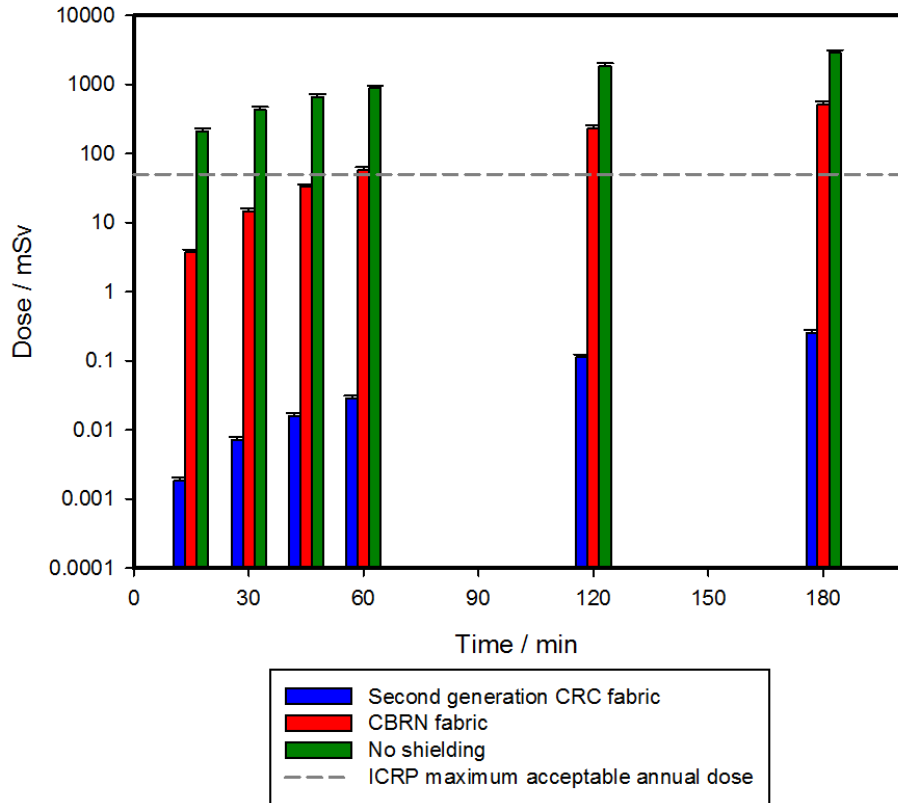


Figure 40: Comparison of the total dose imparted to the forearm tissue as a function of time for the modelling cases involving exposure to Sr-90 particulates and the ICRP maximum acceptable whole-body annual dose

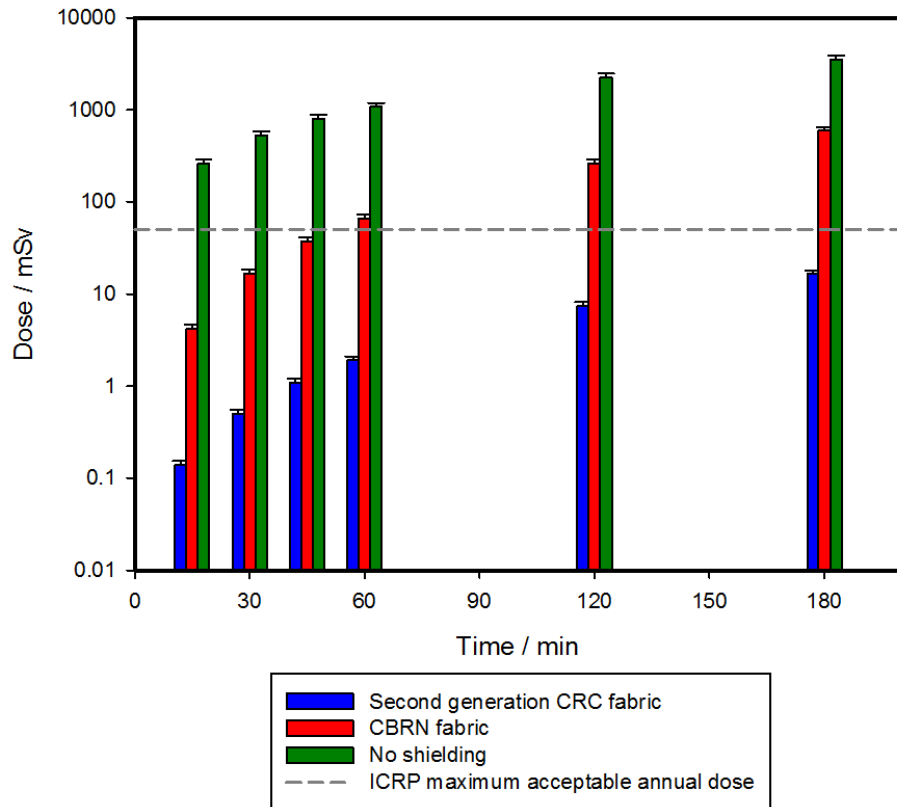


Figure 41: Comparison of the total dose imparted to the forearm tissue as a function of time for the modelling cases involving exposure to Cs-137 particulates and the ICRP maximum acceptable whole-body annual dose

8. RECOMMENDATIONS FOR FUTURE WORK

The particulate transport and dosimetric models developed as part of this thesis can be improved and advanced through additional research. In this regard, a number of areas have been identified for further consideration in future works.

As used here, the particulate transport models rely heavily on a number of key assumptions and, thus, are limited in terms of the situations to which they can be applied. In both cases, as the initial input values were literature estimates based on a generic radiological dispersion event, the outputs reflect these conditions. As such, it may be of interest to analyze the performance of the models against additional realistic, time-varying scenarios that include meteorological conditions in more detail. Furthermore, it is recommended that the finite element modelling be continued as part of any future particulate transport work. This could be performed using either the COMSOL Multiphysics software with a different module or an alternative CFD platform better equipped to simulate particulate transport phenomenon. As the particulate transport experimentation and initial COMSOL model illustrated, it is essential that the improved particulate transport model include a better mechanism for describing the convective motion of particulates within a moving fluid. Additionally, it would be prudent to incorporate surface deposition and gravitational settling effects and include a resuspension factor within the model to account for particulates that are deposited and then re-aerosolized. COMSOL has recently released a new module, entitled '*Particle Tracing*', which has numerous new features pertaining to particulate transport phenomenon [54]. It is recommended that this module be thoroughly investigated as a possible candidate for use in developing the improved particulate transport model in any future work. Any future particulate transport model would also need to be successfully validated against corresponding benchmarking experimentation.

In terms of the dosimetric model, future work could assess the contributions of other types of radiation to the overall dose imparted to the forearm. In this regard, alpha particles and neutrons could be investigated and the attenuation capabilities of various PPE fabrics against these types of radiation analyzed. While the MCNP5 code is not capable of simulating the transport of alpha particles or the secondary particles produced as a result of their interaction with matter, the newly released MCNP6 code includes the required data tables [55]. Further, it may be of interest to re-run the input files of the MCNP5-based dosimetric model using MCNP6 in order to see the variation, if any, between the results generated by the two codes.

Finally, the long-term goals of this research are to develop a model that CAF commanders can reference in order to determine the dose their personnel would receive in response to radiological dispersion events of varying exposure

conditions and to understand how the design specifications of protective systems can affect received dose. As such, there is a significant amount of work that needs to be completed in order to advance this project from its current state to the desired end state. Most notably, future works must seek to extend both the particulate transport and dosimetric models to be representative of a whole-body protected by an entire PPE suit as opposed to a forearm surrounded by a PPE sleeve. Additionally, while the nine modelling cases give a good representation of the most likely exposure conditions facing first responders and emergency personnel during a dispersion event, the scope of the project needs to be broadened to include other types of PPE suits and radionuclides species. The preliminary model developed in this thesis indicates that, given the current state of PPE fabrics, the ability of the fabric to limit the transport of radioactive particulates has a greater impact on reducing the imparted dose than its ability to attenuate the incident radiation and that particulate leakage through closures consistent with a Class 2 NFPA 1994 protection requirement is not a significant contribution to dose. This same conclusion might not be true for the often worn single-use coverall where closures are usually much less effective. In this regard, unless there is a significant breakthrough in the design of and materials used in PPE fabrics, future work should focus on those PPE suits that are impermeable and have effective closures. To complete the project, the integration and performance of various respirators in tandem with the PPE suits should be investigated, both experimentally and using computer simulation. This would allow for the effects of inhaled radiation to be considered and for the total dose imparted to the body, protected by both a PPE suit and respirator, to be determined as a result of exposure to various radiological dispersion event conditions.

9. CONCLUSION

This thesis has contributed valuable insight into the level of protection afforded by current PPE materials when exposed to the radiological conditions present during a dispersion event. A two-fold modelling approach was successfully employed to determine the dose imparted to a human forearm, surrounded by a PPE sleeve, in response to nine different cases that were representative of a combination of the three most likely radionuclide species facing emergency personnel during a radiological dispersion event and three different PPE sleeve concepts.

The following summarizes the conclusions obtained from the particulate transport models:

- The particulate transport models were used to predict the activity concentration of radioactive particulates in five regions surrounding the sleeved forearm for each of the nine modelling cases.
- The results indicate that, for each radionuclide species in its specific dispersion event scenario, the air impermeable fabric with a small closure leak allowed significantly fewer particulates to gain access to the inner confines of the PPE sleeve than the air permeable fabric with no closure leak, while the case in which no PPE sleeve was used resulted in the greatest number of radioactive particulates depositing on the surface of the forearm.

The following summarizes the conclusions obtained from the dosimetric model:

- The MCNP5 code was successfully benchmarked against the gamma photon transmittance experimentation. This was completed as part of a published work [14] and illustrates that the MCNP5 model is able to account for the generation and transport of secondary particles and can accurately simulate real-world, radiological processes.
- The dosimetric model was successfully used to determine the dose imparted to the forearm tissue for each of the nine modelling cases.
- The results generated by the model show, that on a per source particle basis, the regions closest to the forearm contributed a greater percentage to the overall dose than those located further away for each of the nine modelling cases.

- Additionally, the model outputs indicated that, on a per source particle basis, the most dose was imparted to the forearm when it was surrounded by a PPE sleeve composed of the second generation CRC fabric and the least when no sleeve was present.
- The dosimetric model also enabled the contribution by gamma and beta radiation to the overall dose imparted to the forearm tissue to be determined for the modelling cases involving Co-60 and Cs-137. The results illustrate that the ratio of the gamma-contributed dose to the beta-contributed dose is in accordance with their respective decay schemes.

The following summarizes the conclusions obtained by integrating the particulate transport and dosimetric models:

- Integrating the particulate transport and dosimetric models illustrates that, for each radionuclide species, the forearm tissue received the lowest dose when it was surrounded by the second generation CRC fabric and the most dose when no sleeve was present.
- The integrated model indicates that the ability of the fabric to limit the transport of radioactive particulates has a greater impact on reducing the imparted dose than its ability to attenuate incident radiation when comparing an air permeable sleeve with no closure leakage to an air impermeable sleeve consistent with a Class 2 NFPA 1994 protection requirement.
- Comparing the results of the nine modelling cases with the maximum acceptable whole-body dose as put forth by the ICRP is favourable for the modelling cases involving exposure to Co-60 particulates regardless of the PPE sleeve concept; however, for the modelling cases involving exposure to Sr-90 or Cs-137 particulates, only the second generation CRC fabric sleeve concept offered significant protection.

The preliminary model developed in this thesis was able to determine the dose imparted to a human forearm as a result of exposure to radioactive particulates released in a dispersion event, but requires additional work such that it may be extended to consider more accurately particulate infiltration processes and whole-body dose and be used as a tool for CAF commanders during radiological emergencies.

10. REFERENCES

- [1] Glasstone, S. and A. Sesonske. *Nuclear Reactor Engineering*. 3. New York: Van Nostrand Reinhold Company, 1981.
- [2] Corcoran, E.C. *CCE 511: Health Physics and Radiation Protection – Course Notes*. Kingston: Royal Military College of Canada, 2012.
- [3] Bonin, H.W. *Health Physics and Radiation Protection*. RMC-CCE-HWB-90-1. Kingston: Royal Military College of Canada, 1990.
- [4] Lamarsh, J.R. and A.J. Baratta. *Introduction to Nuclear Engineering*. 3. New Jersey: Prentice Hall, 2001.
- [5] Friedlander, G., J.W. Kennedy, E.S. Macias, and J.M. Miller. *Nuclear and Radiochemistry*. 3. Toronto: John Wiley & Sons, Inc., 1981.
- [6] Hall, E.J. *Radiobiology for the Radiologist*. 4. Philadelphia: J.B. Lippincott Company, 1994.
- [7] Bevelacqua, J. *Basic Health Physics*. New York: John Wiley & Sons, Inc., 1999.
- [8] Annals of the ICRP. "2005 Recommendations of the International Commission on Radiological Protection." New York: Elsevier, 2006.
- [9] Annals of the ICRP. "1990 Recommendations of the International Commission on Radiological Protection." New York: Pergamon Press, 1991.
- [10] Military Agency for Standardization. "Commander's guide on low level radiation (LLR) exposure in military operations." Brussels: North Atlantic Treaty Organization, 2000.
- [11] Horton, R. and W. Forest. "Investigation of Demron fabric as a radiation attenuator." Kingston: Royal Military College of Canada, 2012.
- [12] Director Soldier Systems Program Management. "Specification for cloth, chemical warfare (CW) protective, double layer (DSSPM 2-2-80-227)." Canadian Forces, 2003.
- [13] Corcoran, E.C., W. Forest, R. Horton, D.G. Kelly, K. Mattson, C. McDonald, K.S. Nielsen, K. Topping, R.D. Weir, and A. Yonkeu. "A performance

study of radio-opaque personal protective fabrics for the reduction of transmittance of gamma-rays and neutrons." *Journal of Radioanalytical and Nuclear Chemistry* (2012): 251-256.

- [14] Roeterink, M.J., D.G. Kelly, E.G. Dickson, M.T. Andrews, and E.C. Corcoran. "Analysis and Monte Carlo modelling of radio-opaque personal protective fabrics." *Journal of Radioanalytical and Nuclear Chemistry* (2014): 1131-1139.
- [15] DeMeo, R., J. Kucherovsky, and A. Kurupathi. "Radiation detectable and protective articles (patent application number: 20050211930)." Ft. Lauderdale: Meridian Research and Development, 2005.
- [16] Canadian Standards Association and Canadian General Standards Board. "Protection of first responders from chemical, biological, radiological, and nuclear (CBRN) events (CAN/CGSB/CSA-Z1610-11)." Standards Council of Canada, 2011.
- [17] Hinds, W.C. *Aerosol Technology: Properties, Behavior, and Measurement of Airborne Particles*. 2. New York: John Wiley & Sons, Inc., 1999.
- [18] Vincent, J.H. *Aerosol Sampling: Science, Standards, Instrumentation and Applications*. West Sussex: John Wiley & Sons, Inc., 2007.
- [19] Baron, P.A. and K. Willeke. *Aerosol Measurement: Principles, Techniques, and Applications*. 2. Hoboken, NJ: John Wiley & Sons, Inc., 2005.
- [20] Fogh, C.L., M.A. Byrne, K.G. Andersson, K.F. Bell, J. Roed, A.J.H. Goddard, D.V. Vollmair, and S.A.M. Hotchkiss. "Quantitative measurement of aerosol deposition on skin, hair and clothing for dosimetric assessment – final report." Roskilde: Risø National Laboratory, 1999.
- [21] Andersson, K.G., J. Roed, M.A. Byrne, H. Hession, P. Clark, E. Elahi, A. Byskov, X.L. Hou, H. Prip, S.K. Olsen, and T. Roed. "Airborne contamination in the indoor environment and its implications for dose." Roskilde, Risø National Laboratory, 2004.
- [22] Sehmel, G.A. "Particle and gas dry deposition: a review." *Atmospheric Environment* (1980): 983-1011.

- [23] Jamriska, M. "Aerosol penetration through protective fabrics." Fisherman's Bend, Victoria: Australian Department of Defence, Human Protection and Performance Division, 2009.
- [24] Benitez, J. *Principles and Modern Applications of Mass Transfer Operations*. 2. New York: John Wiley & Sons, Inc., 2009.
- [25] Bird, R.B., W.E. Stewart and E.N. Lightfoot. *Transport Phenomena*. 2. New York: John Wiley & Sons, Inc., 2007.
- [26] International Atomic Energy Agency and OECD Nuclear Energy Agency. *The International Nuclear and Radiological Event Scale User's Manual*. Vienna: International Atomic Energy Agency, 2012.
- [27] Edwards, G. "Reactor accidents at Chalk River: the human fallout." 2 July 1998. 25 February 2013. <http://www.ccnr.org/paulson_legacy.html>.
- [28] Kellerer, A.M. "The Southern Urals radiation studies: a reappraisal of the current status." *Radiation and Environmental Biophysics* (2002): 307-316.
- [29] Kuruc, J. and L. Matel. "Thirtieth Anniversary of Reactor Accident in A-1 Nuclear Power Plant Jaslovske Bohunice." *Past and Current Trends in Nuclear Chemistry* (2007): 267-294.
- [30] World Nuclear Association. "Three Mile Island accident." January 2012. 25 February 2013. <<http://www.world-nuclear.org/info/inf36.html>>.
- [31] International Atomic Energy Agency. "Regulatory control of nuclear power plants." 24 February 2013. <<http://www.iaea.org/ns/tutorials/regcontrol/appendix/app96.htm>>.
- [32] McLaughlin, T.P., S.P. Monahan, N.L. Pruvost, V.V. Frolov, B.G. Ryazanov, and V.I. Sviridov. *A Review of Criticality Accidents*. Los Alamos: Los Alamos National Laboratory, 2000.
- [33] Lewis, B.J. *CC523 Nuclear Reactor Engineering: Class Notes*. Kingston: Royal Military College of Canada, 2012.
- [34] Gil, E. "Orphan Sources: Extending Radiological Protection outside the Regulatory Framework." *Second European IRPA Congress on Radiation Protection* (2006): 1-36.

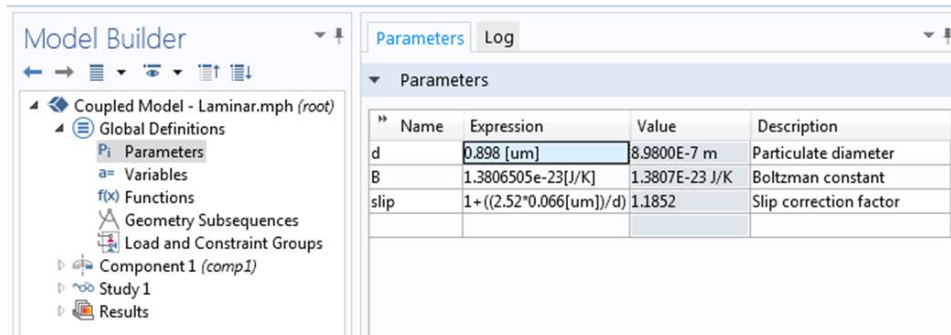
- [35] Nuclear Protection Sub-Group. "Radiological aerosol challenge levels (AC 225/LG/7 D(2006) 0003)." Brussels: North Atlantic Treaty Organization, 2006.
- [36] King, M.M. "Nuclear data sheets update for A = 60." *Nuclear Data Sheets* (1993): 1-67. <<http://atom.kaeri.re.kr/cgi-bin/decay?Co-60%20B->>.
- [37] Federal Emergency Management Agency. "Radiological dispersion device." 12 February 2013. 28 January 2013. <<http://www.ready.gov/radiologicaldispersion-device-rdd>>.
- [38] BBC News. "The Chernobyl disaster." 8 February 2013. <<http://news.bbc.co.uk/2/shared/spl/hi/guides/456900/456957/html/nn3page1.stm>>.
- [39] Tuli, J.K. "Nuclear data sheets for ¹³⁷Ba." *Nuclear Data Sheets* (1997): 579-597. <<http://atom.kaeri.re.kr/cgi-bin/decay?Cs-137%20B->>.
- [40] Browne, E. "Nuclear data sheets for A = 90." *Nuclear Data Sheets* (1997): 379-546. <<http://atom.kaeri.re.kr/cgi-bin/decay?Sr-90%20B->>.
- [41] COMSOL. *COMSOL Multiphysics Reference Manual: Version 4.3b*. COMSOL Software License Agreement, 2013.
- [42] TSI Particle Instruments. "Model 3475 Condensation Monodisperse Aerosol Generator: Instruction Manual." Shoreview, MN: TSI Incorporated, 2004.
- [43] TSI Particle Instruments. "Model 3321 Aerodynamic Particle Sizer[®] Spectrometer: Instruction Manual." St. Paul, MN, MN: TSI Incorporated, 2002.
- [44] X-5 Monte Carlo Team. *MCNP – A General Monte Carlo N-Particle Transport Code, Version 5 Overview and Theory* (LA-UR-03-1987). Los Alamos, NM: Los Alamos National Laboratory, 2008.
- [45] Hubell, J.H. and S.M. Seltzer. *Tables of X-ray Mass Attenuation Coefficients and Mass Energy-Absorption Coefficients*. 1.4. Gaithersburg: National Institute of Science and Technology. June 2013. <<http://physics.nist.gov/xaamdi>>.
- [46] Carrier, R., A. Chamberland, F. Forest, and G. Hachez. "Anthropometric survey of the land forces." North York, ON: Department of National Defence, Defence and Civil Institute of Environmental Medicine, 1998.

- [47] Li, X., Y. Wang, and Y. Lu. “Effects of body postures on clothing air gap in protective clothing.” *Journal of Fiber Bioengineering and Informatics* (2011): 277-283.
- [48] Gudgin Dickson, E., P. Bodurtha, and P. Fedele. “Predicting protection performance behaviour of protective ensembles against airborne contaminants: modeling and measurement.” Bath, UK: Proceedings of the First International Conference on NBC Individual Protective Equipment, 2005.
- [49] National Fire Protection Association. “Standard on protective ensembles for first responders to CBRN terrorism incidents.” Quincy, MA: 2012.
- [50] Duncan, E.J.S., E.F.G. Dickson, P.D. Fedele, and D. Nelson. “A model for prediction of probability of developing an adverse physiological symptom in individuals exposed to VX nerve agent.” *Journal of Medical, Chemical, Biological, and Radiological Defense* (2005).
<http://www.jmedcbr.org/Issue_0301/Dickson/Dickson_0605.html>.
- [51] International Commission on Radiation Units and Measurements. “Photon, electron, proton, and neutron interaction data for body tissue (Report 46).” Bethesda, MD: 1992.
- [52] The Engineering ToolBox. “Air Composition.” August 2014.
<http://www.engineeringtoolbox.com/air-composition-d_212.html>.
- [53] SigmaPlot. *SigmaPlot User’s Guide: Version 11.0*. Systat Software, Inc., 2008.
- [54] COMSOL. “Particle Tracing Module: For Studying the Interaction Between Particles and Fields.” August 2014. < <http://www.comsol.com/particle-tracing-module>>.
- [55] Pelowitz, D.B., ed. *MCNP6TM User’s Manual (LA-CP-13-00634)*. Los Alamos, NM: Los Alamos National Laboratory, 2013.

11. APPENDIX A

Appendix A provides additional detail on the COMSOL model that was benchmarked against the particulate transport experimentation. Further information is presented regarding the global definitions, geometric dimensions, material properties, “Transport of Diluted Species” module, “Laminar Flow” module, and meshing parameters used in the model.

Figure A.1 provides a summary of the parameters that were inputted as global definitions in the COMSOL model. The primary benefit to designating each of these parameters as global definitions was that they could then be used to define other variables included in the model. Additionally, by doing so, any time one of these parameters was altered, all of the model variables dependent on them were automatically updated based on the changes. In this regard, it was possible to quickly and easily manipulate the model to reflect the different particulate sizes measured in each experimental trial.



Name	Expression	Value	Description
d	0.898 [um]	8.9800E-7 m	Particulate diameter
B	1.3806505e-23[J/K]	1.3807E-23 J/K	Boltzman constant
slip	1+((2.52*0.066[um])/d)	1.1852	Slip correction factor

Figure A.1: Summary of the global definitions used in the particulate transport COMSOL model

The COMSOL model geometry and corresponding dimensions of each entity are presented in Figure A.2 and Table A.1, respectively. The geometry was modelled so as to be as representative as possible of the mechanical ‘sleeved forearm’ apparatus, while still being cognisant of the computational requirements needed to solve the model. With this in mind, it was decided to create a 2D axisymmetric model in which the geometry presented in Figure A.2 was revolved about the axial axis prior to being solved as opposed to a more computationally intensive 3D model. Because the apparatus was composed of aluminum, diffusion could not occur through the apparatus boundaries; as such, it was only necessary to model the inner volume of the apparatus and define all of the outer borders, save for the inlet and outlet, as no flux boundaries.

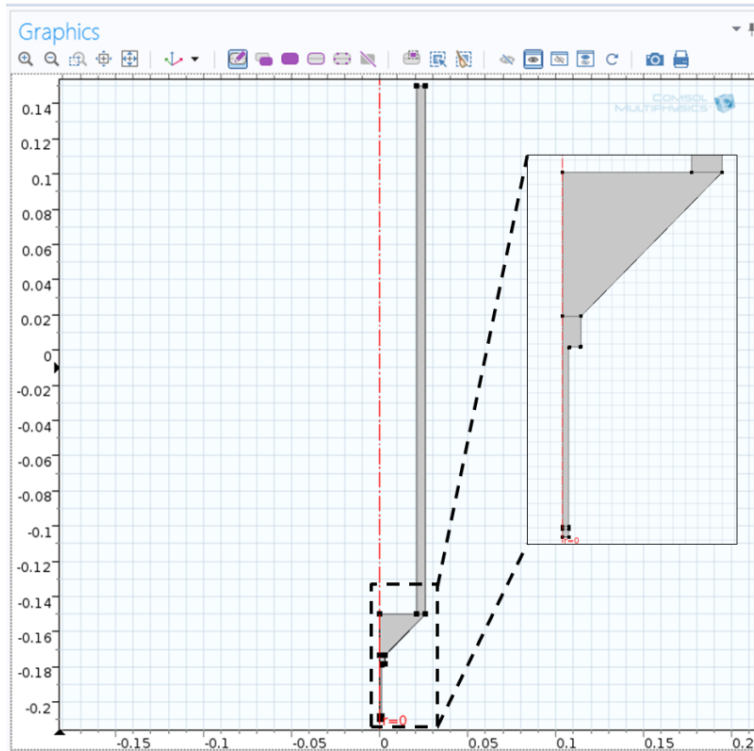


Figure A.2: Particulate transport COMSOL model geometry

Table A.1: Dimensions of each entity making up the model geometry

Domain	Radial Direction Vertices / m	Axial Direction Vertices / m
Rectangle 1	0.021	0.1500
	0.026	0.1500
	0.021	-0.1500
	0.026	-0.1500
Polygon 1	0.000	-0.1500
	0.026	-0.1500
	0.003	-0.1735
	0.000	-0.1735
Polygon 2	0.000	-0.1735
	0.003	-0.1735
	0.003	-0.1785
	0.001	-0.1785
	0.001	-0.2095
0.000	-0.2095	

Due to the manner in which the model was designed, it would have been redundant to model the aluminum components of the apparatus as these components were simply included as no flux boundaries. As a result, the only material to include in the model was the air that filled the inner volume of the apparatus. Figure A.3 presents the material properties for air that were used in the COMSOL model. The majority of these properties were already defined as per the built-in COMSOL material database; however, it was necessary to add additional ones, such as the diffusion coefficient of particulates through air, to the model and define them using the parameters listed as global definitions.

Property	Name	Value	Unit	Property group
Dynamic viscosity	mu	eta(T[1/K])[Pa*s]	Pa*s	Basic
Density	rho	rho(pA[1/Pa], T[1/K])[kg/m^3]	kg/m^3	Basic
Diffusion coefficient	D	(B*T*slip)/(3*pi*d*mu)	m^2/s	Basic
Relative permeability	mur	1	1	Basic
Relative permittivity	epsilonnr	1	1	Basic
Ratio of specific heats	gamma	1.4	1	Basic
Electrical conductivity	sigma	0[S/m]	S/m	Basic
Heat capacity at constant pressure	Cp	Cp(T[1/K])[J/(kg*K)]	J/(kg*K)	Basic
Thermal conductivity	k	k(T[1/K])[W/(m*K)]	W/(m*K)	Basic
Speed of sound	c	cs(T[1/K])[m/s]	m/s	Basic
Refractive index	n	1	1	Refractive index
Refractive index, imaginary part	ki	0	1	Refractive index

Figure A.3: Material properties for air as used in the particulate transport COMSOL model

The built-in system of equations used by COMSOL to describe the laminar flow of an incompressible fluid is presented in Figure A.4. When using the “Laminar Flow” module to solve these equations to describe the flow profile of the air through the apparatus as a function of time, it was first necessary to specify in which domains the physics was occurring, the properties of the fluid, and the initial values of a number of variables. For this model, it was important to solve the velocity profile of the fluid in each of the domains making up the model, whilst the fluid properties were defined in accordance with the selection of the fluid material, in this case air, at standard ambient of temperature and pressure. The initial velocity of the fluid was set to zero and the initial pressure within the volume was deemed to be equal to the reference pressure of 1 atm. It was also necessary to define the wall, inlet, and outlet boundary conditions. In this regard, no slip conditions were applied to each of the wall boundaries. In accordance with the volumetric flowrate of the fluid measured during the experimentation and the dimensions of the apparatus, the inlet velocity was input as 0.00352 m s^{-1} and the pressure at the outlet of the apparatus was set to 0 atm.

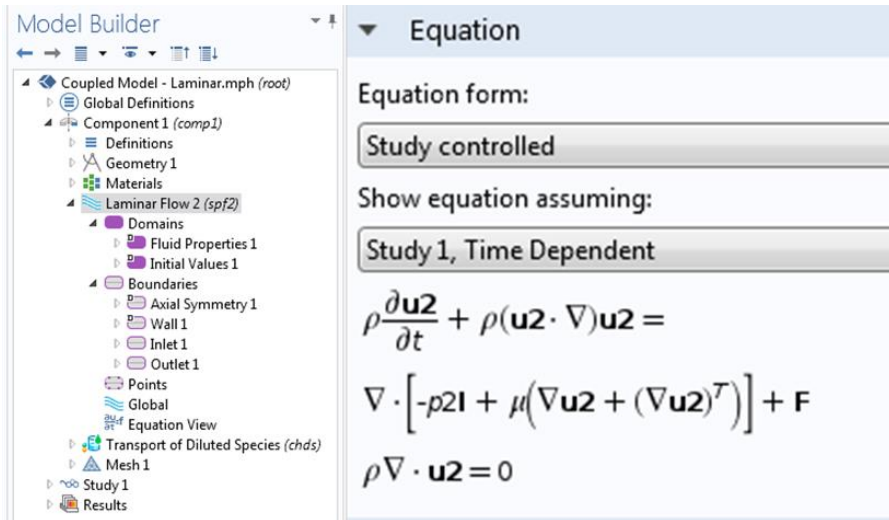


Figure A.4: System of equations used to describe laminar flow of an incompressible fluid by COMSOL

The “Transport of Diluted Species” module was coupled with the “Laminar Flow” module to complete the particulate transport COMSOL model. This module was used to solve the built-in system of equations presented in Figure A.5 in order to determine the concentration of particulates throughout the model geometry as a function of time. To do so, it was necessary to define a number of initial and boundary conditions. For each of the model domains, the initial concentration was equal to zero, while the velocity field was coupled to the solution of the “Laminar Flow” module. The diffusion coefficient of the particulates in air was defined in accordance with the value from the materials properties component of the model. With regards to boundary conditions, the inflow concentration of particulates was defined using a regression equation fitted to the outer concentration results obtained during the benchmarking experimentation. These equations are listed, for each particulate size, in Table A.2. The outflow boundary was located at the opposite end of the model geometry so as to complete the flow of the particulates through the apparatus and into the APS. Finally, as discussed previously, the remaining boundaries were deemed as no flux to reflect the fact that the particulates could not diffuse through the aluminum walls of the mechanical ‘sleeved forearm’ apparatus.

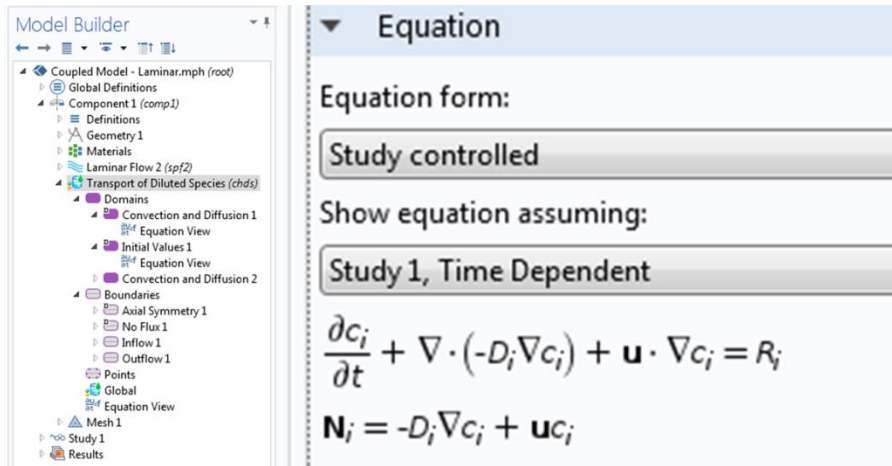


Figure A.5: System of equations used to describe particulate transport by COMSOL

Table A.2: Inflow concentration functions used in the particulate transport COMSOL model

Particulate Size	Inflow concentration expression / particle cm ⁻³
A	$\log(c) = 1.483 - (2.169 \times 10^{-4}) * t [s]$
B	$\log(c) = 1.885 - (3.568 \times 10^{-4}) * t [s]$
C	$\log(c) = 1.683 - (5.572 \times 10^{-4}) * t [s]$

The model geometry was meshed using a combination of quadrilateral and triangular shapes. As shown in Figure A.6, the size and shape of the mesh elements varied with location; however, the aim was to limit computational requirements while still enabling the smaller features of the model geometry to be resolved. Thus, the quadrilateral-shaped mesh elements were confined to a maximum size of 0.0003 m and the triangular-shaped elements to 0.0005 m.

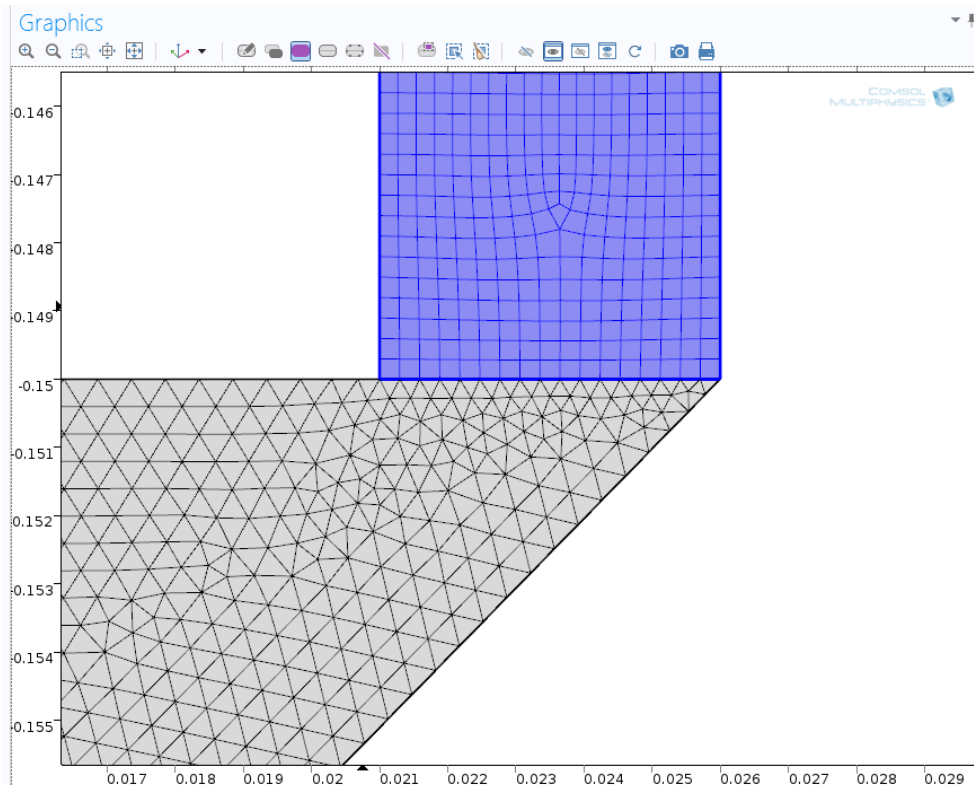


Figure A.6: Illustration of quadrilateral (highlighted) and triangular (grey) mesh elements used in the particulate transport COMSOL model

As outlined in the main body of the thesis, a transient study was used to determine the inner volume concentration and velocity profiles as a function of time. The range was set such that solutions were obtained on 1 s intervals for a period of 360 s and, thus, enabled comparison with the experimentally-obtained results. To solve the compiled system of equations representing both the particulate transport and fluid flow, a fully coupled solution approach, employing a parallel sparse direct solver (PARDISO) with a backward differentiation formula (BDF) time stepping method, was used.

12. APPENDIX B

Appendix B presents the experimentally-obtained results of the particulate transport benchmarking experimentation for the Size B and Size C particulates. In both figures, the error associated with each individual data point was $\pm 5\%$.

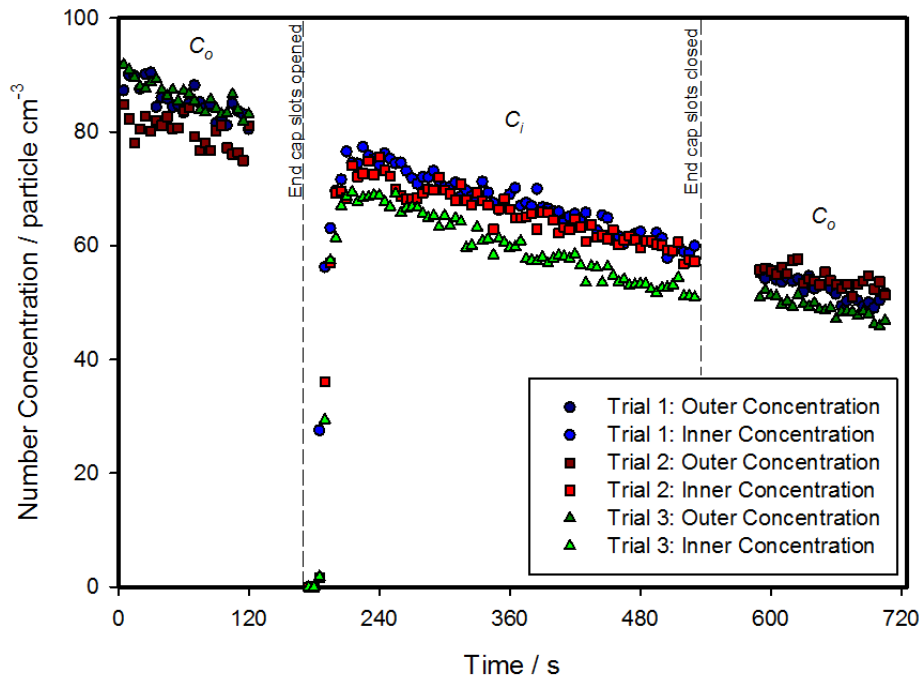


Figure A.7: Experimentally-obtained inner and outer concentration results for the Size B particulates

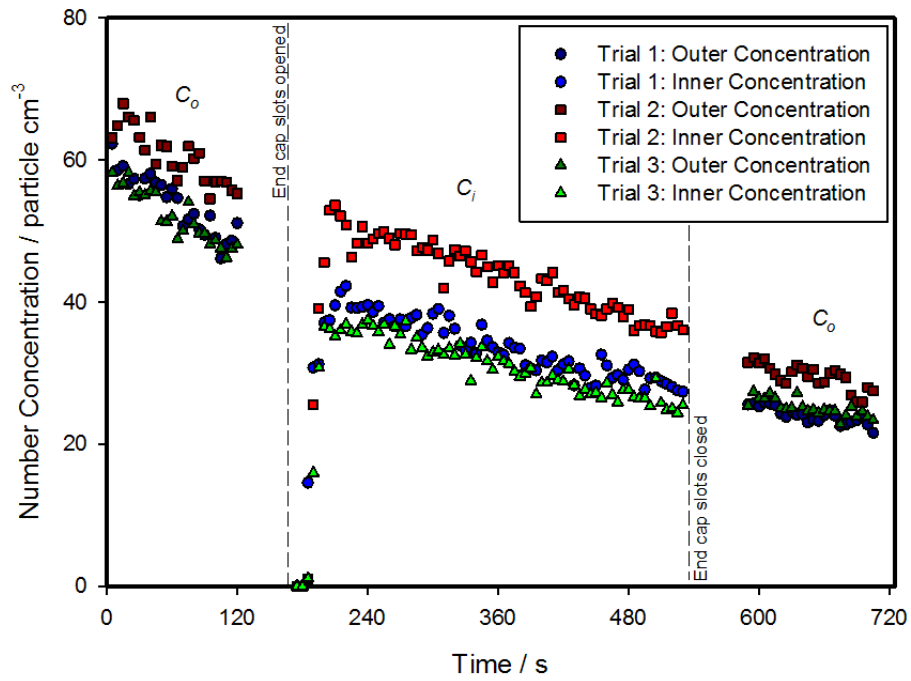


Figure A.8: Experimentally-obtained inner and outer concentration results for the Size C particulates

13. APPENDIX C

Appendix C presents the two-tailed t-test calculations used to confirm that the results of the particulate transport experimentation were statistically significant. The pertinent data are included in Table A.3.

Table A.3: Two-tailed t-test data obtained from the particulate transport experimentation

Particulate Size	Number of Samples (n)	Mean Value (\bar{x})	Standard Deviation (σ)
		log [(particle cm ⁻³) s ⁻¹]	
A	3	2.17 x 10 ⁻⁴	0.05 x 10 ⁻⁴
B	3	3.57 x 10 ⁻⁴	0.02 x 10 ⁻⁴
C	3	5.57 x 10 ⁻⁴	0.05 x 10 ⁻⁴

Comparing Case A and Case B:

$$t_{B-A} = \frac{\bar{x}_B - \bar{x}_A}{\sqrt{\frac{\sigma_B^2}{n_B} + \frac{\sigma_A^2}{n_A}}}$$

$$t_{B-A} = \frac{(3.57 - 2.17) \times 10^{-4}}{\sqrt{\frac{(0.02 \times 10^{-4})^2}{3} + \frac{(0.05 \times 10^{-4})^2}{3}}}$$

$$t_{B-A} = 45.03$$

For a two-tailed t-test with $n - 1$ degrees of freedom and a 95 % confidence interval, $t_{critical} = 4.303$. Therefore, as $t_{B-A} > t_{critical}$, it can be concluded that the means of Size A and Size B are statistically different.

Comparing Case A and Case C:

$$t_{C-A} = \frac{\bar{x}_C - \bar{x}_A}{\sqrt{\frac{\sigma_C^2}{n_C} + \frac{\sigma_A^2}{n_A}}}$$

$$t_{C-A} = \frac{(5.57 - 2.17) \times 10^{-4}}{\sqrt{\frac{(0.05 \times 10^{-4})^2}{3} + \frac{(0.05 \times 10^{-4})^2}{3}}}$$

$$t_{C-A} = 83.28$$

For a two-tailed t-test with $n - 1$ degrees of freedom and a 95 % confidence interval, $t_{critical} = 4.303$. Therefore, as $t_{C-A} > t_{critical}$, it can be concluded that the means of Size A and Size C are statistically different.

Comparing Case B and Case C:

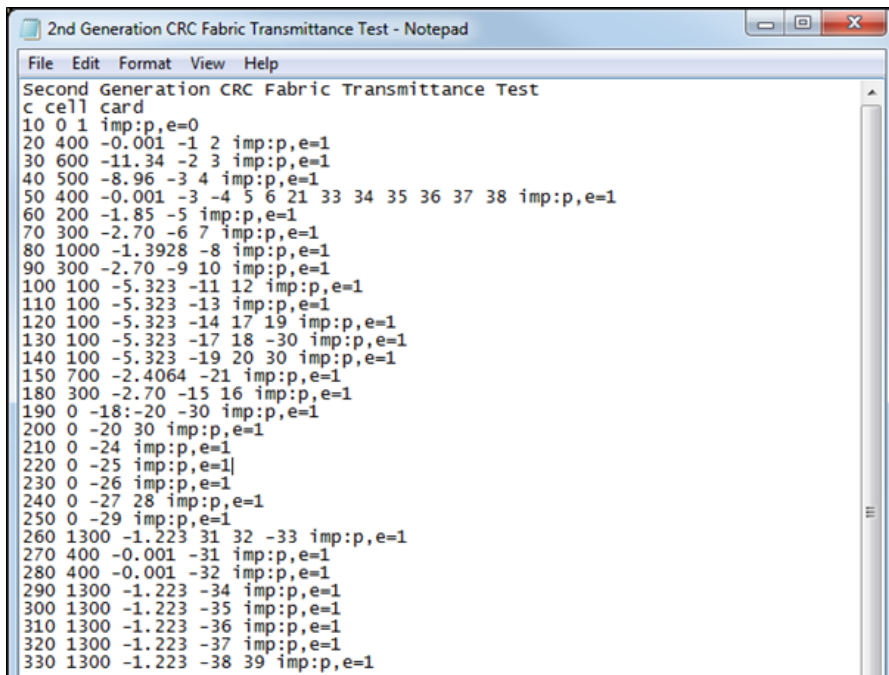
$$t_{C-B} = \frac{\bar{x}_C - \bar{x}_B}{\sqrt{\frac{\sigma_C^2}{n_C} + \frac{\sigma_B^2}{n_B}}}$$
$$t_{C-A} = \frac{(5.57 - 3.57) \times 10^{-4}}{\sqrt{\frac{(0.05 \times 10^{-4})^2}{3} + \frac{(0.02 \times 10^{-4})^2}{3}}}$$
$$t_{C-A} = 64.33$$

For a two-tailed t-test with $n - 1$ degrees of freedom and a 95 % confidence interval, $t_{critical} = 4.303$. Therefore, as $t_{C-B} > t_{critical}$, it can be concluded that the means of Size B and Size C are statistically different.

14. APPENDIX D

Appendix D provides additional detail on the MCNP5 model that was benchmarked against the gamma photon transmittance experimentation. In this regard, further information is presented regarding the content of the cell, surface, and data cards used to construct the input file.

As discussed in the main body of the report, the cell card defines the material content and densities of each of the geometric entities making up the model. As such, it was used to combine the materials listed in the data card with the geometric shapes from the surface card into distinct cells. For example, with reference to Figure A.9, cell 30 corresponds to the volume between the surfaces of the two cylinders used to represent the protective castle from the experimentation; furthermore, the content of this cell is based on the material definition for lead and has a density of 11.34 g cm^{-3} . A similar process was followed to define each of the remaining cells. In this manner, it was possible to define the location and material content of the each of the cells corresponding to the acrylic holder, second generation CRC fabric, surrounding environment, and each component of the high purity germanium detector.



```
2nd Generation CRC Fabric Transmittance Test - Notepad
File Edit Format View Help
Second Generation CRC Fabric Transmittance Test
c cell card
10 0 1 imp:p,e=0
20 400 -0.001 -1 2 imp:p,e=1
30 600 -11.34 -2 3 imp:p,e=1
40 500 -8.96 -3 4 imp:p,e=1
50 400 -0.001 -3 -4 5 6 21 33 34 35 36 37 38 imp:p,e=1
60 200 -1.85 -5 imp:p,e=1
70 300 -2.70 -6 7 imp:p,e=1
80 1000 -1.3928 -8 imp:p,e=1
90 300 -2.70 -9 10 imp:p,e=1
100 100 -5.323 -11 12 imp:p,e=1
110 100 -5.323 -13 imp:p,e=1
120 100 -5.323 -14 17 19 imp:p,e=1
130 100 -5.323 -17 18 -30 imp:p,e=1
140 100 -5.323 -19 20 30 imp:p,e=1
150 700 -2.4064 -21 imp:p,e=1
180 300 -2.70 -15 16 imp:p,e=1
190 0 -18:-20 -30 imp:p,e=1
200 0 -20 30 imp:p,e=1
210 0 -24 imp:p,e=1
220 0 -25 imp:p,e=1
230 0 -26 imp:p,e=1
240 0 -27 28 imp:p,e=1
250 0 -29 imp:p,e=1
260 1300 -1.223 31 32 -33 imp:p,e=1
270 400 -0.001 -31 imp:p,e=1
280 400 -0.001 -32 imp:p,e=1
290 1300 -1.223 -34 imp:p,e=1
300 1300 -1.223 -35 imp:p,e=1
310 1300 -1.223 -36 imp:p,e=1
320 1300 -1.223 -37 imp:p,e=1
330 1300 -1.223 -38 39 imp:p,e=1
```

Figure A.9: Cell card section of the MCNP5 input file used to model the transmittance experimentation

The surface card was used to express each of the different components of the experimental apparatuses as geometric entities suitable for interpretation by the code. In this regard, various shapes, such as planes, spheres, right circular cylinders, and rectangular parallelepipeds, were used to represent the different aspects of the experimental apparatuses. The dimension and location of each geometric entity were defined in accordance with the technical design specifications provided by the manufacturers. The surface card section of the MCNP5 input file used to model the transmittance experimentation is presented in Figure A.10. Figure A.11 illustrates how the MCNP5 code interprets the information contained in the surface card to create the model geometry.

```

c surface card
1 rpp -100 100 -50 150 -100 100 $outter box
2 rcc 0 -9.298 0 0 62.484 0 25.4 $outter Pb
3 rcc 0 -0.2 0 0 40.786 0 14.2 $inner Pb, outter Cu
4 rcc 0 0 0 40.386 0 14.0 $inner Cu, outter air
5 rcc 0 11.95 0 0 0.05 0 3.5 $Be window
6 rcc 0 0 0 11.95 0 3.5 $outter Al lining
7 rcc 0 0 0 11.95 0 3.37 $inner Al lining
8 rcc 0 11.645 0 0 0.005 0 3.07 $aluminized mylar shield
9 rcc 0 2.92 0 0 8.725 0 3.07 $outter mount cup wall
10 rcc 0 2.92 0 0 8.725 0 2.994 $inner mount cup wall
11 rcc 0 4.3 0 0 7.345 0 2.994 $outside contact layer
12 rcc 0 4.3 0 0 7.345 0 2.99397 $inside contact layer
13 rcc 0 11.64497 0 0 0.00003 0 2.99397 $top of contact layer
14 rcc 0 4.3 0 0 7.34497 0 2.99397 $Ge detector
15 rcc 0 2.6 0 0 0.32 0 3.07 $outter mount cup
16 rcc 0 2.6 0 0 0.32 0 0.46 $inner mount cup
17 rcc 0 4.3 0 0 5.26 0 0.53 $outter hole contact layer
18 rcc 0 4.3 0 0 5.26 0 0.46 $inner hole contact layer
19 sph 0 9.56 0 0.53 $outter hole contact layer
20 sph 0 9.56 0 0.46 $inner hole contact layer
21 rcc 0 12 0 0 0.07875 0 3.5 $D2
24 rcc 0 0 0 0 2.6 0 3.37 $void space bottom
25 rcc 0 2.6 0 0 0.32 0 0.46 $void space between cup bases
26 rcc 0 2.92 0 0 1.38 0 2.994 $void space in middle
27 rcc 0 2.6 0 0 9.05 0 3.37 $outter void
28 rcc 0 2.6 0 0 9.05 0 3.07 $inner void
29 rcc 0 11.65 0 0 0.3 0 3.37 $top void
30 py 9.56
31 rcc 0 16.15 0 0 1.0 0 2.45 $hole for the source
32 rcc 0 15.95 0 0 0.2 0 2.25 $ledge for source
33 rpp -5.7 5.7 15.95 17.15 -5.7 5.7 $top rectangular prism
34 rcc -5.1 15.95 -5.1 0 -10.2 0 0.6 $cylindrical support
35 rcc -5.1 15.95 5.1 0 -10.2 0 0.6 $cylindrical support
36 rcc 5.1 15.95 -5.1 0 -10.2 0 0.6 $cylindrical support
37 rcc 5.1 15.95 5.1 0 -10.2 0 0.6 $cylindrical support
38 rpp -5.7 5.7 2.75 5.75 -5.7 5.7 $bottom rectangular prism
39 rcc 0 2.75 0 0 3 0 3.5 $bottom hole for detector

```

Figure A.10: Surface card section of the MCNP5 input file used to model the transmittance experimentation

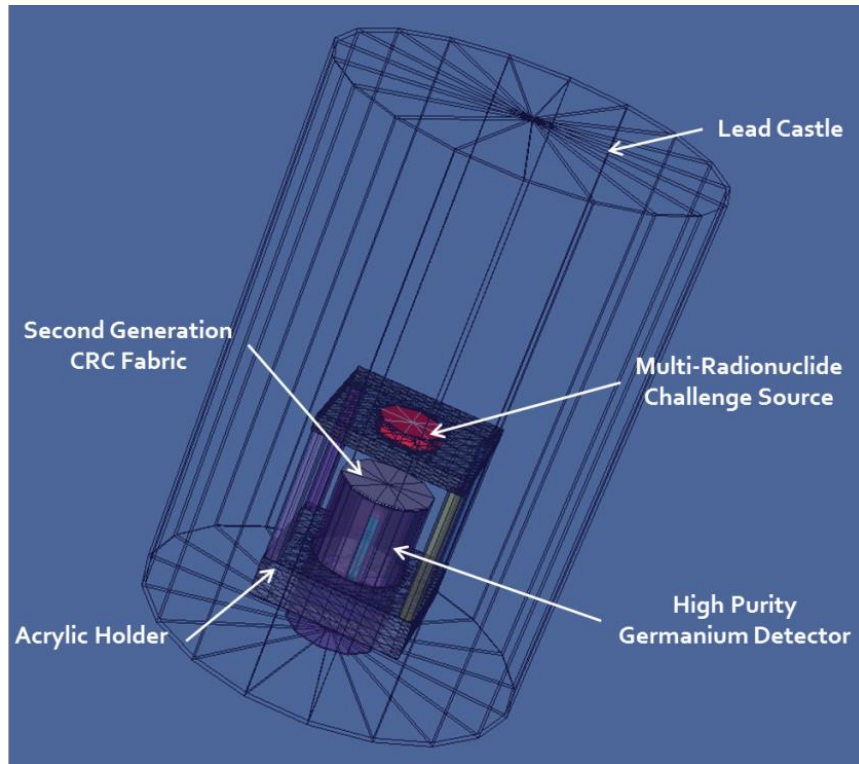


Figure A.11: MCNP5-constructed geometry used to model the transmittance experimentation

The data card was used to define the source, tally type, and materials included in the model. With regard to the source, it was possible to define its position, size, and shape in order to match the experimental set-up to a high degree of accuracy. Additionally, the source was modelled so as to emit gamma photons with energies corresponding to the various radio-nuclides making up the challenge source used during the transmittance testing, while its activity was defined based on the certificate of calibration. To simulate the high purity germanium detector, a pulse height or f8 tally was employed to count the number of pulses within the detector volume; moreover, discrete energy bins were included in the model such that the energy of the incident gamma photons could be determined. The next portion of the card was used to define the elemental composition by mass of the various materials included in the model. The final portion of the data card specifies the number of particles that the program is to run; moreover, in this instance, the code was instructed to analyze the transport of one billion source particles before tallying and outputting the results. This was an important part of variance reduction because by increasing the number of particles run, it was possible to improve the

run statistics and associated relative error. Figure A.12 presents the data card section of the MCNP5 input file used to model the transmittance experimentation.

```
c data card
mode p e
phys:p 20 0 0 0 0
phys:e 20 0 0 0 0 1 1 1 0
sdef pos=0 16.15 0 axs=0 1 0 ext=d1 rad=d2 par=p erg=d3
si1 0 0.828932
sp1 -21 0
si2 0 2.4
sp2 -21 1
si3 1 0.0465 0.0595 0.0880 0.1221 0.1659 0.2792 0.3917 0.514 0.6617 0.8980
      1.1732 1.3325 1.8361
sp3 0.360 0.026 0.390 0.009 0.013 0.028 0.023 0.028 0.011 0.038
      0.018 0.018 0.038
f8:p,e 120
E8 0.057 49i 0.062 0.066 19i 0.068 0.074 9i 0.075 0.077 0.0771 0.0772
      0.0855 49i 0.0905
f18:p 120
E18 0 0.0442 0.0487 0.0571 0.0616 0.0858 0.0903 0.1199 0.1244 0.1637 0.1682
      0.2767 0.2819 0.3891 0.3943 0.5112 0.5170 0.6590 0.6648 0.8950 0.9015
      1.1697 1.1768 1.3288 1.3365 1.8317 1.8401
m100 32000 -1 $Ge detector
m200 4000 -1 $Be window
m300 13000 -1 $Al casing and shielding
m400 6000 -0.00012 $air
      7000 -0.75527
      8000 -0.23178
      20000 -0.01283
m500 29000 -1 $Cu lining
m600 82000 -1 $Pb shielding
m700 8000 -0.02 $second generation CRC fabric
      6000 -0.24
      74000 -0.16
      83000 -0.58
m1000 1000 -0.041959 $approximated Al Mylar
      6000 -0.605017
      8000 -0.303025
      13000 -0.05
c m1100 $Ge with B ions
c m1200 $Ge with Li ions
m1300 1000 4 $Acrylic acid source holder
      6000 3
      8000 2
nps 1000000000j
```

Ln 116, Col 15

Figure A.12: Data card section of the MCNP5 input file used to model the transmittance experimentation

15. APPENDIX E

Appendix E presents the results of the experimental study, used in the development of the penetration model, for the each combination of test parameters. In the this regard, the aerosol penetration efficiency, and accompanying error, calculated for each combination of particulate size, type of PPE fabric, and air face velocity has been included in the below tables.

Table A.4: Aerosol penetration efficiencies for an air face velocity of 5 cm s⁻¹[23]

PPE Fabric	Particulate Size / μm		
	0.03 – 0.3	0.3 – 1.0	1.0 – 3.0
MKIV Over-garment	0.710 \pm 0.018	0.867 \pm 0.031	0.804 \pm 0.066
Black CB suit	0.695 \pm 0.036	0.835 \pm 0.024	0.676 \pm 0.010
Paul Boyé suit	0.760 \pm 0.014	0.867 \pm 0.038	0.688 \pm 0.054

Table A.5: Aerosol penetration efficiencies for an air face velocity of 10 cm s⁻¹[23]

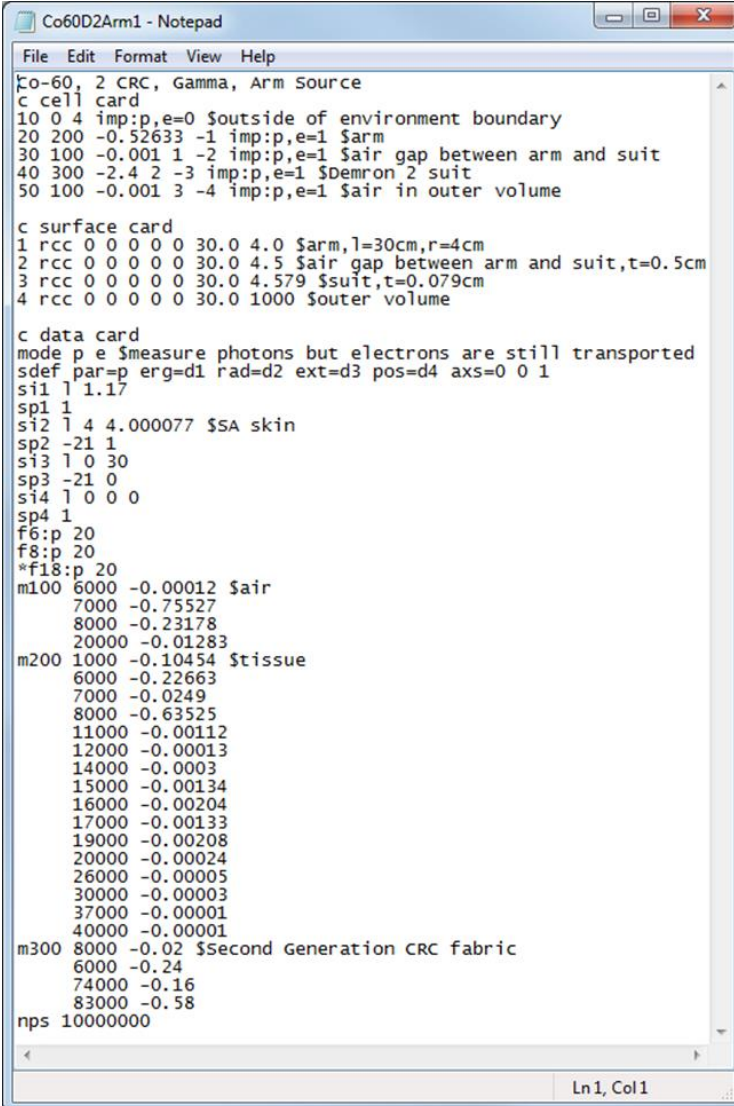
PPE Fabric	Particulate Size / μm		
	0.03 – 0.3	0.3 – 1.0	1.0 – 3.0
MKIV Over-garment	0.775 \pm 0.013	0.895 \pm 0.011	0.666 \pm 0.020
Black CB suit	0.809 \pm 0.009	0.925 \pm 0.007	0.797 \pm 0.008
Paul Boyé suit	0.824 \pm 0.028	0.914 \pm 0.013	0.763 \pm 0.012

Table A.6: Aerosol penetration efficiencies for an air face velocity of 25 cm s⁻¹[23]

PPE Fabric	Particulate Size / μm		
	0.03 – 0.3	0.3 – 1.0	1.0 – 3.0
MKIV Over-garment	0.845 \pm 0.019	0.876 \pm 0.043	0.503 \pm 0.057
Black CB suit	0.875 \pm 0.033	0.934 \pm 0.003	0.636 \pm 0.010
Paul Boyé suit	0.885 \pm 0.032	0.856 \pm 0.028	0.388 \pm 0.077

16. APPENDIX F

Appendix F presents an example of one of the MCNP5 input files used in the dosimetric model. Figure A.13 illustrates the input file used for the modelling case in which the forearm was protected with the second generation CRC fabric against Co-60 particulates, emitting gamma photons, which were located on the surface of the forearm.



```
Co60D2Arm1 - Notepad
File Edit Format View Help
Co-60, 2 CRC, Gamma, Arm Source
c cell card
10 0 4 imp:p,e=0 $outside of environment boundary
20 200 -0.52633 -1 imp:p,e=1 $arm
30 100 -0.001 1 -2 imp:p,e=1 $air gap between arm and suit
40 300 -2.4 2 -3 imp:p,e=1 $Demron 2 suit
50 100 -0.001 3 -4 imp:p,e=1 $air in outer volume

c surface card
1 rcc 0 0 0 0 0 30.0 4.0 $arm,l=30cm,r=4cm
2 rcc 0 0 0 0 0 30.0 4.5 $air gap between arm and suit,t=0.5cm
3 rcc 0 0 0 0 0 30.0 4.579 $suit,t=0.079cm
4 rcc 0 0 0 0 0 30.0 1000 $outer volume

c data card
mode p e $measure photons but electrons are still transported
sdef par=p erg=d1 rad=d2 ext=d3 pos=d4 axs=0 0 1
si1 1 1.17
sp1 1
si2 1 4 4.000077 $SA skin
sp2 -21 1
si3 1 0 30
sp3 -21 0
si4 1 0 0 0
sp4 1
f6:p 20
f8:p 20
*f18:p 20
m100 6000 -0.00012 $air
7000 -0.75527
8000 -0.23178
20000 -0.01283
m200 1000 -0.10454 $tissue
6000 -0.22663
7000 -0.0249
8000 -0.63525
11000 -0.00112
12000 -0.00013
14000 -0.0003
15000 -0.00134
16000 -0.00204
17000 -0.00133
19000 -0.00208
20000 -0.00024
26000 -0.00005
30000 -0.00003
37000 -0.00001
40000 -0.00001
m300 8000 -0.02 $second Generation CRC fabric
6000 -0.24
74000 -0.16
83000 -0.58
nps 10000000
Ln1, Col1
```

Figure A.13: Example of one of the MCNP5 input files used in the dosimetric model

16. APPENDIX G

Appendix G contains the regional concentration values generated by the first principles model for the modelling cases involving the air impermeable fabric and the Sr-90 and Cs-137 particulates. The results are presented as a function of time in the tables below.

Table A.7: Regional concentration values generated by the first principles model for the case in which the air impermeable fabric was exposed to Sr-90 particulates

Time / min	C_o / Bq m^{-3}	$C_{\text{outersuit}}$ / Bq m^{-2}	C_i / Bq m^{-3}	$C_{\text{innersuit}}$ / Bq m^{-2}	C_{skin} / Bq m^{-2}
0	1.5E+08	0.0E+00	0.0E+00	0.0E+00	0.0E+00
15	1.5E+08	6.1E+08	1.5E+04	6.4E+04	1.7E+05
30	1.5E+08	1.2E+09	1.5E+04	1.3E+05	3.5E+05
45	1.5E+08	1.8E+09	1.5E+04	1.9E+05	5.2E+05
60	1.5E+08	2.4E+09	1.5E+04	2.7E+05	6.9E+05
120	1.5E+08	4.9E+09	1.5E+04	5.2E+05	1.4E+06
180	1.5E+08	7.3E+09	1.5E+04	7.7E+05	2.1E+06

Table A.8: Regional concentration values generated by the first principles model for the case in which the air impermeable fabric was exposed to Cs-137 particulates

Time / min	C_o / Bq m^{-3}	$C_{\text{outersuit}}$ / Bq m^{-2}	C_i / Bq m^{-3}	$C_{\text{innersuit}}$ / Bq m^{-2}	C_{skin} / Bq m^{-2}
0	1.3E+08	0.0E+00	0.0E+00	0.0E+00	0.0E+00
15	1.3E+08	5.3E+08	1.3E+04	5.6E+04	1.5E+05
30	1.3E+08	1.1E+09	1.3E+04	1.1E+05	3.0E+05
45	1.3E+08	1.6E+09	1.3E+04	1.7E+05	4.5E+05
60	1.3E+08	2.1E+09	1.3E+04	2.2E+05	6.0E+05
120	1.3E+08	4.2E+09	1.3E+04	4.4E+05	1.2E+06
180	1.3E+08	6.3E+09	1.3E+04	6.7E+05	1.8E+06

17. APPENDIX H

Appendix H contains the regional concentration values generated by the penetration model for the modelling cases involving the air permeable fabric and the Sr-90 and Cs-137 radionuclides. The results are presented for various time increments in the tables below.

Table A.9: Regional concentration values generated by the penetration model for the case in which the air permeable fabric was exposed to Sr-90 particulates

Time / min	C_o / Bq m⁻³	$C_{outersuit}$ / Bq m⁻²	C_i / Bq m⁻³	$C_{innersuit}$ / Bq m⁻²	C_{skin} / Bq m⁻²
0	1.5E+08	0.0E+00	0.0E+00	0.0E+00	0.0E+00
15	1.5E+08	6.1E+08	1.1E+08	4.7E+08	1.3E+09
30	1.5E+08	1.2E+09	1.1E+08	9.3E+08	2.5E+09
45	1.5E+08	1.8E+09	1.1E+08	1.4E+09	3.8E+09
60	1.5E+08	2.4E+09	1.1E+08	1.9E+09	5.0E+09
120	1.5E+08	4.9E+09	1.1E+08	3.7E+09	1.0E+10
180	1.5E+08	7.3E+09	1.1E+08	5.6E+09	1.5E+10

Table A.10: Regional concentration values generated by the penetration model for the case in which the air permeable fabric was exposed to Cs-137 particulates

Time / min	C_o / Bq m⁻³	$C_{outersuit}$ / Bq m⁻²	C_i / Bq m⁻³	$C_{innersuit}$ / Bq m⁻²	C_{skin} / Bq m⁻²
0	1.3E+08	0.0E+00	0.0E+00	0.0E+00	0.0E+00
15	1.3E+08	5.3E+08	9.7E+07	4.0E+08	1.1E+09
30	1.3E+08	1.1E+09	9.7E+07	8.1E+08	2.2E+09
45	1.3E+08	1.6E+09	9.7E+07	1.2E+09	3.3E+09
60	1.3E+08	2.1E+09	9.7E+07	1.6E+09	4.3E+09
120	1.3E+08	4.2E+09	9.7E+07	3.2E+09	8.7E+09
180	1.3E+08	6.3E+09	9.7E+07	4.8E+09	1.3E+10

18. APPENDIX I

Appendix I contains the regional concentration values calculated using fundamental particulate transport theory for the modelling cases involving no PPE sleeve and the Sr-90 and Cs-137 radionuclides. The results are presented for various time increments in the tables below.

Table A.11: Regional concentration values generated using fundamental particulate transport theory for the case in which no PPE sleeve was used to protect the forearm from exposure to Sr-90 particulates

Time / min	$C_o / \text{Bq m}^{-3}$	$C_{skin} / \text{Bq m}^{-2}$
0	1.5E+08	0.0E+00
15	1.5E+08	1.6E+09
30	1.5E+08	3.3E+09
45	1.5E+08	4.9E+09
60	1.5E+08	6.6E+09
120	1.5E+08	1.3E+10
180	1.5E+08	2.0E+10

Table A.12: Regional concentration values generated using fundamental particulate transport theory for the case in which no PPE sleeve was used to protect the forearm from exposure to Cs-137 particulates

Time / min	$C_o / \text{Bq m}^{-3}$	$C_{skin} / \text{Bq m}^{-2}$
0	1.3E+08	0.0E+00
15	1.3E+08	1.4E+09
30	1.3E+08	2.8E+09
45	1.3E+08	4.3E+09
60	1.3E+08	5.7E+09
120	1.3E+08	1.1E+10
180	1.3E+08	1.7E+10

19. APPENDIX J

Appendix J contains the results of the dosimetric model for the modelling cases involving Cs-137. They are presented in the figures below.

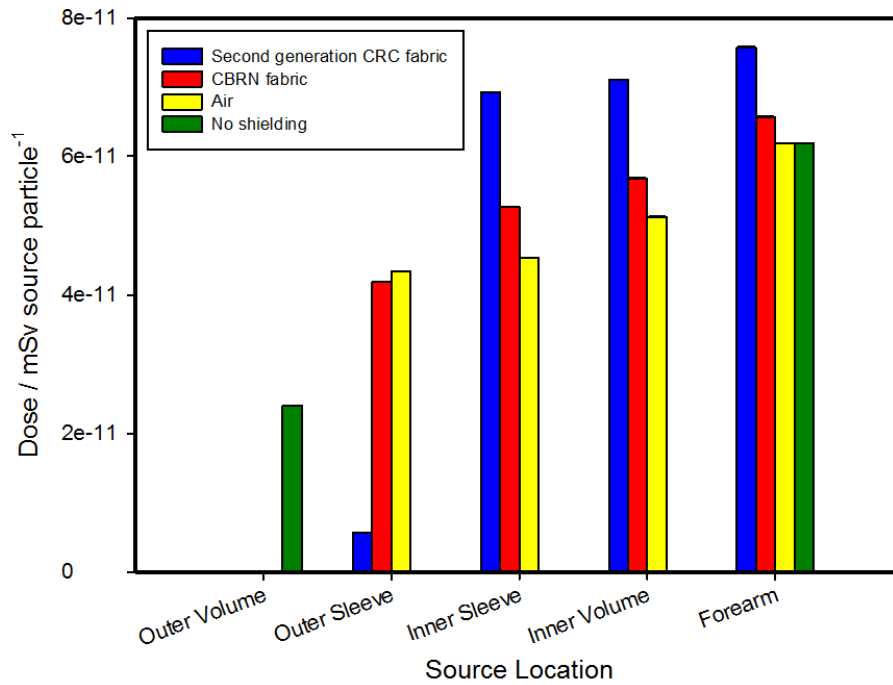


Figure A.14: Overall dose (gamma and beta) imparted to forearm as a function of source location for each of the PPE sleeve compositions when exposed to Cs-137 particulates

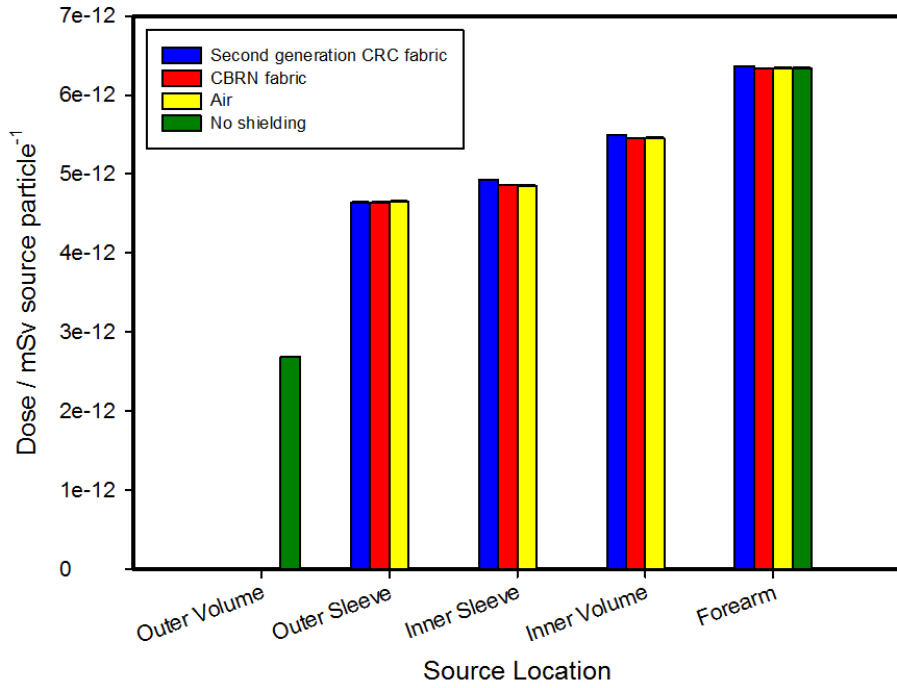


Figure A.15: Gamma-contributed dose imparted to forearm as a function of source location for each of the PPE sleeve compositions when exposed to Cs-137 particulates

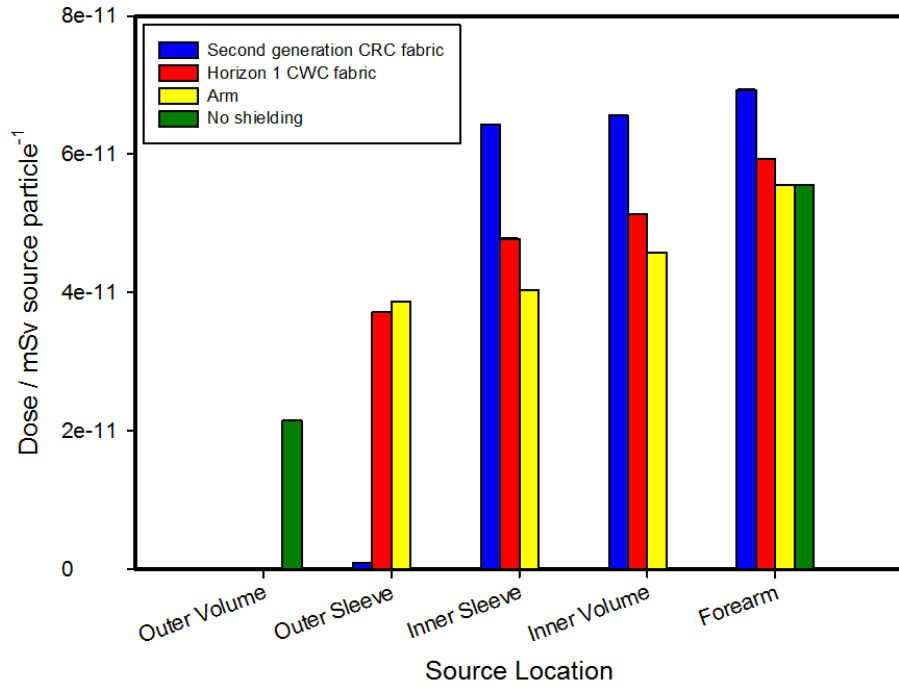


Figure A.16: Beta-contributed dose imparted to forearm as a function of source location for each of the PPE sleeve compositions when exposed to Cs-137 particulates

20. APPENDIX K

Appendix K contains the regional dose rate results obtained by integrating the results of the particulate transport model with those of the dosimetric model for each of the nine modelling cases.

Table A.13: Regional dose rates for the modelling case in which the forearm was surrounded by a PPE sleeve composed of the second generation CRC fabric and exposed to Co-60 particulates

Time / min	Dose Rate / mSv min ⁻¹					
	<i>D_o</i>	<i>D_{outersuit}</i>	<i>D_i</i>	<i>D_{innersuit}</i>	<i>D_{skin}</i>	<i>Total</i>
0	6.9E-05	0.0E+00	0.0E+00	0.0E+00	0.0E+00	6.9E-05
15	6.9E-05	5.5E-04	2.2E-10	1.8E-07	5.0E-07	6.2E-04
30	6.9E-05	1.1E-03	2.2E-10	3.6E-07	1.0E-06	1.2E-03
45	6.9E-05	1.6E-03	2.2E-10	5.5E-07	1.5E-06	1.7E-03
60	6.9E-05	2.2E-03	2.2E-10	7.3E-07	2.0E-06	2.3E-03
120	6.9E-05	4.4E-03	2.2E-10	1.5E-06	4.0E-06	4.4E-03
180	6.9E-05	6.6E-03	2.2E-10	2.2E-06	6.0E-06	6.6E-03

Table A.14: Regional dose rates for the modelling case in which the forearm was surrounded by a PPE sleeve composed of the second generation CRC fabric and exposed to Sr-90 particulates

Time / min	Dose Rate / mSv min ⁻¹					
	<i>D_o</i>	<i>D_{outersuit}</i>	<i>D_i</i>	<i>D_{innersuit}</i>	<i>D_{skin}</i>	<i>Total</i>
0	7.3E-06	0.0E+00	0.0E+00	0.0E+00	0.0E+00	7.3E-06
15	7.3E-06	1.6E-04	2.4E-08	1.8E-05	5.0E-05	2.4E-04
30	7.3E-06	3.3E-04	2.4E-08	3.6E-05	1.0E-04	4.7E-04
45	7.3E-06	4.9E-04	2.4E-08	5.5E-05	1.5E-04	7.0E-04
60	7.3E-06	6.6E-04	2.4E-08	7.3E-05	2.0E-04	9.4E-04
120	7.3E-06	1.3E-03	2.4E-08	1.5E-04	4.0E-04	1.9E-03
180	7.3E-06	2.0E-03	2.4E-08	2.2E-04	6.0E-04	2.8E-03

Table A.15: Regional dose rates for the modelling case in which the forearm was surrounded by a PPE sleeve composed of the second generation CRC fabric and exposed to Cs-137 particulates

Time / min	Dose Rate / mSv min ⁻¹					
	D _o	D _{outersuit}	D _i	D _{innersuit}	D _{skin}	Total
0	1.8E-03	0.0E+00	0.0E+00	0.0E+00	0.0E+00	1.8E-03
15	1.8E-03	1.5E-02	2.3E-08	2.0E-05	5.1E-05	1.7E-02
30	1.8E-03	3.1E-02	2.3E-08	3.9E-05	1.0E-04	3.3E-02
45	1.8E-03	4.6E-02	2.3E-08	5.9E-05	1.5E-04	4.8E-02
60	1.8E-03	6.2E-02	2.3E-08	7.8E-05	2.0E-04	6.4E-02
120	1.8E-03	1.2E-01	2.3E-08	1.6E-04	4.1E-04	1.3E-01
180	1.8E-03	1.9E-01	2.3E-08	2.4E-04	6.1E-04	1.9E-01

Table A.16: Regional dose rates for the modelling case in which the forearm was surrounded by a PPE sleeve composed of the CBRN fabric and exposed to Co-60 particulates

Time / min	Dose Rate / mSv min ⁻¹					
	D _o	D _{outersuit}	D _i	D _{innersuit}	D _{skin}	Total
0	8.2E-05	0.0E+00	0.0E+00	0.0E+00	0.0E+00	8.2E-05
15	8.2E-05	9.2E-04	1.2E-06	9.9E-04	3.0E-03	5.0E-03
30	8.2E-05	1.8E-03	1.2E-06	2.0E-03	5.9E-03	9.8E-03
45	8.2E-05	2.8E-03	1.2E-06	3.0E-03	8.9E-03	1.5E-02
60	8.2E-05	3.7E-03	1.2E-06	4.0E-03	1.2E-02	2.0E-02
120	8.2E-05	7.4E-03	1.2E-06	7.9E-03	2.4E-02	3.9E-02
180	8.2E-05	1.1E-02	1.2E-06	1.2E-02	3.5E-02	5.9E-02

Table A.17: Regional dose rates for the modelling case in which the forearm was surrounded by a PPE sleeve composed of the CBRN fabric and exposed to Sr-90 particulates

Time / min	Dose Rate / mSv min ⁻¹					
	D _o	D _{outersuit}	D _i	D _{innersuit}	D _{skin}	Total
0	5.3E-03	0.0E+00	0.0E+00	0.0E+00	0.0E+00	5.3E-03
15	5.3E-03	8.9E-02	1.1E-04	9.9E-02	3.0E-01	4.9E-01
30	5.3E-03	1.8E-01	1.1E-04	2.0E-01	5.9E-01	9.7E-01
45	5.3E-03	2.7E-01	1.1E-04	3.0E-01	8.9E-01	1.5E+00
60	5.3E-03	3.6E-01	1.1E-04	4.0E-01	1.2E+00	1.9E+00
120	5.3E-03	7.1E-01	1.1E-04	7.9E-01	2.4E+00	3.9E+00
180	5.3E-03	1.1E+00	1.1E-04	1.2E+00	3.5E+00	5.8E+00

Table A.18: Regional dose rates for the modelling case in which the forearm was surrounded by a PPE sleeve composed of the CBRN fabric and exposed to Cs-137 particulates

Time / min	Dose Rate / mSv min ⁻¹					
	D _o	D _{outersuit}	D _i	D _{innersuit}	D _{skin}	Total
0	8.7E-03	0.0E+00	0.0E+00	0.0E+00	0.0E+00	8.7E-03
15	8.7E-03	1.2E-01	1.3E-04	1.1E-01	3.2E-01	5.5E-01
30	8.7E-03	2.3E-01	1.3E-04	2.2E-01	6.4E-01	1.1E+00
45	8.7E-03	3.5E-01	1.3E-04	3.2E-01	9.7E-01	1.6E+00
60	8.7E-03	4.6E-01	1.3E-04	4.3E-01	1.3E+00	2.2E+00
120	8.7E-03	9.2E-01	1.3E-04	8.7E-01	2.6E+00	4.4E+00
180	8.7E-03	1.4E+00	1.3E-04	1.3E+00	3.9E+00	6.6E+00

Table A.19: Regional dose rates for the modelling case in which the forearm was not surrounded by a PPE sleeve and was exposed to Co-60 particulates

Time / min	Dose Rate / mSv min ⁻¹		
	<i>D_o</i>	<i>D_{skin}</i>	<i>Total</i>
0	1.6E-01	0.0E+00	1.6E-01
15	1.6E-01	3.6E-03	1.6E-01
30	1.6E-01	7.3E-03	1.7E-01
45	1.6E-01	1.1E-02	1.7E-01
60	1.6E-01	1.5E-02	1.7E-01
120	1.6E-01	2.9E-02	1.9E-01
180	1.6E-01	4.4E-02	2.0E-01

Table A.20: Regional dose rates for the modelling case in which the forearm was not surrounded by a PPE sleeve and was exposed to Sr-90 particulates

Time / min	Dose Rate / mSv min ⁻¹		
	<i>D_o</i>	<i>D_{skin}</i>	<i>Total</i>
0	1.4E+01	0.0E+00	1.4E+01
15	1.4E+01	3.3E-01	1.4E+01
30	1.4E+01	6.5E-01	1.5E+01
45	1.4E+01	9.8E-01	1.5E+01
60	1.4E+01	1.3E+00	1.5E+01
120	1.4E+01	2.6E+00	1.7E+01
180	1.4E+01	3.9E+00	1.8E+01

Table A.21: Regional dose rates for the modelling case in which the forearm was not surrounded by a PPE sleeve and was exposed to Cs-137 particulates

Time / min	Dose Rate / mSv min ⁻¹		
	<i>D_o</i>	<i>D_{skin}</i>	<i>Total</i>
0	1.7E+01	0.0E+00	1.7E+01
15	1.7E+01	4.0E-01	1.8E+01
30	1.7E+01	8.0E-01	1.8E+01
45	1.7E+01	1.2E+00	1.8E+01
60	1.7E+01	1.6E+00	1.9E+01
120	1.7E+01	3.2E+00	2.0E+01
180	1.7E+01	4.8E+00	2.2E+01

21. APPENDIX L

Appendix L presents the total dose rate regression equations as a function of time for each of the nine modelling cases. These equations were subsequently integrated to determine the total dose imparted to the forearm tissue as a function of time for each set of exposure conditions. A residual analysis was performed on each regression equation in order to determine the error associated with the slope and y-intercept values; however, as the results ranged in magnitude from 10^{-7} - 10^{-18} , they have not been included in Table A.22.

Table A.22: Total dose rate regression equations for the nine modelling cases

Case	PPE fabric	Radionuclide	Regression Equation	R ²
1	Second generation CRC	Co-60	$y = 3.6E-05 t + 6.9E-05$	1.0
2		Sr-90	$y = 1.6E-05 t + 7.3E-06$	1.0
3		Cs-137	$y = 0.0010 t + 0.0018$	1.0
4	CBRN	Co-60	$y = 0.0003 t + 8.3E-05$	1.0
5		Sr-90	$y = 0.032 t + 0.0054$	1.0
6		Cs-137	$y = 0.036 t + 0.0088$	1.0
7	No shielding	Co-60	$y = 0.0002 t + 0.16$	1.0
8		Sr-90	$y = 0.022 t + 14$	1.0
9		Cs-137	$y = 0.027 t + 17$	1.0